**Article:**
Wheeler, J., Piazolo, S., Prior, D.J. et al. (2 more authors) (2023) Using crystal-lattice distortion data for geological investigations: the weighted Burgers vector method. Journal of Structural Geology, 179. 105040. ISSN 0191-8141

https://doi.org/10.1016/j.jsg.2023.105040

Journal of Structural Geology

# Using crystal-lattice distortion data for geological investigations: the weighted Burgers vector method

--Manuscript Draft--

| | |
|---|---|
| **Manuscript Number:** | SG-D-22-00329R2 |
| **Article Type:** | Original article |
| **Keywords:** | Electron backscatter diffraction; Geometrically Necessary Dislocations; slip systems; Intracrystalline Distortion; Weighted Burgers Vector |
| **Corresponding Author:** | John Wheeler, PhD<br>University of Liverpool<br>UNITED KINGDOM |
| **First Author:** | John Wheeler, PhD |
| **Order of Authors:** | John Wheeler, PhD |
| | Sandra Piazolo, PhD |
| | David J Prior, PhD |
| | Patrick W Trimby, PhD |
| | Jacob A Tielke |
| **Abstract:** | Distorted crystals carry useful information on processes involved in their formation, deformation and growth. The distortions are accommodated by geometrically necessary dislocations, and therefore characterising those dislocations is an informative task, to assist in, for example, deducing the slip systems that produced the dislocations. Electron backscatter diffraction (EBSD) allows detailed quantification of distorted crystals and we summarise here a method for extracting information on dislocations from such data. The weighted Burgers vector (WBV) method calculates a vector at each point on an EBSD map, or an average over a region. The vector is a weighted average of the Burgers vectors of dislocation lines intersecting the map surface. It is weighted towards dislocation lines at a high angle to the map but that can be accounted for in interpretation. The method is fast and does not involve specific assumptions about dislocation types; it assumes only that elastic strains have little effect on the calculation. It can be used, with care, to analyse subgrain walls (sharp orientation changes) as well as gradational orientation changes within individual grains. There are four linked parts to this contribution.<br><br>We describe the mathematical background to the WBV and then how it is modified to deal with spaced, discrete orientation measurements.<br><br>EBSD orientation data have angular errors, and so does the WBV. We present a new analysis of these angular errors, showing there is a trade-off between directional accuracy and area sampled. Angular errors can now be accounted for during testing of hypotheses about dislocation types.<br><br>We present new studies on olivine and plagioclase to illustrate how to use the method.<br><br>We discuss published studies on ice and titanite to further illustrate the method.<br><br>We note that the methods discussed here are applicable to any crystalline material |

| | |
|---|---|
| | encompassing minerals (including ice), metals and ceramics. |
| **Suggested Reviewers:** | Manish A Mamtani<br>Professor, Indian Institute of Technology Kharagpur<br>mamtani@gg.iitkgp.ac.in<br>Reviewed previous version. EBSD + TEM expert |
| | Elena A Miranda<br>Professor, California State University Northridge<br>elena.miranda@csun.edu<br>EBSD expert |
| | Virginia Gail Toy<br>Professor, Johannes Gutenberg University Mainz<br>virginia.toy@uni-mainz.de<br>EBSD expert |
| | Andrew Cross<br>Assistant Scientist, Woods Hole Oceanographic Institution<br>across@whoi.edu<br>EBSD expert |
| | Luca Menegon<br>Professor, University of Oslo<br>luca.menegon@geo.uio.no<br>EBSD expert |
| **Response to Reviewers:** | |

Highlights

- The Weighted Burgers Vector method gives constraints on dislocations in minerals
- It uses EBSD data and makes no prior assumptions about dislocation types
- Angular errors are reduced by analysing larger regions of maps
- Applications to olivine and plagioclase are discussed

No Conflict of Interest

**Declaration of interests**

☐The authors declare that they have no known competing financial interests or personal relationships that could have appeared to influence the work reported in this paper.

☒The authors declare the following financial interests/personal relationships which may be considered as potential competing interests:

John Wheeler reports a relationship with Oxford Instruments Nanoanalysis that includes: consulting or advisory. The lead author assisted Oxford Instruments Nanoanalysis with development of a commercial version of the WBV algorithm. This was commercialisation of Intellectual Property developed at University of Liverpool, so OINA paid a sum to UoL. Co-author Trimby facilitated developing the relationship between OINA and UoL. The manuscript comprises ideas developed in collaboration prior to this commercialisation.

**Credit author statement**

**John Wheeler:** Conceptualization, Software, Writing - Original Draft, Visualization; **Sandra Piazolo:** Conceptualization, Writing – Review and Editing; **David Prior:** Conceptualization, Writing – Review and Editing; **Patrick Trimby:** Conceptualization, Resources, Writing – Review and Editing; **Jake Tielke:** Resources, Writing – Review and Editing.

Hi Virginia
Many thanks for taking charge of the final stage of review. Our replies bulleted.

I did try to ask the previous reviewers to check what you've done, but they didn't have time, so I did it. I am satisfied that you've addressed most of their recommendations in the revision aside from a few nagging things - which is why I'm requesting minor revisions. I invite you to resubmit your manuscript after addressing my final comments below. Please resubmit your revised manuscript by Feb 03, 2024. And this time please use track changes?

- Thanks for your help, and once again apologies for not tracking changes previously. As well as Editor's suggested edits we made 3 other changes.

1. A paper just out confirms and goes beyond our prediction that high angular resolution EBSD data lead to WBV calculations with lower errors, so we cited this on li 789-793.
2. We don't include that paper in Table 1 because it opens up a whole new discussion, but we added to the caption to make clear the assumption behind our $\alpha_{95}$ estimates.
3. Acknowledged you, including doing more than just the usual editorial role.

Here are your specific suggestions and our responses.

L98. Jiang lacks a year.

- Done

L102-118. Is it possible to more explicitly state that basically you are reconsidering the original WBV idea in context of the ways it has been used, and abused, in the 14 years since your original publication (2009), with the ultimate goal of ensuring that it, and other methods of measuring distortion, are more realistically employed in future studies?

- Rephrased and done. We still need the four subdivisions since reviewers were confused as the aims appeared mixed up.

L124. remove one extra right parenthese

- Done

L210. one reason(s) - delete s.

- Done

L211 'it is convenient to use units of (μm)-1). Could you say 'we recommend using the convenient units of "per-micron"

- Now 214. Done

Q: Lines 179**: i.e..** "there should be no large orientation variations around the loop" – what would this look like? What is "large"? How would a reader know if they had this problem? A: We cannot provide comprehensive information on misorientations above which boundaries are disorganised; the user must decide.
VT: Yes, but at this stage in the text you say that you will explain later how to recognise or deal with the effect of a large orientation gradient, but I can't really work out where you mean. Why not state here "as explained in Section XXX"?

- new li 232. 228-238 rewritten, hopefully clearer

L275. Half sentence 'In a later section…". Did you miss something else here or should you just delete these words?

- new 280. Deleted

Q: Line 226: The angle theta should be labeled within Figure 2a—if the sentence calling out 2a mentions theta, this would help integrate the figure with the text. It would be helpful to also label x and y direction in the yellow map surfaces in Figure 2. A: Figure 2 end,
VT: Did you do anything in response to this comment? I can't see changes of this nature to the figure.

- The referee was referring to OLD Fig. 2 now Fig. 3. It wasn't done but is fixed now. Caption modified.

L312-313. You could also say that a disorientation angle "has no absolute sign"?

- Done

Q: L295: "So, although eqn. (4) still applies, it is not particularly helpful": Equation 4 would have to be evaluated between two points with a finite separation, in which case it's just as helpful as evaluating it around a loop enclosing a finite area (notwithstanding nuances of noise levels), so I'm not sure this sentence is quite right; does it need rephrasing? A: The sentence is correct because in this section it is based on the orientation being a mathematical function of position, and gradients are defined using partial differentiation. We make discussion of spaced measurement points a separate and later section, and such issues are discussed around new Fig. 6.
VT: I think it's useful if you explicitly state which later section this topic is further discussed in.

- New line 365-373 etc. This triggered a rewrite as well as referring forwards to section 2.3.2, and there (li 463) referring back.

L834. 'Do you mean 'Crystalscape is for academic use only.'

- We weren't sure if you were suggesting removal of mentioning Aztec Crystal. But we think this should be in there so the reader understands the choices available. Slightly rephrased.

John Wheeler
13 Dec 2023

# For submission to Journal of Structural Geology

## Using crystal-lattice distortion data for geological investigations: the weighted Burgers vector method

J. Wheeler[1], S. Piazolo[2], D. J. Prior[3], P. W. Trimby[4] and J. A. Tielke[5]

[1]Department of Earth, Ocean, and Ecological Sciences, University of Liverpool, 4 Brownlow Street, Liverpool, L69 3GP, UK

[2] University of Leeds, School of Earth & Environment, Leeds LS2 9JT, UK

[3]Department of Geology, University of Otago, Dunedin, New Zealand

[4]Oxford Instruments Nanoanalysis, High Wycombe, Bucks, England

[5]Lamont-Doherty Earth Observatory of Columbia University, Palisades, NY, USA

**Abstract**

Distorted crystals carry useful information on processes involved in their formation, deformation and growth. The distortions are accommodated by geometrically necessary dislocations, and therefore characterising those dislocations is an informative task, to assist in, for example, deducing the slip systems that produced the dislocations. Electron backscatter diffraction (EBSD) allows detailed quantification of distorted crystals and we summarise here a method for extracting information on dislocations from such data. The weighted Burgers vector (WBV) method calculates a vector at each point on an EBSD map, or an average over a region. The vector is a weighted average of the Burgers vectors of dislocation lines intersecting the map surface. It is weighted towards dislocation lines at a high angle to the map but that can be accounted for in interpretation. The method is fast and does not involve specific assumptions about dislocation types; it assumes only that elastic strains have little effect on the calculation. It can be used, with care, to analyse subgrain walls (sharp orientation changes) as well as gradational orientation changes within individual grains. There are four linked parts to this contribution.

1. We describe the mathematical background to the WBV and then how it is modified to deal with spaced, discrete orientation measurements.
2. EBSD orientation data have angular errors, and so does the WBV. We present a new analysis of these angular errors, showing there is a trade-off between directional accuracy and area sampled. Angular errors can now be accounted for during testing of hypotheses about dislocation types.
3. We present new studies on olivine and plagioclase to illustrate how to use the method.
4. We discuss published studies on ice and titanite to further illustrate the method.

We note that the methods discussed here are applicable to any crystalline material encompassing minerals (including ice), metals and ceramics.

**Keywords**

Electron Backscatter Diffraction; Geometrically Necessary Dislocations; Slip Systems; Intracrystalline Distortion; weighted Burgers vector; Olivine; Plagioclase; Ice; Titanite

## 1. Introduction

Microstructures are crucial indicators of processes that have affected rocks. Dislocations provide evidence for how and under what conditions individual grains have deformed or they may be growth defects indicating growth conditions. Regardless of their origin dislocations give rise to *distortion* in a crystal lattice on some scale, and we advocate use of this word as a non-genetic description of their geometric effects. If dislocations are due to deformation their Burgers vectors may help constrain the style or conditions of deformation. Individual dislocations give a lattice extra energy, so the density of dislocations is needed to estimate this on a volumetric basis. This plastic strain energy provides a driving force for recrystallization in deformed rocks (Drury & Urai 1990). TEM is the standard method to image individual dislocations, a procedure that can be laborious and will characterise just a tiny fraction of the microstructure, leaving doubts as to how representative it is. In contrast intracrystalline distortions may be optically visible and can be quickly characterised by EBSD mapping over large regions. Such distortions, regardless of cause, must be accommodated by geometrically necessary dislocations (GNDs) (Ashby 1970) and hence give indirect information on dislocation content.

The GND concept complements the statistically stored dislocation (SSD) concept. The dislocations involved are not fundamentally different types; instead, these are scale dependent ideas. Lattice curvature over a particular length scale is by definition accommodated by GNDs *at that scale.* Over that length scale there may be other dislocations for example of opposite signs, that cancel out each other's local curvature effects (though still contribute to plastic strain energy and other relevant properties): these are SSDs. Zooming in to a smaller length scale may reveal local lattice curvatures related to what were classified as SSDs. At this smaller length scale some SSDs are now GNDs. If one examines lattice curvature on the atomic scale, all dislocations would be classified as GNDs. In relation to EBSD, the relevant length scale is the step size. So lattice curvature shown on EBSD maps relates to GNDs on the scale of the step size. SSDs will, by definition, not leave a fingerprint on the curvature. A smaller step size will reveal more GNDs. Very small step sizes can reveal individual dislocations (https://www.ebsd.com/ois-ebsd-system/dislocation-density-analysis).

It would be useful to constrain *directional* (lines, Burgers vectors) and *magnitude* (dislocation density) GND information from EBSD data: examples of approaches follow. If distortion is due to deformation by dislocation motion it can in principle be used to constrain active slip systems (hence deformation conditions) using directional information. Based on geometric assumptions alone, such studies have often focussed on subgrain walls (in essence, localised sharp distortions). For example Lloyd (2002) argues that subgrain walls traces and misorientation axes in quartz can be used to deduce slip systems, though assumptions about "pure" tilt or twist nature of boundaries are needed. Wieser et al. (2020) applied a modified approach to olivine, incorporating subgrain wall traces with information from the method of Wheeler et al. (2009). The latter, the weighted Burgers vector (WBV) method, is what we discuss in this contribution. In minerals with multiple slip systems, distortion cannot be uniquely linked to slip systems using geometry alone. Calculations can then be made assuming that the net dislocation energy is minimised with respect to all possible combinations of dislocation lines and Burgers vectors for example in quartz (Wallis et al. 2019b). Distortion magnitudes can be quantified using for example "local misorientation" though the link to actual dislocation densities is not straightforward to make. For example

Timms et al. (2012) use local misorientation maps to give an overview of the heterogeneous distortion in shocked zircon crystals.

If distortion is due to growth, or is postulated to be, then purely geometric analyses can be applied as they would be to deformed crystals but any extra assumptions must be evaluated with care. Spruzeniece et al. (2017) quantified crystal distortions in KBr-KCl solid solution grown in a stress-free environment: these are due to growth not deformation. Gardner et al. (2021) examined natural distorted albite and showed that some subgrain walls contain dislocations with Burgers vectors with <010> components. There are no known slip systems with such Burgers vectors, so the subgrain walls were diagnosed as growth defects.

The methods in these and many other papers using EBSD to analyse distortions include various assumptions, both in manual processes (e.g. selecting straight segments of boundary traces) and in automatic calculations (e.g. assumptions about allowed slip systems and dislocation energy minimisation). It is generally not clear how errors in EBSD orientation measurements affect deductions: specifically, here we address *angular* errors although *magnitude* errors are relevant (e.g. Jiang et al. (2013)). Some methods are slow if they are manual or compute intensive, a relevant consideration in terms of time versus benefit. Methods using boundary trace analysis cannot be applied to smooth, distributed distortions because there are no discrete boundaries. Overall, the methods to date have diverse strengths and weaknesses.

Our overall aim here is to review and extend the WBV method for extracting information on GNDs from EBSD data, based on our experience of how it has been used since first publication in 2009. By clarifying and enhancing the insights it can give we hope to encourage its use in future studies. There are four linked aims.

1. A description of the theoretical basis based on existing understanding (sections 2.1-2.3) but using new illustrative models. We explain the method using model distorted crystals, with mathematical details in Supplementary Information. We discuss how the method applies to smoothly curved lattices and to subgrain walls (where GNDs are collected into surfaces of negligible width). The aim here is to ensure users of the method understand its advantages and limitations.
2. New analysis of the errors (specifically angular errors) inherent in the calculation, so that hypotheses about microstructural evolution can be tested robustly (section 2.4).
3. New examples of application of the method (sections 3.1 olivine and 3.2 plagioclase) to assist in understanding how it works in practice.
4. Review of implications for previous studies in section 3.5 (Table 1), with some detail in 3.3 ice and 3.4 titanite.

Finally, we discuss this method in relation to others used to analyse intracrystalline distortion and suggest future developments. We note that the methods discussed here are applicable to any crystalline material encompassing minerals (including ice), metals and ceramics.

## 2. The WBV method: background and error analysis

The method gives information on combinations of GND Burgers vectors and GND densities, so we now discuss these two concepts. Imagine a closed loop joining atoms (or unit cells) around a dislocation in “sample coordinates” (Fig. 1a, c). Now move the atoms to the positions they would have in an undistorted crystal: the Burgers vector is the gap opened up

in the previously closed loop (red arrows in Fig. 1b, d) in "crystal coordinates"). It can be described in crystal coordinates (hence dimensionless, for example [100] for the edge and [001] for the screw) or in sample coordinates (dimensions of length; direction depends on sample orientation). Dislocation density is a phrase that is used in different ways. It may refer to the total line length of SSDs in a unit volume. Not all of these give rise to lattice curvature so here we consider only the total line length of GNDs per unit volume. We illustrate the basic ideas using a 2D model first.

Fig. 1. a) A closed loop around an edge dislocation in sample space, view down along the dislocation line. b) The same path traced out in crystal coordinates, showing a gap that is the definition of the Burgers vector (red) of the dislocation within the loop. c), d) The same for a screw dislocation; the dislocation line is parallel to the Burgers vector.

*2.1. Concepts in 2D*

GND density relates to lattice curvature and a 2D description illustrates this most simply, where there is no distortion in the z or [001] direction. We show here how curvature relates to single then multiple dislocation populations. Figure 2 shows lattice orientations in a 2D model which can, at each point, be described by a single number (angle θ of a particular lattice direction anticlockwise from a reference direction). In 2D all dislocations have edge character and in the Figure the Burgers vectors are defined as one atomic spacing so **b** = [100]. The four frames show increasing dislocation density ρ, defined in 2D as the number of dislocations per unit area, and the corresponding increase in lattice curvature. The irregular spacing of dislocations means this model is an approximate illustration but provides a basis for understanding.

Figure **2.** Visualization of the link between GND density (chosen here as edge dislocations all the same sign) and lattice curvature. The crystallographic "z" direction [001] is chosen as out of the page so the dislocations illustrated have line vector [001] and Burgers vector [100]. Angle θ, dependent on position, shows orientation of a lattice direction relative to a reference direction (thick line).

EBSD measurements do not pick out individual atoms but provide orientation θ as a defined function of position (in 2D, θ(x, y)); that is what we must work with. Lattice curvature is defined by variations in θ in the x and/or y directions. The lattice curvature is then a vector

$$\boldsymbol{\kappa} = -\left(\frac{\partial\theta}{\partial x}, \frac{\partial\theta}{\partial y}\right) \quad (1)$$

(see Appendix 2.1 for details). There is one key assumption made when using the WBV method: that elastic strains have a relatively small effect. If EBSD records lattice curvature, then that could in principle be caused by elastic strain. As EBSD cannot generally image individual dislocations, an EBSD map of (for example) Fig. 2 could look identical to a map of a perfect lattice with no GNDs, elastically bent. However, as was argued in Wheeler et al. (2009), in the microstructures we have studied, curvature is often localized along sub-grain

walls and we cannot conceive of elastic strain being localized in this way. Secondly, we would expect elastic bending in a wide variety of orientations in a polycrystal, giving rise to a wide variety of (illusory) WBVs. Instead, we see systematic patterns as exhibited in the case studies we present here, and in most of the published studies (Table 1). Wallis et al. (2019a) find that "often the rotation gradients are larger than the elastic strain gradients … in which case, the elastic strain gradients can be neglected".

From now on we will assume no elastic strains and, in that case, $\boldsymbol{\kappa}$ relates to a single population of GNDs by

$$\boldsymbol{\kappa} = \rho \boldsymbol{b}$$

that incorporates the fact that in sample coordinates, **b** may vary even if it is a single crystallographic direction. Considering just the magnitudes, we can write this as

(curvature) = (dislocation density) × (Burgers vector length)

which is a starting point for understanding the link between curvature and dislocation density. If there is more than one type of dislocation (each with different Burgers vectors and densities)

$$\boldsymbol{\kappa} = \sum_N \rho^{(N)} \boldsymbol{b}^{(N)} \qquad (2)$$

where ρ and **b** are the density and Burgers vectors *for each type* (superscript N) of dislocation. If there were just 2 types of dislocation, this equation would yield their densities uniquely. If more than 2 types are present then the densities are non-unique, but the equation still provides constraints. Such issues are relevant for 3D which we now discuss.

### *2.2. Concepts in 3D*

In 3D we require three numbers to define a lattice orientation (e.g. conventionally three Euler angles, although other representations are available), and we have three directions in which to evaluate gradients, there are 9 gradients to consider. Nye (1953) showed how curvature is then a second rank tensor, but a more direct link to dislocation density (line length per unit volume in 3D) is established via a tensor $\boldsymbol{\alpha}$ (which now carries his name), also a function of orientation gradients. This links to dislocation density as follows.

$$\alpha_{i\gamma} = \sum_N \rho^{(N)} b_i^{(N)} l_\gamma^{(N)} \qquad (3)$$

where ρ, **b** and **l** are the density, Burgers vector and unit line vector for each type (labelled N) of dislocation. Note the close resemblance to eqn 2, but with the extension to include dislocation line vectors. When there are many types of dislocation, there may be multiple combinations giving a particular Nye tensor. Note the following.

- This has to be written in terms of vectors and tensors, since the situation is 3D.
- Such equations are best written using index notation which makes explicit whether vectors are expressed in crystal coordinates (Latin subscript for $b_i$) or sample coordinates (Greek subscript for $l_\gamma$), for reasons explained in Wheeler et al. (2009) and Das et al. (2018).
- $\boldsymbol{\alpha}$ is sometimes called "dislocation density" but must be distinguished from other uses of the same phrase.

Determining the full Nye tensor requires orientation gradients in all three directions. Although there are GND studies using 3D EBSD from serial focussed ion beam milling e.g. (Kalácska et al. 2020, Konijnenberg et al. 2015) these are challenging and generally EBSD is conducted on 2D sections. Wheeler et al. (2009) showed that relevant (though incomplete) information could still be extracted from a 2D map. Specifically, of the 9 components of the Nye tensor, a 3-component vector can be calculated. The vector is a sum of Burgers vectors of GNDs, *weighted* by the actual dislocation density of each type of GND and by the angle between the dislocation lines and the map. Lines at a high angle to the map are favoured because the mathematics involves multiplying the true density by sin(angle between dislocation line and map). The phrase "weighted Burgers vector" (WBV) was used, to make clear that this vector is a weighted "sample" of the Nye tensor.

$$W_i = \alpha_{i3} = \sum_N \rho^{(N)} b_i^{(N)} l_3^{(N)} = \sum_N \left[\rho^{(N)} l_3^{(N)}\right] b_i^{(N)} \quad (4)$$

where W is the WBV, and the subscript "3" refers to the z direction, perpendicular to the map, so $l_3$ is the component of a dislocation line vector perpendicular to the map: it varies from 0 (lines parallel to map) to 1 (lines perpendicular to map). The terms in square brackets are scalars, so note that the WBV is a linear combination of Burgers vectors – this is one reason why it is a useful quantity. The WBV has units of $(\text{length})^{-1}$ and we recommend using the convenient unit of $(\mu\text{m})^{-1}$. We denote its magnitude as W. It can be expressed in crystal coordinates as in eqn (4), or in sample coordinates by calculating **hW** where **h** is the orientation tensor (a function of Euler angles). It might appear that this will give a non-unique answer for the vector in sample coordinates, since **W** has symmetric variants in crystal coordinates, but Appendix 1 shows this is not the case – there is a unique WBV in sample coordinates.

There are two approaches to calculating **W**, differential and integral. The differential method involves evaluating local gradients in **h** around the point at which **W** is required. Since that point has a specific orientation, **W** can be expressed in crystal or sample coordinates. The integral method involves integrating round a closed loop on the map to obtain the *net* or *average* Burgers vector content of the GND lines intersecting the map inside the loop, expressed in crystal coordinates. The mathematics in essence defines the loop in sample coordinates (c.f. Fig. 1a) black arrows), transforms each loop segment (black arrow) into crystal coordinates (c.f. Fig. 1b) black arrows), and sums up the segments in crystal coordinates to give the net Burgers vector (red arrow). For the calculation to be meaningful there should be no "high angle" grain boundaries (HAGBs) (which do not usually have organised dislocation substructures) intersected by the loop. If the loop crosses HAGBs then the calculation will still return a vector, but that will not give clear information on dislocations. There is no systematic knowledge of or agreement on what constitutes an HAGB and we usually pick 5 degrees as a maximum angle, discussed further in section 2.2.5. Unlike the differential method, there is no strict way to express the vector in sample coordinates because orientation varies around and within the loop and the result of the integral method is not linked to any specific point within the loop. However, if the loop does not include HAGBs then orientation variations in the loop are small and the orientation at, for example, the loop centroid could be used to convert from crystal to sample coordinates.

If the orientation **h** is a defined mathematical function of position, then the methods are identical (they are related by Stokes' theorem). In practice **h** is defined at discrete measurement points, e.g. on a square grid. The differential method then involves numerical estimation of orientation gradients, with some flexibility in terms of the number of points used. The integral method involves numerical integration around the closed loop. As we will show later (section 2.3), the methods have different advantages in practice.

*2.2.1. WBV, lattice vectors and Burgers vectors*

In this section we discuss the links between WBV and Burgers vectors and show how there may be unique or non-unique relationships. In the approach we describe here, the "differential" values of WBV are usually expressed in units of $(\mu m)^{-1}$. In crystal coordinates **W** can be decomposed into lattice basis vectors **L** if needed

$$\boldsymbol{W} = K_1\boldsymbol{L}_1 + K_2\boldsymbol{L}_2 + K_3\boldsymbol{L}_3 \quad (5)$$

where the coefficients K are in units of $(\text{length})^{-2}$. These coefficients *resemble* dislocation densities but are in general different. This decomposition relates to the GND types and densities and is unique but further assumptions are needed to express it in terms of the Burgers vectors of actual slip systems. For example, in olivine, slips systems have Burgers vectors that are either [100] or [001]. If we find that **W** is parallel to [203] and we know the distortion is due to crystal plasticity then we can deduce that it shows a combination of slip systems with [100] and [001] Burgers vectors. The magnitude of **W** parallel to [100] would then, in accord with eqn. (4), be a weighted sum of the dislocation densities of all types of dislocation with [100] Burgers vectors. In anhydrite, also orthorhombic, slip systems can involve [001], [1-1-2] and [11-2] Burgers vectors (Hildyard et al. 2009). There is a unique way to express the three components of **W** in terms of those three vectors, if those vectors are linearly independent: in this example [203] = 7[001] + [1-1-2] + [11-2]. However, many crystals have more than three Burgers vectors for possible slip systems, especially in more symmetric crystals counting all symmetric variants. For example, in a trigonal phase such as calcite, there will be at least 3 Burgers vectors in the basal plane. Any two of these can be combined to give the basal plane component of **W**, so the decomposition is non-unique. **W** still carries valuable information on the relative contributions of dislocations with basal and non-basal Burgers vectors (Chauve et al. 2017). Our philosophy here is that the methods give the value of **W**, and if further assumptions are required (in terms of expected slip systems, relative energies etc.) these should be made on a case-by-case basis. The K coefficients can be related to GND densities using further information such as the specific Burgers vectors of GNDs.

Except for angular errors which are discussed later, it is crucial to note that the WBV cannot generate "phantom" directions: it must be the weighted average of Burgers vectors that are actually present in the microstructure. For example, regardless of mineral symmetry, if **W** is [203] then *at least one* of the GND types involved *must* have Burgers vector with an [001] component, though not necessarily parallel to [001]. Similarly, *at least one* of the GND types involved *must* have Burgers vector with an [100] component. **W** could be decomposed as 2[100] + 3[001], or 2[101] + 1[001], or 3[101] – 1[001] or even simply 1[203] if [203] is a known Burgers vector.

We next illustrate how to visualise and interpret the WBV, using models for a smoothly tilted lattice and a smoothly twisted lattice (for illustration, distortions are much larger than those found in real crystals). We then address a tilt subgrain wall, describing some issues that are specific to sharp changes in orientation. The models have no variation of orientation in the z direction and the Nye tensors can be calculated fully (Appendix 2).

Figure **3.** Basic WBV concepts illustrated with model tilted and twisted crystals. a), b) 3D views of model tilted and twisted crystals, planes are colour coded in accord with IPF key (inset) for plane normal. Pale yellow of semi-transparent rectangles indicates the map plane though not the shape, with x and y marked for subsequent maps. c), d) Misorientation relative to top-left corner for tilt and twist models. In c) misorientation is around the [001] axis that points out of the page. In d) misorientation is around the [010] axis, running left-right, with linearly increasing gradient of twist angle to right. e), f) WBV magnitude (in $\mu m^{-1}$) colour coded for each model. In e) actual vector directions shown as white arrows; in f) WBV directions point directly into page so are not shown. The boxes are example integration loops with the net WBV indicated as K coefficients in $(\mu m)^{-2}$. g), h) WBV direction colour coded for each model. i) 3D view of semi-transparent WBV magnitude map for tilt model (as in (e)), with edge dislocations lines shown schematically: parallel to [010] and colour coded in accord with their [100] Burgers vectors. j) 3D view of semi-transparent WBV direction map for twist model (as in (h)), with two sets of screw dislocations lines shown schematically: blue parallel to [100], red parallel to [001]. For visual clarity the dislocations are shown as if in walls, but the distortion gradient is smooth. Note how the "weighting" towards dislocation lines perpendicular to the map causes variation in WBV direction (as in f) although the relative density of the two types of dislocation is uniform in 3D.

*2.2.2. Smoothly tilted crystal*

This model is similar to Fig 2, with a 3D view shown in Fig. 3a). The lattice is misoriented relative to the y-axis by an angle θ (zero along the y-axis and < 0 to the right), Fig. 3c). The misorientation axis is [001] that points out of the page. The centre of curvature is beyond the bottom left of the map (Fig. 3c)). If r is the distance to this centre, it is the radius of curvature of the lattice and in sample coordinates

$$\boldsymbol{W} = \frac{1}{r}(\cos\theta\,, \sin\theta\,, 0)$$

and in crystal coordinates,

$$\boldsymbol{W} = \frac{1}{r}(1, 0, 0) \qquad (6)$$

The magnitude of W is shown in Fig. 3e), increasing towards the centre of curvature in accord with eqn. (6). The WBV is a vector that can be represented in sample or crystal space: these require different methods for visualising direction. In sample space WBVs can be displayed as arrows on a map as in Fig. 3e). The direction in crystal coordinates is colour coded (as in any other sort of IPF map) in Fig. 3g), with the IPF colour scheme inset. Since **W** is everywhere parallel to [100] we see a single colour. The rectangle is an integral loop

labelled with its net Burgers vector content in units of $(\mu m)^{-2}$; note only the first [100] component is non-zero.

Multiple decompositions of **W** are possible, but the simplest is a single population of edge dislocations with lines parallel to [001], Burgers vectors parallel to [100] and density

$$\frac{1}{ar}$$

where a is the length of [100]. Fig. 3i) shows a 3D view of that model. If this were not a model, all the map and WBV data could be in accord with other interpretations, for example dislocation lines not parallel to z. However, *any* interpretation must involve dislocations with Burgers vectors with a [100] component: the WBV calculation cannot generate "phantom" components (see above).

*2.2.3. Smoothly twisted crystal*

This model illustrates the importance of understanding the "weighting" or stereological bias in the WBV calculation. In Fig. 3b) the twist is defined by misorientation by angle θ around the [010] axis, with $\frac{d\theta}{dx}$ increasing to the right. Fig. 3d) shows the misorientation, defined as the *minimum* angle (with no absolute sign) required to rotate a lattice back to a reference orientation, relative to the top-left corner. Because this is olivine, symmetry dictates that the misorientation reaches a maximum at 90 degrees then decreases rightwards even though the lattice is more twisted to the right and the angle θ used for calculations increases monotonically. In sample coordinates (appendix 2.2) we have

$$\boldsymbol{W} = \frac{d\theta}{dx}(0, 0, -1)$$

In crystal coordinates

$$\boldsymbol{W} = \frac{d\theta}{dx}(\sin\theta\,, 0, -\cos\theta)\,. \qquad (7)$$

The magnitude of W is simply $\frac{d\theta}{dx}$ and increases linearly to the right because θ is quadratic in x (Fig. 3f)). WBV arrows in sample coordinates are not shown for the twist example because they all point vertically out of the map. Despite the fact that individual dislocation lines and Burgers vectors are clearly not vertical, the WBV components parallel to the map cancel out because we are adding weighted contributions. In crystal coordinates the direction of **W** varies sinusoidally with θ (Fig. 3h)). The rectangle is an integral loop labelled with its net Burgers vector content in units of $(\mu m)^{-2}$; note both [100] and [001] components are non-zero, in agreement with the presence of blues and purples within the loop. The variation in WBV direction across the map could be interpreted to mean that different types of dislocation predominate in different parts of the model. This is not the case: it is a stereological effect and needs careful explanation now because such effects must be borne in mind in any study.

Multiple decompositions of **W** are possible, but the simplest is as a sum of contributions from screw dislocations parallel to [100] with a density of

$$\frac{1}{a}\frac{d\theta}{dx}$$

and screw dislocations parallel to [001] with a density of $\frac{1}{c}\frac{d\theta}{dx}$.

This decomposition is show in Fig. 3j). The screw dislocation lines are coloured using the IPF colour scheme for screw dislocation *line direction* (as in Fig. 3g)) but since these are screw dislocations the colours also indicate Burgers vector directions. Consider the model near the left hand end where θ is small. Blue dislocations, with [100] line vectors, are almost parallel to the map. This means the WBV calculation does not "sample" them and the IPF colour (Fig. 3h)) is dominated by red [001]. As the lattice is more twisted passing to the right, [100] lines are at higher and higher angles to the map. Hence the WBV IPF map is more dominated by blue. At a position near the right-hand side of the map, [001] lines are parallel to the maps so are not sampled at all; the IPF map is blue. As θ increases beyond 90 degrees we see an influence of [001] reappear. This is an example of the "weighting" towards dislocation lines at a high angle to the map.

The twist structure illuminates some fundamental aspects of WBV. The displays are entirely in accord with eqn. (7) and the WBV provides a weighted "subset" of the full dislocation population. If we were to examine another map at right angles to the one considered (but still containing the twist rotation axis) this second map would show a preponderance of [100] vectors at the left end, with more [001] passing to the right – it would look quite different.

*2.2.4. Model of subgrain tilt wall*

Many microstructures contain subgrain walls that, although populated by GNDs, have in essence zero width and hence zero volume. This means that dislocation density, defined as line length per unit volume, is infinite. Similarly, a sharp change in orientation means the lattice curvature is infinite. So, although eqn. (4) still applies, it is not particularly helpful. In contrast the integral method is helpful because it still yields finite values when the loop crosses a subgrain wall. For any particular subgrain wall the net Burgers vector content **B** depends only the length of subgrain wall intersected by the loop, and not on the loop area. In this paper we use a vector **B**/A with units of $(\text{length})^{-1}$ to characterise the GND content of any loop. For a subgrain wall, then, the magnitude of **B**/A is strongly influenced by loop area. Fig. 4 shows three loops, each intersecting the same length of subgrain wall and having the same value of **B**. The areas differ and so the magnitudes of **B**/A differ; however, the *direction* of **B**/A is not influenced by A and carries useful GND information. The advantage of the integral method for analysing subgrain walls persists when we consider spaced measurement points (section 2.3.2).

Fig. 4. Numerical aspects in of subgrain wall analysis - a sharp boundary indicated by green line, misorientation 5.6° around [001], crystal directions shown on either side with exaggerated misorientation for clarity. The 3 white boxes are used as loops to indicate the average dislocation density using the integral method (inset numbers for each box): they have relative lengths 1, 2 and 3.

So far we have assumed that all the analysed distortions are due to GNDs, but for sufficiently high angle boundaries this will not be the case. We discuss this in detail next.

*2.2.5 "High angle" boundaries and boundary dislocation content*

When can boundaries be regarded as made of GNDs? Questions emerge for high angle grain boundaries (HAGBs) where basic geometry proves that dislocations with specific Burgers vectors must be close together and may not be recognisable as discrete entities. White (1976) states "The limit is reached when dislocations are so closely spaced that they lose their individual identity and when this happens the boundary is no longer a low angle sub-grain boundary but a high angle, mobile, grain boundary. If a spacing of 2.5 nm (five lattice spacings) is taken as the minimum distance before core interference … then a low angle boundary becomes a grain boundary when the misorientation is about 10°". Trimby et al. (1998) state "Without detailed TEM [Transmission Electron Microscopy] studies the nature of a boundary can only be constrained from the nature of the misorientation across it": here "constrained" does not mean "fully described". They continue "In many studies an arbitrary misorientation value is assigned, above which boundaries are assumed to be grain boundaries and below which they are assumed to be subgrain walls although, in some cases (e.g. quartz), this value corresponds to the necessary misorientation for the overlap of dislocation cores. Typical values are 10° for quartz (White 1976), 15° or more for halite (Guillopé & Poirier 1979) and 15° for olivine (Poirier & Nicolas 1975)". Two decades later there is still a lack of clarity regarding such angles, but we discuss some relevant work next.

Shigematsu et al. (2006) coupled TEM to EBSD and showed that in quartz boundaries dislocation substructures were lost somewhere between 9° and 17°, with one 13.5° boundary still having dislocations (beyond the angular limit of 10° mentioned above). Mamtani et al. (2020) image dislocations near HAGBs in magnetite using TEM as do Zhang et al. (2020) in a Pd-10%Au alloy. So, HAGBs are not always disorganised. Kuhr and Farkas (2019) used molecular dynamics models of an FCC polycrystal and found dislocations present in some HAGBs. Twin boundaries may have dislocations e.g. p 79 of (Sutton & Balluffi 1995) but if the twin plane is perfectly oriented there are none. An attempt to apply the WBV calculation would yield an enormous and illusory dislocation density. Some HAGBs have lattices in direct contact (Marquardt & Faul 2018), others may have amorphous films nm thick (Wirth 1996). In summary, HAGBs have diverse characteristics. We cannot address that diversity here; nor can other methods of using EBSD data to deduce dislocation information. We simply assert that our calculation is interpreted assuming that the lattice curvature is due to the presence of GNDs. There is no single "cut-off" HAGB angle beyond which the GND assumption is invalid. For this reason, in the algorithms we have created the user chooses the HAGB angle above which calculations are excluded. The WBV method may in future provide useful information about HAGB structure, but further research is required.

Our models up to this point are based on algebraic descriptions of distorted lattices (see Appendix 2). We next address the finite number of measurement points that comprise an actual EBSD map, and their consequences for gradient and WBV calculations (section 2.3). We then explore the errors in orientation and their consequences for those calculations (section 2.4).

*2.3. Numerical aspects of analysing spaced EBSD measurement points*

Orientation data to be analysed are not mathematical functions of position but discrete measurements at scattered measurement points (hereafter, simply "points" for brevity). The calculation methods therefore involve numerical approximations to the gradients and integrals of the underlying theory, and the differential and integral methods have different

advantages in practice. The points in the studies we describe are on square grids, but there is no reason why the method should not be extended to hexagonal or other grids.

*2.3.1. Differential method*

The differential method uses gradients in orientation in the x and y map directions to calculate the WBV. A numerical estimation of gradients uses 2 or more orientation measurements and the distances between the points. We call the cluster of points used a "stencil" (Fig. 5a)). Here each measurement point is represented by a square with a side equal to the step size, so a stencil is illustrated as a cluster of squares. For flexibility our software allows for different stencil sizes; the differential method calculates a "best fit" lattice curvature using the orientations at each point in the stencil. Using larger stencils reduces errors in calculation (discussed later), but at the same time "smears out" microstructural details on the scale of the stencil. In published works the P = 9 stencil has usually been used; we discuss the effects of stencil size in the section on accuracy below.

Figure **5.** Stencils, orientation gradients and errors relevant for WBV. a) "Stencils" are arrangements of nearby measurement points (shown here as squares) used for numerical calculation of orientation gradients at the central point (coloured). Shown are example stencils of area 3, 5, 9 and 21. b) Illustration of effects of orientation errors. Blue graph shows a low but uniform orientation gradient (in 1D) with errors imposed. Red lines show the large effects of errors on estimating gradients over a short segment (analogous to using a small stencil). Note the estimate may even have the wrong sign. Orange line shows the improved precision using a longer segment (analogous to using a larger stencil as in a)). Inset illustrates consequent angular error in WBV direction (in 2D). The actual WBV is shown as middle arrow but with error ε (related to the gradient error) so WBV values might fall in the circle. Outer arrows illustrate the range of directions and hence the angular error δ that would arise due to these errors. c) as in b), with the same errors imposed, but for a larger orientation gradient. The errors in slope are the same as in b) but are *proportionately* less. The error ε in WBV is the same as in b) and the size of the error circle is the same for both. However, the angular error δ is smaller in c) because the WBV is longer.

In section 2.2.4 we pointed out that if a subgrain wall is considered as having zero width, it will have infinite dislocation density. Because of this numerical differentiation creates numerical artefacts as it uses spaced measurement points. The algorithm cannot distinguish a sharp orientation change between two points from a smooth orientation gradient between those points. A consequence is that if a subgrain wall is present, the apparent WBV magnitude will be finite and depend on step size, so should be interpreted with care. In practice we find that narrow "swathes" of high W are common on calculated W maps and are likely to be subgrain walls. In this case the magnitude W must be interpreted with care but the WBV direction still contains information on the Burgers vectors of the GNDs in the subgrain wall. The 3 boxes in Fig. 6 indicate the calculated W values for a sharp orientation boundary, using the differential method using stencils with areas 9, 13 and 21. Note how the dislocation density is smeared out more for larger stencils, and has apparently lower values.

Fig. 6. Numerical aspects in of subgrain wall analysis - a sharp orientation boundary indicated by green line – using the differential method. The 3 black boxes show regions in which W has been calculated using stencils of size 9 (top), 13 and 21. Compare Fig. 4 which uses the integral method on the same boundary.

451

452 *2.3.2. Integral method*

453 The integral method involves integrating the orientation tensor around a closed loop in the
454 map plane, directly giving the net Burgers vector sum for all the dislocation lines threading
455 through that loop. The details of numerical integration are given in Supplementary
456 Information 1.2. Publications to date have restricted loop shapes to rectangles, though there is
457 no fundamental difficulty in implementing other shapes and this has been done in a
458 commercial version of the algorithm in the Oxford Instruments Aztec system. The result of
459 integration is a vector **B** with dimensions of length. We divide this by the loop area A to get a
460 vector in $(\text{length})^{-1}$ which is more easily compared to results of the differential method.
461 Algebraically, the vector **B/**A must equal the average **W** value in the loop (eqn. (6)).
462 Numerically, the "best fit" algorithm used in the differential method means the methods may
463 give slightly different results; for subgrain walls the integral method remains advantageous
464 (c.f. section 2.2.4).

465 In Wheeler et al. (2009) the integral method was presented as an exploratory tool in which
466 the user drew rectangular loops and the WBV was reported as a lattice vector (e.g. Fig 3e),
467 f)). More recently a method of systematically "tiling" the map with square loops, and
468 applying the integral method to each loop was used in Fig. 8c of Timms et al. (2019). The
469 tiles can be displayed colour coded by standard IPF colour schemes using a W threshold, in
470 the same way as for calculations made with stencils (examples are given later). The tiles can
471 be thought of as large pixels, though not all properties are precisely analogous to those of
472 individual measurement points. In all circumstances, if the loop crosses a high angle
473 boundary, then a WBV can in principle be calculated but as discussed above, has no meaning
474 - so instead the algorithms we use do not return a result and the tile is left uncoloured.

475 *2.4. Numerical aspects of dealing with orientation measurement errors*

476 Orientation measurements used may be in error as a result of errors in the Hough transform,
477 up to a degree at most (Prior et al. 2009); for one study on an Si single crystal, was 0.2° (Ram
478 et al. 2015). Improved "real time" approaches to indexing Kikuchi patterns reduce the
479 angular error in orientations to <0.05° (Nicolay et al. 2019). For higher angular resolution
480 methods, e.g. correlating Kikuchi patterns, errors may be as low as ~0.0003 radians (Wallis et
481 al. 2019a). The differential method uses gradients in crystal orientation to calculate WBV. On
482 the grid of measurement points, a gradient is calculated from the misorientations between
483 adjacent measurements. The misorientation angles are likely to be small and so the errors in
484 misorientation axes will be large (Prior 1999) and these errors will propagate into the WBV
485 calculation. An algebraic analysis would involve error propagation through operations on
486 various orientation tensors and is beyond the scope of this contribution; instead, we use
487 simple arguments followed by some numerical experiments.

488 *2.4.1. General nature of error effects*

489 We argue in this section that angular errors in WBV are smaller for long WBVs. Longer
490 WBVs are linked to higher lattice curvatures. Higher lattice curvatures mean the
491 misorientation angles between adjacent pixels are larger, and the misorientation axes will

have smaller errors, and the WBV direction will have smaller errors. We illustrate this assuming a typical orientation error of 0.01 radians.

Benchmark curvature (above which calculation will be less error prone) ~ 0.01/(step size)

and in terms of magnitude

|WBV| ~ curvature

which means we should consider a benchmark below which WBV is error-prone as

$|WBV| \sim 0.01/(\text{step size}) = W_t$

This approach is similar to the derivation of eqn. 13 of Wilkinson and Randman (2010) and eqn 2 of Jiang et al. (2013), where a lower limit on detectable dislocation density is given in terms of step size:

(Minimum detectable GND density) ~

(Angular resolution) /((step size) * (Burgers vector length) )

For example 0.01 /( (1 micron) * (5 angstrom) ) = 2 x $10^{13}$ $m^{-2}$

The approach described below is related because in order of magnitude, $W = \rho b$. Hence our $W_t/b$ equates to the minimum detectable GND density discussed in other work. That work, and others (by the group) focusses on accuracy in determining dislocation *density*; here we also analyse WBV *direction* since it plays a key role in several studies (Table 1). In Wheeler et al. (2009) we argued that longer WBVs would be more accurate in terms of direction. For example, the map of Mg used in Fig. 2 and 3 of Wheeler et al. (2009), modified in Fig. 7, has a step size of 4 μm so $W_t = 0.0025$ $\mu m^{-1}$. Fig. 7 shows considerable scatter for $W > 0.002$ $\mu m^{-1}$ and much less for $W > 0.004$ $\mu m^{-1}$, in accordance with the argument that $W_t$ offers a guide to judging precision. Guided by this, our approach to displaying WBV data involves selecting data based on ranges of W. The minimum value $W_{min}$ in the range will be associated with the maximum angular error. Setting it high will reduce error. The maximum value $W_{max}$ is less important but is useful for dividing up datasets.

| |
|---|
| Figure **7.** IPFs of Mg WBV displayed using three different thresholds: threshold lengths and numbers of points as indicated, modified from Fig. 3 of Wheeler et al. (2009). |

Figure 5b) and c) are non-rigorous illustrations of error effects. The graphs illustrate that larger stencils will give better precision. Errors ε in gradients are independent of the gradients themselves but for larger orientation gradients (as in Fig. 5c)), longer WBVs) the errors are *proportionately* less important. The insets in b) and c) illustrate the consequent effects on angular errors. The errors in WBV are now drawn as circles around the actual values since errors may be in any direction. The error circles are the same size in b) and c). The green arrows mark the vectors with maximum angular error δ, showing that longer WBVs in c) will have smaller angular errors. In the next section we analyse error effects using numerical models.

*2.4.2. Specific analyses of error effects*

It is useful to quantify error estimates for WBV, incorporating the effects of WBV length and other parameters. We define an angle $\alpha_{95}$ so that there is a 95% chance that the true WBV direction is that angle or less from the calculated direction, an approach used in analysing palaeomagnetic data for example Butler (1992). In essence $\alpha_{95}$ defines a cone of directions within which the true direction is likely to be. This is analogous to the $\pm 2$ standard deviation range within which 95% of the data lie when dealing with a one-dimensional normal distribution. Our approach gives the angular error for the WBV in sample coordinates: it is in principal the same for crystal coordinates except crystal symmetry may modify the interpretation, as addressed in Appendix 3.1.

EBSD orientation errors will depend on mineralogy, acquisition conditions and indexing methods and will propagate in the WBV calculations. For illustration we create model orientation maps with angular errors in orientation up to 0.57° (0.01 rad) – so our angular error estimates for WBVs are likely to be pessimistic. We used theoretical models shown in Fig. 3 with added orientation noise, and calculated **W** for the noisy datasets. Larger stencils and tiles take into account more orientation measurements and, in common with other averaging methods, we hypothesised in Wheeler et al. (2009) that this would give higher precision. We examine this idea in Appendix 3. First, we calculate the error on WBV, by comparing actual **W** and theoretical $\mathbf{W}_c$ values. We find that the error in WBV magnitudes $\mathbf{E} = \mathbf{W} - \mathbf{W}_c$ are not strongly dependent on length W, or on whether the model is tilt or twist, but they do depend on stencil size. To quantify the errors, we calculate a standard deviation $\sigma$ for the vector **E** as described in Appendix 3. Larger stencils and tiles give smaller errors (Fig. 6). So, if one uses stencils (i.e the differential method), there is an approximate relationship between W precision and the area S of a stencil (number of points, hence dimensionless)

$$\sigma_S = 0.0247 S^{-1}/u \qquad (7)$$

where *u* is step size.

If one uses tiles (i.e. the integral method) and defines the dimensionless area T of a tile the standard deviation $\sigma_T$ of vector E is:

$$\sigma_T = 0.0081 T^{-3/4}/u\ . \qquad (8)$$

Figure **8.** a) Standard deviation σ of nondimensionalised WBV magnitude plotted against calculation region size for tilt and twist models, showing errors are independent of the detailed nature of distortion. The three left-hand points are for stencils, the others are for tiles. b) Same, plotted against areas of stencils and tiles for both tilt and twist models. c) Same as b) but plotted as log-log graphs to show linear relationships.

In Wheeler et al. (2009) we suggested that the integral method would have higher precision than the differential method because numerical integration is less sensitive to errors than numerical differentiation. Our assertion was correct because we were using small stencils (P = 9) and large integral loops. Fig. 8 b) and c) show that in fact the precision depends mainly on the area of the tile or stencil used. The integral method remains our favoured method for initial exploration since the calculation is much faster than for a stencil of comparable size.

563 The second stage of error analysis involves the angular errors. These *do* depend on the length
564 W as described above and in Fig. 8. The inset in Fig 5c) suggests that $\delta \approx \varepsilon/W$ when errors
565 are small. This is in accord with Fig. S1. One might then expect some proportionality
566 between measures of vector error $\sigma$ and angular error $\alpha_{95}$ in a more rigorous approach, and
567 this is confirmed in Appendix 3. For small errors we have

568 $$\alpha_{95} \cong 1.413\frac{\sigma}{W}$$

569 For example, in Table 1, for the second Mg example we have a step size of 4 μm and
570 calculated the WBV using a stencil area 9 so $\sigma_s = 0.000686$ μm$^{-1}$. For a WBV length 0.004
571 μm$^{-1}$ we have

572 $$\alpha_{95} \cong 1.413\frac{0.000686}{0.004} = 0.24\,rad = 13.8°$$

573 (the table calculation is more precise). If we compare the calculated $\alpha_{95}$ with Fig. 7c), it is
574 plausible that the dislocations are all basal and we see a scatter up to 14° away from the basal
575 plane, broadly in accord with the calculation. The above assessment of precision should be
576 used with caution, since it assumes a particular range of orientation errors in the measured
577 data, and those errors are dependent on acquisition conditions and the mineral being
578 measured. A larger stencil or tile will give a more precise measure of WBV magnitude and
579 direction, but larger regions are also more likely to contain more than one type of dislocation.
580 There is a trade-off between finding a relatively precise WBV direction in a large region that
581 may contain more than one type of GND, versus finding a less precise direction in a smaller
582 region which may relate to a single type of GND.

583 Our error analysis is numerical rather than algebraic but simple calculations give confidence
584 that, if other parameters are maintained, the WBV angular error will scale linearly with
585 orientation angular error. Thus, if angular errors are distributed uniformly between 0 and
586 0.001 rad, we expect angular errors in WBV to be 10 times less than those we present here.
587 Such low indexing errors are now routinely possible, albeit with a trade-off on indexing
588 speed (Nicolay et al. 2019). Improved indexing would allow for use of a smaller stencil or tile
589 ensure a particular level of WBV precision. We note that algorithms that assign interpolated
590 orientations to misindexed or non-indexed pixels may have adverse effects on subsequent
591 WBV calculations. For example, if the orientation value of an adjacent pixel is used, this
592 guarantees that there is a zero orientation gradient between those two pixels, which may have
593 a big (and spurious) influence on the WBV calculation. Ideally, analysis is done only on
594 confidently indexed points. We also urge caution using dictionary indexed EBSD maps (De
595 Graef 2020) for WBV calculations, because the orientations stored in the dictionary of
596 Kikuchi patterns are discrete and orientation gradients therefore will be stepped. This may
597 give a spurious influence on WBV calculations.

598 **3. WBV applications in Earth Sciences: examples**
599
600 The published works in Table 1 show a variety of approaches for interpreting WBV. The
601 basic algorithms we use do *not* decompose the WBV down into individual Burgers vectors
602 because to do this requires additional assumptions, dependent on the particular mineral and
603 its microstructural evolution. For example, a WBV parallel to [100] may result from a single

population of GNDs with Burgers vectors parallel to [100], or a mix of dislocations with [110] and [1-10]. In some phases, prior knowledge of likely Burgers vectors will mean there is only one choice for decomposition – e.g. if such a WBV is found in olivine. In the following, we present first two new examples of WBV usage and then comment on published examples.

Figure **9.** Example of WBV applied to olivine. a) IPF map of Y direction of deformed single crystal of olivine. Scale bar is 1000 μm. b) IPF key. c) IPF coloured as in a), showing a few degrees of distortion within a single initially undeformed crystal. d) WBV magnitude map calculated on 10 x 10 tiles. e) IPF map of WBV direction (calculated as in (d)) superimposed on a band contrast greyscale map; minimum length 0.001 $\mu m^{-1}$. f) IPF of WBV as in (e). g) WBV magnitude map calculated on 3 x 3 stencils in part of overview map shown as white box in (d). Scale bar is 1000 μm. Inset shows orientation variation (degrees) from left hand end of transect marked by white line. h) IPF map of WBV direction (calculated as in (g)) superimposed on a band contrast greyscale map; minimum length 0.00005 $\mu m^{-1}$, showing subgrain walls with [100] Burgers vectors running NE and those with [001] running NW. White squares indicate results of the integral method, with numbers in $\mu m^{-2}$ expressed as coefficients of crystal basis vectors (K values). i) IPF of WBV as in (h).

*3.1. Olivine: subgrain wall analysis free from trace, or tilt or twist assumptions*

Fig. 9 shows an experimentally deformed single crystal of olivine (PI-1766) as in Fig. 8 of Tielke et al. (2017). The experiment was set up so that the Y (shortening) direction was initially parallel to $[101]_c$, at 45∘ to [100] and [001], with an expectation that slip systems with [100] and [001] Burgers vectors would be activated. The orientation map (a) shows the crystal direction that is parallel to the Y sample direction, in accord with the IPF key (b). We refer to such maps as "IPF Y maps" below. The colour variations reveal rather straight subgrain walls running in two directions. Orientations vary over a few degrees (c). Fig 9(d) shows 10 x 10 tiles colour coded by WBV magnitude and (e) by direction, superimposed on the band contrast greyscale map. The size of the tiles reduces $\alpha_{95}$ but the threshold length for display is set low, at 0.00005/μm, so $\alpha_{95}$ is 26°.With this in mind, the IPF Fig 9f) is, within error, in accord with a mix of dislocations with [100] and [001] Burgers vectors, and the dominant blue colour on the map indicates mainly [100]. Figs (g) and (h) show a subarea with WBV now calculated using a 3 × 3 stencil, giving less precision but more spatial resolution and revealing individual subgrain walls. Blue subgrain walls running NE are consistent with being [100] tilt boundaries and red subgrain walls running SE are consistent with being [001] tilt boundaries. A higher threshold length for display (0.001/μm) means $\alpha_{95}$ is 14° and the IPF in Fig. (i) is in accord with that, insofar as most points are within 14° of the plane containing [100] and [001]. There are still mixtures of [100] and [001]. Some will result from where the stencil overlapped subgrain wall junctions, but as Fig. (h) shows, these mixtures also appear along irregular segments of the NW-SE subgrain walls and are likely to represent two types of GND in an individual wall. The three square "loops" show results of the integral method and provide additional illustration of how the WBV is averaged over the sample area. Each triplet of numbers is a list of K values, i.e. the coefficients defining the WBV when it is expressed in crystal basis vectors (eqn (5)). The numbers have the

dimensions of dislocation density but must be interpreted with care, as discussed above and shown in Fig. 4, since the dislocations are in discrete walls.

In this example the directional information is more useful than the density information: integral and differential methods both give information about where GNDs with [100] and [001] occur. Note that examining the subgrain wall traces together with misorientation axes deduced from the distortion (Fig. 9c) could yield similar results. However, that approach would involve manual and subjective selection of boundary segments and of subregions from which to use misorientation data; it would be based on assumptions about pure tilt or twist boundary character and errors would be difficult to assess. Use of WBV does not preclude further analysis (e.g. Wieser et al. (2020)) but provides a firm foundation.

*3.2. Plagioclase: distributed deformation analysis free from slip system assumptions*

Fig. 10 shows plagioclase from a deformed gabbro from close to the slow spreading mid ocean ridge in the SW Indian Ocean (sample ODP 176-735B-95R-2 from approx. 546 m below the ocean floor). The plagioclase is highly strained, with two prominent ribbons bent around an augite porphyroclast (grey scale on right). Trails of smaller grains are interpreted as new grains due to recrystallization. Hornblende marginal to pyroxene suggests deformation is amphibolite facies, as recorded deeper in the leg (Gardner et al. 2020), but it may have been higher temperature. Our aim here is to not to offer a full interpretation of how the microstructure evolved, but to show how the WBV tools assist in that task.

Figure **10.** Example of WBV applied to plagioclase. Figure layout is similar to Fig. 9 but contouring is used to reveal dominant directions. a) IPF map of plagioclase Y direction of a deformed gabbro. Inset shows orientation variation (degrees) from top end of transect marked by white line. The right-hand porphyroclast is augite rimmed by hornblende. b) Key for IPF map colour scheme. c) IPF map of plagioclase as in a), contoured with intervals at 0.1 x uniform. d) Magnitude of WBV calculated on 20 x 20 tiles in area a) superimposed on a band contrast greyscale map. e) IPF map of WBV calculated as in d) colour coded by WBV direction using b), minimum length 0.0005 $\mu m^{-1}$. f) IPF of WBV as in d) and e), contoured in multiples of uniform. g) Magnitude of WBV calculated on 3 × 3 stencils in white box subarea of map d) superimposed on a band contrast greyscale map. h) IPF map of WBV calculated as in g) colour coded by WBV direction as in b), minimum length 0.01 $\mu m^{-1}$. i) IPF of WBV as in g) and h).

The IPF Y map (Fig. 10a), colour coded as in 10b)) indicates rather smooth variations in orientation for the large grain, in contrast to the olivine example Fig. 9a). Large tiles used in Fig 10d) confirm this, showing a rather uniform level of distortion on the scale of the tiles through the two ribbons. The WBV IPF map (Fig. 10e)) shows <100> dominates at the top of the left hand ribbon, whilst <001> dominates at the bottom, and the IPF (Fig. 10f)) combines these. In and around new grains no data is displayed (Fig. 10d and e) because the 20 × 20 pixel tiles are large enough to cover several small grains and include high (> 5°) angle boundaries. Thus, in these areas WBV analysis is not appropriate. It is worth considering whether the apparent variation in WBV direction is a stereological effect, like that shown in Fig. 3h), j). Could the ribbon have a relatively uniform population of GNDs, but with a stereological bias governed by varying orientation? The misorientation from bottom to top of (for example) the left-hand ribbon is about 35° in contrast to Fig. 3h), j) which involved 90°

of twist. We conclude it is likely that there are real variations in the GND population in this grain, which is not surprising given the stretch and non-uniform bending it has enjoyed. Fig 10g)-i) shows WBV calculated using the differential method on a subarea marked with a white box in Figs. 10d and e. In Fig 10g), boundaries above 5° are shown in black and the highest distortions i.e. WBV magnitude are shown not in the large ribbons but in small grains interpreted as products of dynamic recrystallization. Fig. 10h) and i) show WBV direction, with a pronounced maximum close to <001> as illustrated by the preponderance of red colours in new grains in (h) and a contoured maximum near <001> in (i). The relict ribbon in centre right of Fig. 10h) shows two left-right tapered zones coloured green, indicating WBV rather close to <-100> and in accord with the tiling in Fig. 10e).

In summary this example shows how the integral (here, tiling) and differential methods may be used to interrogate different parts of the microstructure. The interiors of the plagioclase ribbons have relatively low dislocation densities, with GNDs with Burgers vectors combining <100> and <001>, likely in different proportions in different parts. Here, the integral method is a very effective tool. For the small grains, interpreted as recrystallized, the differential method is helpful; they have higher dislocation densities and various Burgers vectors but with an emphasis on <001>. In tectonites small grains are often interpreted as new, forming by static or dynamic recrystallisation from strongly plastically deformed large old grains, and are relatively strain free. Intriguingly, here the small grains are more distorted than the old ribbons though normally one would expect them to be relatively strain free. Further WBV investigation will assist in understanding the evolution of that microstructure. Methods including the traces of subgrain walls could not be used here, since distortion is distributed; methods assuming slip systems and dislocation line energies could be applied but the required inputs may be difficult to constrain in a mineral like plagioclase. As in the olivine example, we suggest the WBV approach provides a firm foundation on which other analyses can be built if required.

### *3.3. Ice: investigation of non-basal slip*

Figure **11.** Example of WBV applied to a subgrain in ice, modified from Fig. 2 of Chauve et al. (2017). WBV is colour coded not by the full IPF but just by the sin of the angle of the WBV from the basal plane, i.e. (component of W parallel to c)/W. This runs between 0 and 1 as shown by the colour scale. Red arrows show the WBV projected onto the map plane, using its actual length not just its direction. Black line is a subgrain wall of 5° or more misorientation.

There is ongoing research into the role of non-basal slip in ice, since if that is active it will alter the rheology of ice sheets (Chauve et al. 2017, Piazolo et al. 2015, Weikusat et al. 2011). Chauve et al. (2017) undertook deformation experiments on ice and Fig. 11a), modified from Fig. 2 of that paper, shows a subgrain from an experiment run at -7 °C and 0.5 MPa stress. The WBV is colour coded not by the full IPF but just by the sin of the angle of the WBV from the basal plane, i.e. (component of W parallel to c)/W. For this dataset we estimate $\alpha_{95}$ as 32° (Table 1). The yellow vertical subgrain wall indicates angles near 90° from the basal plane so, even though the errors are large, there is negligible probability that these WBVs lie in the basal plane. Moreover, the colours along this wall are quite consistent, adding credence to the diagnosis that the WBV is subparallel to c. It does not immediately imply that

individual Burgers vectors are parallel to c: for example, there could be a mixed population of c + a and c - a, bearing in mind the WBV is a vector average. Further data and/or assumptions are required to determine this. However, as noted above the WBV cannot contain "phantom" directions: it must be the weighted average of Burgers vectors that are actually present in the microstructure, and here must include non-basal vectors of some sort. The Figure also provides an example of WBVs drawn in red as vectors in sample coordinates. As discussed above and derived in Appendix 1, there is only one such choice at each point, regardless of crystal symmetry. Despite $\alpha_{95}$ being predicted as 32°, the WBV directions along each wall segment are quite consistent, suggesting the angular errors are in fact lower, though further work is required to confirm this.

*3.4. Titanite: discovery of new slip system*

Fig. 12 shows the use of tiling in a study of deformed titanite, modified from Timms et al. (2019). The titanite grain is from a shocked granitoid from the Chicxulub impact structure, Mexico, and the study searched for slip systems activated under extreme stresses, which would not necessarily correspond to slip systems documented from other settings. The study included a boundary trace/misorientation approach, but that assumed pure tilt boundaries, so the WBV method was used for independent verification. The differential method gave a wide scatter of WBV directions so to reduce errors 20 × 20 pixel tiles were used. The tiles are colour coded in terms of IPF direction; missing colours indicate either that the tile includes a high angle boundary, or the WBV magnitude is below the threshold for display (Table 1). There are many shock-induced twins, and the abundance of those high angle boundaries mean that tile coverage is sparse. However, the WBV directions show a strong maximum near <341>. This is a Burgers vector not previously described in titanite but likely indicating a dislocation slip system operating concurrently with twinning under shock.

Figure **10.** Example of WBV applied to titanite. The greyscale map is of band contrast in a shocked titanite grain and its surroundings, redrawn from Fig. 8 of Timms et al. (2019). Inset shows orientation variation (degrees) from lower left end of transect marked by thick black line. Tiling was used to analyse the microstructure – tiles are coloured for WBV direction in accordance with the IPF key on bottom left. The WBV IPF (top right) shows distinct preferred directions. Calculation and display parameters are given in Table 1.

*3.5. WBV precision in specific studies*

In Table 1 we compile the parameters required for estimating $\alpha_{95}$ from previous studies making a big assumption, that the orientation measurement errors in those studies are all distributed uniformly between 0 and 0.01 radians. Despite this, the error estimates are in general agreement with the appearance of the relevant IPFs. For example, for Mg metal Fig. 7 shows IPFs with $\alpha_{95}$ of 28° and 14°, and those angles are in accord with the scatters of points if all WBVs are in fact in the basal plane. One large $\alpha_{95}$ = 110° is for quartz and relates to Fig. 15 of Wheeler et al. (2009), but the left hand IPF there was drawn to specifically illustrate the effect of choosing a threshold W that is too low. The cone of error would cover the entire IPF and that is in accord with the random scatter of points seen. In contrast, another study is predicted to have a large $\alpha_{95}$ of 110° yet the IPFs show strong maxima. Fig. 4 of Kendrick et al. (2017) shows IPFs of WBV for deformed plagioclase microlites in an andesite with strong maxima around [001], particularly in the experimentally deformed sample. We

743 suggest this is because there is a single family of GNDs with a single [001] Burgers vector.
744 Then, even though individual WBVs have large errors, the maximum is strong because the
745 errors cancel out to some extent. This is analogous to a standard result in statistics of a single
746 variable: the standard variation of the mean is equal to the standard deviation of an individual
747 measurement divided by the square root of the sample size. A similar idea might be
748 developed for directional statistics in future work.

749 **4. Comparison of WBV with other methods used for analysing GND directional data**
750 All 6 orientation gradients (3 in x and 3 in y) can be calculated from EBSD maps and provide
751 6 constraints on the Nye curvature tensor as in (Pantleon 2008), Wilkinson and Randman
752 (2010), Wallis et al. (2016). If there are 6 types of dislocation, then eqn (3) has a unique
753 solution for 6 GND densities, given the 6 constraints on the Nye tensor. In many materials,
754 particularly cubic phases, symmetry indicates there are more than 6 types of slip system and
755 there is no unique solution for eqn (3). So, an additional assumption is made, that the total
756 line energy of all the dislocations involved is the minimum out of all the possible solutions.

757 This approach uses more information than the WBV method (6 components of the Nye tensor
758 versus 3) but is based on assumptions that we recommend deserve appraisal on a mineral-by-
759 mineral basis.
760 i) Assumptions about allowable slip systems might be misleading as we do not have a
761 complete knowledge of all in all minerals.
762 ii) Assumptions about the line energies of each type of dislocation, to enable overall
763 energy minimisation if there are more than 6 slip systems, will be based on limited
764 information for minerals.
765 iii) Assuming that the types of dislocation related to slip also characterise growth defects
766 deserves scrutiny. For growth the concept of slip systems is not relevant: there might be
767 alternative lists of allowable GND types, but again in minerals such information is scanty.
768 iv) Assuming that dislocations have locally reorganised to minimise their net energy may
769 not be true (e.g. in cold working, or when defects are due to growth).
770

771
772 In contrast WBV calculation makes no assumptions about GND types at any stage of the
773 calculations. Instead, individual studies tailor the interpretation, possibly involving further
774 calculation, based on the problems being addressed. This is well illustrated in the published
775 ice non-basal slip example outlined above. Here, the hypothesis to be tested was to identify if
776 non-basal dislocations are present in ice, tested by calculating and displaying the angle of the
777 WBV to the basal plane (Chauve et al. 2017). The calculation is free from detailed
778 assumptions about dislocation types and energies, which are not well known. A further
779 example is provided in Wieser et al. (2020) who used the trace of subgrain walls together with
780 WBV analysis to provide additional constraints on potential activated slip systems. In this
781 case, additional assumptions were introduced, e.g. that all subgrain walls were either pure tilt
782 or pure twist. Those assumptions are not intrinsic to the WBV calculation. In essence the
783 WBV may provide sufficient information on its own and provides a platform for further in-
784 depth analysis which may use additional assumptions.

785 In a number of works using the "energy minimisation" method, the EBSD data are high
786 resolution electron backscatter diffraction (HREBSD) which gives higher angular accuracy to

orientation measurements: for details see Wilkinson and Randman (2010), Wallis et al. (2016) and Wallis et al. (2019a). This means that errors in misorientation gradients and hence WBV or other calculations will be lower than using conventional data (Gardner et al. 2024). However, there is no intrinsic difference in applying WBV or energy minimisation calculations to HREBSD versus conventional data or to data obtained with new techniques e.g. (Winkelmann et al. 2020). WBV can be calculated from HREBSD data, as in Wallis et al. (2016) and Gardner et al. (2024). Equally, best fit/energy minimisation can be used on Hough based orientation data as in Pantleon (2008).

## 5. Summary and discussion

We have described the theoretical basis for the WBV method and shown examples where it has assisted in deducing Burgers vectors for slip systems in various minerals. Since the method is purely geometric it can also be used to analyse distortions due to growth as in Gardner et al. (2021). Key aspects of the WBV method are as follows.

- It makes no assumptions about the dislocation populations being investigated.
- It uses just the three numbers defining orientation at each measurement point, so is fast.
- It assumes there are no significant grain scale elastic strains.

The software we use in this contribution ("Crystalscape") involves user-defined parameters for calculation as follows; these need to be recorded to allow calculations to be reproduced.

- The cutoff angle above which boundaries are assumed to no longer have dislocation substructure.
- The size of the stencil or tile used for systematic calculations.

WBV results can be displayed in several ways and the key user-defined parameters for display are the minimum and maximum WBV lengths. The minimum length can then, together with the other parameters, be used to estimate the angular accuracy $\alpha_{95}$ (the shortest vectors being the least accurate in terms of direction). That estimation contains several simplifications and, in any case, depends on an assumed angular error in the EBSD data; but it serves as an indication of accuracy which proves useful.

For interpretation, the following properties must be borne in mind.

- The WBV does *not* measure the complete GND population or density. It is a sample of that population, weighted towards dislocation lines that intersect the EBSD map at high angles. Maps cut in different planes will show different but related WBV information.
- The WBV is a weighted sum of Burgers vectors of GNDs. In general, there are multiple ways of decomposing the WBV, but it still provides a platform for testing hypotheses. It will never generate "phantom" components. For example, if a trigonal or hexagonal mineral shows WBVs with significant c axis components, there must be GNDs with Burgers vectors involving c (though not necessarily parallel to c).
- Errors in WBV are smaller when larger stencils or tiles are used. Angular errors are smaller for longer WBVs.
- Larger stencils or tiles tend to "smear out" the WBV pattern. Increased angular precision is thus linked to reduced spatial resolution.

Future directions using this method could include further development of ways to characterise non-basal slip in hexagonal and trigonal materials e.g. Chauve et al. (2017). The combination of WBV analysis with subgrain boundary trace analysis (Wieser et al. 2020) has potential to be developed for olivine and other minerals. More advanced statistical tests related to directional data could be developed. We have not discussed 3D orientation data here but in principle this allows calculation of orientation gradients in all three dimensions and hence the complete Nye tensor which would be valuable for constraining GNDs. However, even the 9 components of the Nye tensor are not sufficient to constrain all GND types in very symmetric minerals. Statistical tests could be developed for 3D analysis as we have done in 2D. Hybrid approaches using two or more maps at right angles also deserve investigation.

We note that the methods discussed here are applicable to any crystalline material including metals, ceramics and ice.

The Matlab software used for analysis here ("Crystalscape") is available from the lead author for academic use only. In 2021 Oxford Instruments Nanoanalysis adapted a version of the WBV method for use in Aztec Crystal, their EBSD analysis suite. This is described here: https://www.ebsd.com/ois-ebsd-system/dislocation-density-analysis and in a webinar here https://register.gotowebinar.com/register/5472775566652982031.

**Credit author statement**

**John Wheeler:** Conceptualization, Software, Writing - Original Draft, Visualization; **Sandra Piazolo:** Conceptualization, Writing – Review and Editing; **David Prior:** Conceptualization, Writing – Review and Editing; **Patrick Trimby:** Conceptualization, Resources, Writing – Review and Editing; **Jake Tielke:** Resources, Writing – Review and Editing.

**Acknowledgements**

We thank all the user of the WBV method who have contributed through discussion to developing the method. We thank Elena Miranda and David Wallis for constructive reviews and Virginia Toy for substantial editorial work.

**Table 1. Details of published WBV studies, and the new studies here**

Table 1. Published papers using WBV on minerals, with precision estimates added in this contribution. We include one example of use on Mg metal as it helps illustrate the basic ideas. In the right hand columns we have compiled information from the published works to estimate $\alpha_{95}$ based on the assumption that orientation measurement errors are distributed uniformly between 0 and 0.01 radians, a realistic if somewhat pessimistic range for data obtained by Hough transform.

| Crystal system | Laue group | Phase | weighted Burgers vector study motivation | Reference | Figure in referenced paper | Integral method used? | Stencil or tile | Sampled area (pixels) | Step size (μm) | W minimum length ((μm)$^{-1}$) | $\alpha_{95}$ (deg) |
|---|---|---|---|---|---|---|---|---|---|---|---|
| Cubic holosymmetric | m3m | Periclase | example | (Wheeler et al. 2009) | Fig 11 | | s | 9 | 10 | 0.0015 | 14.9 |
| Cubic | m3 | | ***no studies yet published on minerals*** | - | | | | | | | - |
| Hexagonal holosymmetric | 6/mmm | Mg | example | (Wheeler et al. 2009) | Fig 3, 5 | | s | 9 | 4 | 0.002 | 28.1 |
| | | Mg | example | (Wheeler et al. 2009) | | | s | 9 | 4 | 0.004 | 13.9 |
| | | Ti | magnitude display from TKD data | (Trimby et al. 2014) | Fig 5 | | | | 0.01 | | n/a |
| | | Ice | search for non-basal dislocations | (Piazolo et al. 2015) | | | s | 9 | 15 | 0.0004 | 37.7 |
| | | Ice | search for non-basal dislocations | (Chauve et al. 2017) | Fig. 2 | | s | 9 | 5 | 0.0014 | 32.2 |
| | | Ice | intragranular boundary development | (Fan et al. 2022) | Fig. 5 | | s | 9 | 5 | 0.006 | 7.4 |
| Hexagonal | 6/m | | ***no studies yet published on minerals*** | - | | | | | | | - |
| Trigonal holosymmetric | -3m | Quartz | example | (Wheeler et al. 2009) | Fig 15 | | s | 9 | 2 | 0.001 | 110.0 |
| | | Quartz | example | (Wheeler et al. 2009) | Fig 15 | | s | 9 | 2 | 0.003 | 37.7 |
| | | Quartz | compare GND density with density from etch pits | (Billia et al. 2013) | n/a | y | | | | | n/a |
| | | Calcite | deduce slip systems hence deformation T | (Mcnamara et al. 2020) | Fig 4, 5 | | | | | | |
| Trigonal | -3 | | ***no studies yet published on minerals*** | - | | | | | | | |
| Tetragonal holosymmetric | 4/mmm | Zircon | Link magnitude to Pb loss | (MacDonald et al. 2013) | Fig. 9 | y | | | 1, 2, 0.8 | | n/a |
| | | Zircon | Planar deformation bands | (Kovaleva et al. 2015) | Fig. 6 | y | | | | | n/a |
| | | Zircon | help to characterise slip systems | (Kovaleva et al. 2018) | Fig. 6 | y | | | | | n/a |
| Tetragonal | 4/m | | ***no studies yet published on minerals*** | - | | | | | | | - |
| Orthorhombic | mmm | Olivine | confirm slip systems dominated by [100] | (Tielke et al. 2019) | Fig. 5 b | y | s | 9 | 3 | 0.005 | 14.9 |
| | | Olivine | determine slip systems | (Wieser et al. 2020) | Fig. 4, 7 | | | | | | |
| | | Olivine | tiling example | ***this contribution*** | Fig. *7* | y | t | 100 | 16 | 0.00005 | 26.2 |
| | | Olivine | stencil example | ***this contribution*** | Fig. *7* | | s | 9 | 16 | 0.001 | 13.9 |
| Monoclinic | 2/m | Titanite | Diagnose slip systems: map showing WBV direction (6 μm tiles) | (Timms et al. 2019) | Fig. 8c | | t | 400 | 0.3 | 0.001 | 24.6 |
| | | Titanite | Contoured IPF showing WBV direction (2.4 μm tiles) | (Timms et al. 2019) | Fig. 8e | | t | 64 | 0.3 | 0.003 | 32.6 |
| Triclinic | -1 | Plagioclase | Diagnose slip system in naturally and experimentally deformed microlites; latter show [001] clearly; both show it in loops | (Kendrick et al. 2017) | Fig. 4 | | s | 9 | 0.2 | 0.01 | 110.0 |
| | | Plagioclase | Understand plagioclase replacement by albite | (Gardner et al. 2021) | Fig. 6 | | s | | | | |
| | | Plagioclase | tiling example | ***this contribution*** | Fig. *8* | y | t | 400 | 1 | 0.0005 | 14.7 |
| | | Plagioclase | stencil example | ***this contribution*** | Fig. *8* | | s | 21 | 1 | 0.01 | 9.5 |

## References


Ashby, M. F. 1970. Deformation of plastically non-homogeneous materials. *Philosophical Magazine* **21**(170), 399-424.

Billia, M. A., Timms, N. E., Toy, V. G., Hart, R. D. & Prior, D. J. 2013. Grain boundary dissolution porosity in quartzofeldspathic ultramylonites: Implications for permeability enhancement and weakening of mid-crustal shear zones. *Journal Of Structural Geology* **53**, 2-14.

Butler, R. F. 1992. *Paleomagnetism: Magnetic Domains to Geologic Terranes*. Blackwell Scientific Publications.

Chauve, T., Montagnat, M., Piazolo, S., Journaux, B., Wheeler, J., Barou, F., Mainprice, D. & Tommasi, A. 2017. Non-basal dislocations should be accounted for in simulating ice mass flow. *Earth And Planetary Science Letters* **473**, 247-255.

Das, S., Hofmann, F. & Tarleton, E. 2018. Consistent determination of geometrically necessary dislocation density from simulations and experiments. *International Journal Of Plasticity* **109**, 18-42.

De Graef, M. 2020. A dictionary indexing approach for EBSD. *IOP Conference Series: Materials Science and Engineering* **891**, 012009.

Drury, M. R. & Urai, J. L. 1990. Deformation related recrystallization processes. *Tectonophysics* **172**, 235-253.

Fan, S., Wheeler, J., Prior, D. J., Negrini, M., Cross, A. J., Hager, T. F., Goldsby, D. L. & Wallis, D. 2022. Using misorientation and weighted Burgers vector statistics to understand intragranular boundary development and grain boundary formation at high temperatures. *Journal of Geophysical Research - Solid Earth* **127**(8), 26 pages.

Gardner, J., Wallis, D., Hansen, L. N. & Wheeler, J. 2024. Weighted Burgers Vector analysis of orientation fields from high-angular resolution electron backscatter diffraction. *Ultramicroscopy* **257**, 113893.

Gardner, J., Wheeler, J. & Mariani, E. 2021. Interactions between deformation and dissolution-precipitation reactions in feldspar at greenschist facies. *Lithos* **396-397**.

Gardner, R. L., Piazolo, S., Daczko, N. R. & Trimby, P. 2020. Microstructures reveal multistage melt present strain localisation in mid-ocean gabbros. *Lithos* **366**.

Guillopé, M. & Poirier, J. P. 1979. Dynamic recrystallization during creep of single-crystal halite: an experimental study. *Journal of Geophysical Research* **84**, 5557-5567.

Hildyard, R. C., Prior, D. J., Faulkner, D. R. & Mariani, E. 2009. Microstructural analysis of anhydrite rocks from the Triassic Evaporites, Umbria-Marche Apennines, Central Italy: An insight into deformation mechanisms and possible slip systems. *Journal Of Structural Geology* **31**(1), 92-103.

Jiang, J., Britton, T. B. & Wilkinson, A. J. 2013. Measurement of geometrically necessary dislocation density with high resolution electron backscatter diffraction: Effects of detector binning and step size. *Ultramicroscopy* **125**, 1-9.

Kalácska, S., Dankházi, Z., Zilahi, G., Maeder, X., Michler, J., Ispánovity, P. D. & Groma, I. 2020. Investigation of geometrically necessary dislocation structures in compressed Cu micropillars by 3-dimensional HR-EBSD. *Materials Science and Engineering: A* **770**, 138499.

Kendrick, J. E., Lavallee, Y., Mariani, E., Dingwell, D. B., Wheeler, J. & Varley, N. R. 2017. Crystal plasticity as a strain marker of the viscous-brittle transition in magmas. *Nature Communications* **8**(1), Art. No. 1926.

Konijnenberg, P. J., Zaefferer, S. & Raabe, D. 2015. Assessment of geometrically necessary dislocation levels derived by 3D EBSD. *Acta Materialia* **99**, 402-414.

Kovaleva, E., Klotzli, U., Habler, G. & Wheeler, J. 2015. Planar microstructures in zircon from paleo-seismic zones. *American Mineralogist*.

Kovaleva, E., Klotzli, U., Wheeler, J. & Habler, G. 2018. Mechanisms of strain accommodation in plastically-deformed zircon under simple shear deformation conditions during amphibolite-facies metamorphism. *Journal Of Structural Geology* **107**, 12-24.

Kuhr, B. & Farkas, D. 2019. Dislocation content in random high angle grain boundaries. *Modelling and Simulation in Materials Science and Engineering* **27**(4), 045005.

Lloyd, G. E. 2002. Microstructural evolution in a mylonitic quartz simple shear zone: the significant roles of dauphine twinning and misorientation. In: *Joint International Meeting of the Tectonic-Studies-Group of the Geological-Society London/Structural Geology and Tectonics Division of the Geological-Society-of-America/Geological-Society-of-Australia*. *Geological Society Special Publication* **224**, London, ENGLAND, 39-61.

MacDonald, J. M., Wheeler, J., Harley, S. L., Mariani, E., Goodenough, K. M., Crowley, Q. G. & Tatham, D. 2013. Lattice distortion in a zircon population and its effects on trace element mobility and U–Th–Pb isotope systematics: examples from the Lewisian Gneiss Complex, northwest Scotland. *Contributions To Mineralogy And Petrology* **166**, 21-41.

Mamtani, M. A., Reznik, B. & Kontny, A. 2020. Intracrystalline deformation and nanotectonic processes in magnetite from a naturally deformed rock. *Journal of Structural Geology* **135**, 104045.

Marquardt, K. & Faul, U. H. 2018. The structure and composition of olivine grain boundaries: 40 years of studies, status and current developments. *Physics and Chemistry of Minerals* **45**(2), 139-172.

Mcnamara, D. D., Lister, A., Prior, D. J., Scully, A., Gardner, J. & Wheeler, J. 2020. Microanalysis of Calcite Scaling in a Fractured Geothermal System.

Nicolay, A., Franchet, J. M., Cormier, J., Mansour, H., De Graef, M., Seret, A. & Bozzolo, N. 2019. Discrimination of dynamically and post-dynamically recrystallized grains based on EBSD data: application to Inconel 718. *JOURNAL OF MICROSCOPY* **273**(2), 135-147.

Nye, J. F. 1953. Some geometrical relations in dislocated crystals. *Acta Metallurgica* **1**, 153-162.

Pantleon, W. 2008. Resolving the geometrically necessary dislocation content by conventional electron backscattering diffraction. *Scripta Materialia* **58**(11), 994-997.

Piazolo, S., Montagnat, M., Grennerat, F., Moulinec, H. & Wheeler, J. 2015. Effect of local stress heterogeneities on dislocation fields: Examples from transient creep in polycrystalline ice. *Acta Materialia* **90**, 303-309.

Poirier, J. P. & Nicolas, A. 1975. Deformation-induced recrystallization due to progressive misorientation of subgrains, with special reference to mantle peridotites. *Journal of Geology* **83**, 707-720.

Prior, D. J. 1999. Problems in determining the orientations of crystal misorientation axes, for small angular misorientations, using electron backscatter diffraction in the SEM. *Journal of Microscopy* **195**, 217-225.

Prior, D. J., Mariani, E. & Wheeler, J. 2009. EBSD in the Earth Sciences: applications, common practice and challenges. In: *Electron Backscatter Diffraction in Materials Science* (edited by Schwartz, A. J., Kumar, M., Adams, B. L. & Field, D. P.). Springer, 345-357.

Ram, F., Zaefferer, S., Japel, T. & Raabe, D. 2015. Error analysis of the crystal orientations and disorientations obtained by the classical electron backscatter diffraction technique. *Journal of Applied Crystallography* **48**(3), 797-813.

Shigematsu, N., Prior, D. J. & Wheeler, J. 2006. First combined electron backscatter diffraction and transmission electron microscopy study of grain boundary structure of deformed quartzite *Journal of Microscopy* **224**, 306-321.

Spruzeniece, L., Piazolo, S. & Maynard-Casely, H. E. 2017. Deformation-resembling microstructure created by fluid-mediated dissolution-precipitation reactions. *Nature Communications* **8**.

Sutton, A. P. & Balluffi, R. W. 1995. *Interfaces in crystalline materials*. Clarendon Press, Oxford.

Tielke, J. A., Mecklenburgh, J., Mariani, E. & Wheeler, J. 2019. The influence of water on the strength of olivine dislocation slip systems. *Journal Of Geophysical Research: Solid Earth* **124**, 6542-6559.

Tielke, J. A., Zimmerman, M. E. & Kohlstedt, D. L. 2017. Hydrolytic weakening in olivine single crystals. *Journal of Geophysical Research-Solid Earth* **122**(5), 3465-3479.

Timms, N. E., Pearce, M. A., Erickson, T. M., Cavosie, A. J., Rae, A., Wheeler, J., Wittman, A., Ferriere, F., Poelchau, M. H., Tomioka, N., Collins, G. S., Gulick, S. P. S., Rasmussen, C., Morgan, J. V. & Scientists, I.-I. E. 2019. New shock microstructures in titanite (CaTiSiO5) from the peak ring of the Chicxulub impact structure, Mexico. *Contributions To Mineralogy And Petrology*.

Timms, N. E., Reddy, S. M., Healy, D., Nemchin, A. A., Grange, M. L., Pidgeon, R. T. & Hart, R. 2012. Resolution of impact-related microstructures in lunar zircon: A shock-deformation mechanism map. *Meteoritics & Planetary Science* **47**(1), 120-141.

Trimby, P. W., Cao, Y., Chen, Z., Han, S., Hemker, K. J., Lian, J., Liao, X., Rottmann, P., Samudrala, S., Sun, J., Wang, J. T., Wheeler, J. & Cairney, J. M. 2014. Characterizing deformed ultrafine-grained and nanocrystalline materials using transmission Kikuchi diffraction in a scanning electron microscope. *Acta Materialia* **62**, 69-80.

Trimby, P. W., Prior, D. J. & Wheeler, J. 1998. Grain boundary hierarchy development in a quartz mylonite. *Journal of Structural Geology* **20**, 917-935.

Wallis, D., Hansen, L. N., Ben Britton, T. & Wilkinson, A. J. 2016. Geometrically necessary dislocation densities in olivine obtained using high-angular resolution electron backscatter diffraction. *Ultramicroscopy* **168**, 34-45.

Wallis, D., Hansen, L. N., Britton, T. B. & Wilkinson, A. J. 2019a. High-Angular Resolution Electron Backscatter Diffraction as a New Tool for Mapping Lattice Distortion in Geological Minerals. *Journal of Geophysical Research: Solid Earth* **124**, 6337–6358.

Wallis, D., Parsons, A. J. & Hansen, L. N. 2019b. Quantifying geometrically necessary dislocations in quartz using HR-EBSD: Application to chessboard subgrain boundaries. *Journal of Structural Geology* **125**, 235-247.

Weikusat, I., Miyamoto, A., Faria, S. H., Kipfstuhl, S., Azuma, N. & Hondoh, T. 2011. Subgrain boundaries in Antarctic ice quantified by X-ray Laue diffraction. *Journal of Glaciology* **57**(201), 111-120.

Wheeler, J., Mariani, E., Piazolo, S., Prior, D. J., Trimby, P. & Drury, M. R. 2009. The weighted Burgers vector: a new quantity for constraining dislocation densities and types using Electron Backscatter Diffraction on 2D sections through crystalline materials. *Journal of Microscopy* **233**(3), 482-494.

White, S. 1976. The effects of strain on the microstructures, fabrics, and deformation mechanisms in quartzites. *Philosophical Transactions of the Royal Society of London A* **283**, 69-86.

Wieser, P., Edmonds, M., Maclennan, J. & Wheeler, J. 2020. The Record of Magma Storage under Kīlauea Volcano preserved in Distorted Olivine Crystals. *Nature Communications*.

Wilkinson, A. J. & Randman, D. 2010. Determination of elastic strain fields and geometrically necessary dislocation distributions near nanoindents using electron back scatter diffraction. *Philosophical Magazine* **90**(9), 1159-1177.

Winkelmann, A., Nolze, G., Cios, G., Tokarski, T. & Bała, P. 2020. Refined Calibration Model for Improving the Orientation Precision of Electron Backscatter Diffraction Maps. *Materials* **13**(12), 2816.

Wirth, R. 1996. Thin amorphous films (1–2 nm) at olivine grain boundaries in mantle xenoliths from San Carlos, Arizona. *Contributions to Mineralogy and Petrology* **124**(1), 44-54.

Zhang, Z., Ódor, É., Farkas, D., Jóni, B., Ribárik, G., Tichy, G., Nandam, S.-H., Ivanisenko, J., Preuss, M. & Ungár, T. 2020. Dislocations in Grain Boundary Regions: The Origin of Heterogeneous Microstrains in Nanocrystalline Materials. *Metallurgical and Materials Transactions A* **51**(1), 513-530.

# For submission to Journal of Structural Geology

**Using crystal-lattice distortion data for geological investigations: the weighted Burgers vector method**

J. Wheeler[1], S. Piazolo[2], D. J. Prior[3], P. W. Trimby[4] and J. A. Tielke[5]

[1]Department of Earth, Ocean, and Ecological Sciences, University of Liverpool, 4 Brownlow Street, Liverpool, L69 3GP, UK

[2] University of Leeds, School of Earth & Environment, Leeds LS2 9JT, UK

[3]Department of Geology, University of Otago, Dunedin, New Zealand

[4]Oxford Instruments Nanoanalysis, High Wycombe, Bucks, England

[5]Lamont-Doherty Earth Observatory of Columbia University, Palisades, NY, USA

**Abstract**

Distorted crystals carry useful information on processes involved in their formation, deformation and growth. The distortions are accommodated by geometrically necessary dislocations, and therefore characterising those dislocations is an informative task, to assist in, for example, deducing the slip systems that produced the dislocations. Electron backscatter diffraction (EBSD) allows detailed quantification of distorted crystals and we summarise here a method for extracting information on dislocations from such data. The weighted Burgers vector (WBV) method calculates a vector at each point on an EBSD map, or an average over a region. The vector is a weighted average of the Burgers vectors of dislocation lines intersecting the map surface. It is weighted towards dislocation lines at a high angle to the map but that can be accounted for in interpretation. The method is fast and does not involve specific assumptions about dislocation types; it assumes only that elastic strains have little effect on the calculation. It can be used, with care, to analyse subgrain walls (sharp orientation changes) as well as gradational orientation changes within individual grains. There are four linked parts to this contribution.

1. We describe the mathematical background to the WBV and then how it is modified to deal with spaced, discrete orientation measurements.
2. EBSD orientation data have angular errors, and so does the WBV. We present a new analysis of these angular errors, showing there is a trade-off between directional accuracy and area sampled. Angular errors can now be accounted for during testing of hypotheses about dislocation types.
3. We present new studies on olivine and plagioclase to illustrate how to use the method.
4. We discuss published studies on ice and titanite to further illustrate the method.

We note that the methods discussed here are applicable to any crystalline material encompassing minerals (including ice), metals and ceramics.

**Keywords**

Electron Backscatter Diffraction; Geometrically Necessary Dislocations; Slip Systems; Intracrystalline Distortion; weighted Burgers vector; Olivine; Plagioclase; Ice; Titanite

## 1. Introduction

Microstructures are crucial indicators of processes that have affected rocks. Dislocations provide evidence for how and under what conditions individual grains have deformed or they may be growth defects indicating growth conditions. Regardless of their origin dislocations give rise to *distortion* in a crystal lattice on some scale, and we advocate use of this word as a non-genetic description of their geometric effects. If dislocations are due to deformation their Burgers vectors may help constrain the style or conditions of deformation. Individual dislocations give a lattice extra energy, so the density of dislocations is needed to estimate this on a volumetric basis. This plastic strain energy provides a driving force for recrystallization in deformed rocks (Drury & Urai 1990). TEM is the standard method to image individual dislocations, a procedure that can be laborious and will characterise just a tiny fraction of the microstructure, leaving doubts as to how representative it is. In contrast intracrystalline distortions may be optically visible and can be quickly characterised by EBSD mapping over large regions. Such distortions, regardless of cause, must be accommodated by geometrically necessary dislocations (GNDs) (Ashby 1970) and hence give indirect information on dislocation content.

The GND concept complements the statistically stored dislocation (SSD) concept. The dislocations involved are not fundamentally different types; instead, these are scale dependent ideas. Lattice curvature over a particular length scale is by definition accommodated by GNDs *at that scale.* Over that length scale there may be other dislocations for example of opposite signs, that cancel out each other's local curvature effects (though still contribute to plastic strain energy and other relevant properties): these are SSDs. Zooming in to a smaller length scale may reveal local lattice curvatures related to what were classified as SSDs. At this smaller length scale some SSDs are now GNDs. If one examines lattice curvature on the atomic scale, all dislocations would be classified as GNDs. In relation to EBSD, the relevant length scale is the step size. So lattice curvature shown on EBSD maps relates to GNDs on the scale of the step size. SSDs will, by definition, not leave a fingerprint on the curvature. A smaller step size will reveal more GNDs. Very small step sizes can reveal individual dislocations (https://www.ebsd.com/ois-ebsd-system/dislocation-density-analysis).

It would be useful to constrain *directional* (lines, Burgers vectors) and *magnitude* (dislocation density) GND information from EBSD data: examples of approaches follow. If distortion is due to deformation by dislocation motion it can in principle be used to constrain active slip systems (hence deformation conditions) using directional information. Based on geometric assumptions alone, such studies have often focussed on subgrain walls (in essence, localised sharp distortions). For example Lloyd (2002) argues that subgrain walls traces and misorientation axes in quartz can be used to deduce slip systems, though assumptions about "pure" tilt or twist nature of boundaries are needed. Wieser et al. (2020) applied a modified approach to olivine, incorporating subgrain wall traces with information from the method of Wheeler et al. (2009). The latter, the weighted Burgers vector (WBV) method, is what we discuss in this contribution. In minerals with multiple slip systems, distortion cannot be uniquely linked to slip systems using geometry alone. Calculations can then be made assuming that the net dislocation energy is minimised with respect to all possible combinations of dislocation lines and Burgers vectors for example in quartz (Wallis et al. 2019b). Distortion magnitudes can be quantified using for example "local misorientation" though the link to actual dislocation densities is not straightforward to make. For example

Timms et al. (2012) use local misorientation maps to give an overview of the heterogeneous distortion in shocked zircon crystals.

If distortion is due to growth, or is postulated to be, then purely geometric analyses can be applied as they would be to deformed crystals but any extra assumptions must be evaluated with care. Spruzeniece et al. (2017) quantified crystal distortions in KBr-KCl solid solution grown in a stress-free environment: these are due to growth not deformation. Gardner et al. (2021) examined natural distorted albite and showed that some subgrain walls contain dislocations with Burgers vectors with <010> components. There are no known slip systems with such Burgers vectors, so the subgrain walls were diagnosed as growth defects.

The methods in these and many other papers using EBSD to analyse distortions include various assumptions, both in manual processes (e.g. selecting straight segments of boundary traces) and in automatic calculations (e.g. assumptions about allowed slip systems and dislocation energy minimisation). It is generally not clear how errors in EBSD orientation measurements affect deductions: specifically, here we address *angular* errors although *magnitude* errors are relevant (e.g. Jiang et al. (2013)~~Jiang~~). Some methods are slow if they are manual or compute intensive, a relevant consideration in terms of time versus benefit. Methods using boundary trace analysis cannot be applied to smooth, distributed distortions because there are no discrete boundaries. Overall, the methods to date have diverse strengths and weaknesses.

Formatted: Not Highlight

Our overall aim here is to review and extend the WBV method for extracting information on GNDs from EBSD data, based on our experience of how it has been used since first publication in 2009. By clarifying and enhancing the insights it can give we hope to encourage its use in future studies. ~~In this contribution we summarise the WBV method for extracting information on GNDs from EBSD data.~~ There are four linked aims.

1. A description of the theoretical basis based on existing understanding (sections 2.1-2.3) but using new illustrative models. We explain the method using model distorted crystals, with mathematical details in Supplementary Information. We discuss how the method applies to smoothly curved lattices and to subgrain walls (where GNDs are collected into surfaces of negligible width). The aim here is to ensure users of the method understand its advantages and limitations.
2. New analysis of the errors (specifically angular errors) inherent in the calculation, so that hypotheses about microstructural evolution can be tested robustly (section 2.4).
3. New examples of application of the method (sections 3.1 olivine and 3.2 plagioclase) to assist in understanding how it works in practice.
4. Review of implications for previous studies in section 3.5 (Table 1), with some detail in 3.3 ice and 3.4 titanite.

Finally, we discuss this method in relation to others used to analyse intracrystalline distortion and suggest future developments. We note that the methods discussed here are applicable to any crystalline material encompassing minerals (including ice), metals and ceramics.

## 2. The WBV method: background and error analysis

The method gives information on combinations of GND Burgers vectors and GND densities, so we now discuss these two concepts. Imagine a closed loop joining atoms (or unit cells) around a dislocation in "sample coordinates" (Fig. 1a, c). ~~in "sample coordinates").~~ Now

move the atoms to the positions they would have in an undistorted crystal: the Burgers vector is the gap opened up in the previously closed loop (red arrows in Fig. 1b, d) in "crystal coordinates"). It can be described in crystal coordinates (hence dimensionless, for example [100] for the edge and [001] for the screw) or in sample coordinates (dimensions of length; direction depends on sample orientation). Dislocation density is a phrase that is used in different ways. It may refer to the total line length of SSDs in a unit volume. Not all of these give rise to lattice curvature so here we consider only the total line length of GNDs per unit volume. We illustrate the basic ideas using a 2D model first.

Fig. 1. a) A closed loop around an edge dislocation in sample space, view down along the dislocation line. b) The same path traced out in crystal coordinates, showing a gap that is the definition of the Burgers vector (red) of the dislocation within the loop. c), d) The same for a screw dislocation; the dislocation line is parallel to the Burgers vector.

*2.1. Concepts in 2D*

GND density relates to lattice curvature and a 2D description illustrates this most simply, where there is no distortion in the z or [001] direction. We show here how curvature relates to single then multiple dislocation populations. Figure 2 shows lattice orientations in a 2D model which can, at each point, be described by a single number (angle θ of a particular lattice direction anticlockwise from a reference direction). In 2D all dislocations have edge character and in the Figure the Burgers vectors are defined as one atomic spacing so **b** = [100]. The four frames show increasing dislocation density ρ, defined in 2D as the number of dislocations per unit area, and the corresponding increase in lattice curvature. The irregular spacing of dislocations means this model is an approximate illustration but provides a basis for understanding.

Figure **2.** Visualization of the link between GND density (chosen here as edge dislocations all the same sign) and lattice curvature. The crystallographic "z" direction [001] is chosen as out of the page so the dislocations illustrated have line vector [001] and Burgers vector [100]. Angle θ, dependent on position, shows orientation of a lattice direction relative to a reference direction (thick line).

EBSD measurements do not pick out individual atoms but provide orientation θ as a defined function of position (in 2D, θ(x, y)); that is what we must work with. Lattice curvature is defined by variations in θ in the x and/or y directions. The lattice curvature is then a vector

$$\boldsymbol{\kappa} = -\left(\frac{\partial\theta}{\partial x}, \frac{\partial\theta}{\partial y}\right) \quad (1)$$

(see Appendix 2.1 for details). There is one key assumption made when using the WBV method: that elastic strains have a relatively small effect. If EBSD records lattice curvature, then that could in principle be caused by elastic strain. As EBSD cannot generally image individual dislocations, an EBSD map of (for example) Fig. 2 could look identical to a map of a perfect lattice with no GNDs, elastically bent. However, as was argued in Wheeler et al.

(2009), in the microstructures we have studied, curvature is often localized along sub-grain walls and we cannot conceive of elastic strain being localized in this way. Secondly, we would expect elastic bending in a wide variety of orientations in a polycrystal, giving rise to a wide variety of (illusory) WBVs. Instead, we see systematic patterns as exhibited in the case studies we present here, and in most of the published studies (Table 1). Wallis et al. (2019a) find that "often the rotation gradients are larger than the elastic strain gradients … in which case, the elastic strain gradients can be neglected".

From now on we will assume no elastic strains and, in that case, $\boldsymbol{\kappa}$ relates to a single population of GNDs by

$$\boldsymbol{\kappa} = \rho \boldsymbol{b}$$

that incorporates the fact that in sample coordinates, **b** may vary even if it is a single crystallographic direction. Considering just the magnitudes, we can write this as

(curvature) = (dislocation density) × (Burgers vector length)

which is a starting point for understanding the link between curvature and dislocation density. If there is more than one type of dislocation (each with different Burgers vectors and densities)

$$\boldsymbol{\kappa} = \sum_N \rho^{(N)} \boldsymbol{b}^{(N)} \qquad (2)$$

where ρ and **b** are the density and Burgers vectors *for each type* (superscript N) of dislocation. If there were just 2 types of dislocation, this equation would yield their densities uniquely. If more than 2 types are present then the densities are non-unique, but the equation still provides constraints. Such issues are relevant for 3D which we now discuss.

*2.2. Concepts in 3D*

In 3D we require three numbers to define a lattice orientation (e.g. conventionally three Euler angles, although other representations are available), and we have three directions in which to evaluate gradients, there are 9 gradients to consider. Nye (1953) showed how curvature is then a second rank tensor, but a more direct link to dislocation density (line length per unit volume in 3D) is established via a tensor $\boldsymbol{\alpha}$ (which now carries his name), also a function of orientation gradients. This links to dislocation density as follows.

$$\alpha_{i\gamma} = \sum_N \rho^{(N)} b_i^{(N)} l_\gamma^{(N)} \qquad (3)$$

where ρ, **b** and **l** are the density, Burgers vector and unit line vector for each type (labelled N) of dislocation. Note the close resemblance to eqn 2, but with the extension to include dislocation line vectors. When there are many types of dislocation, there may be multiple combinations giving a particular Nye tensor. Note the following.

- This has to be written in terms of vectors and tensors, since the situation is 3D.
- Such equations are best written using index notation which makes explicit whether vectors are expressed in crystal coordinates (Latin subscript for $b_i$) or sample coordinates (Greek subscript for $l_\gamma$), for reasons explained in Wheeler et al. (2009) and Das et al. (2018).

- $\alpha$ is sometimes called "dislocation density" but must be distinguished from other uses of the same phrase.

Determining the full Nye tensor requires orientation gradients in all three directions. Although there are GND studies using 3D EBSD from serial focussed ion beam milling e.g. (Kalácska et al. 2020, Konijnenberg et al. 2015) these are challenging and generally EBSD is conducted on 2D sections. Wheeler et al. (2009) showed that relevant (though incomplete) information could still be extracted from a 2D map. Specifically, of the 9 components of the Nye tensor, a 3-component vector can be calculated. The vector is a sum of Burgers vectors of GNDs, *weighted* by the actual dislocation density of each type of GND and by the angle between the dislocation lines and the map. Lines at a high angle to the map are favoured because the mathematics involves multiplying the true density by sin(angle between dislocation line and map). The phrase "weighted Burgers vector" (WBV) was used, to make clear that this vector is a weighted "sample" of the Nye tensor.

$$W_i = \alpha_{i3} = \sum_N \rho^{(N)} b_i^{(N)} l_3^{(N)} = \sum_N \left[\rho^{(N)} l_3^{(N)}\right] b_i^{(N)} \qquad (4)$$

where W is the WBV, and the subscript "3" refers to the z direction, perpendicular to the map, so $l_3$ is the component of a dislocation line vector perpendicular to the map: it varies from 0 (lines parallel to map) to 1 (lines perpendicular to map). The terms in square brackets are scalars, so note that the WBV is a linear combination of Burgers vectors – this is one reason~~s~~ why it is a useful quantity. The WBV has units of (length)$^{-1}$ and we recommend using the convenient ~~it is convenient to use~~ unit~~s~~ of (μm)$^{-1}$. We denote its magnitude as W. It can be expressed in crystal coordinates as in eqn (4), or in sample coordinates by calculating **hW** where **h** is the orientation tensor (a function of Euler angles). It might appear that this will give a non-unique answer for the vector in sample coordinates, since **W** has symmetric variants in crystal coordinates, but Appendix 1 shows this is not the case – there is a unique WBV in sample coordinates.

There are two approaches to calculating **W**, differential and integral. The differential method involves evaluating local gradients in **h** around the point at which **W** is required. Since that point has a specific orientation, **W** can be expressed in crystal or sample coordinates. The integral method involves integrating round a closed loop on the map to obtain the *net* or *average* Burgers vector content of the GND lines intersecting the map inside the loop, expressed in crystal coordinates. The mathematics in essence defines the loop in sample coordinates (c.f. Fig. 1a) black arrows), transforms each loop segment (black arrow) into crystal coordinates (c.f. Fig. 1b) black arrows), and sums up the segments in crystal coordinates to give the net Burgers vector (red arrow). ~~Unlike the differential method, there is no strict way to express the vector in sample coordinates because orientation varies around and within the loop and the result of the integral method is not linked to any particular point within the loop. However, as we discuss below, f~~For the calculation to be meaningful there should be no "high angle" grain boundaries (HAGBs) (which do not usually have organised dislocation substructures~~large~~) ~~orientation variations around~~ intersected by the loop. If the loop crosses HAGBs then the calculation will still return a vector, but that will not give clear information on dislocations. There is no systematic knowledge of or agreement on what constitutes an HAGB and we usually pick 5 degrees as a maximum angle~~: see~~, discussed further in section 2.2.5. ~~In that case the orientation at, for example, the loop centroid could be~~

~~used to convert from crystal to sample coordinates. If orientation variations include "high angle" grain boundaries (HAGBs) which do not have organised dislocation substructures then the calculation will still return a vector but it will not give information on dislocations.~~ Unlike the differential method, there is no strict way to express the vector in sample coordinates because orientation varies around and within the loop and the result of the integral method is not linked to any specific point within the loop. ~~In~~However, if the loop does not include HAGBs then orientation variations in the loop are small ~~that case~~and the orientation at, for example, the loop centroid could be used to convert from crystal to sample coordinates. ~~There is no systematic knowledge of or agreement on what constitutes an HAGB and we usually pick 5 degrees as a maximum angle: see section 2.2.5.~~

If the orientation **h** is a defined mathematical function of position, then the methods are identical (they are related by Stokes' theorem). In practice **h** is defined at discrete measurement points, e.g. on a square grid. The differential method then involves numerical estimation of orientation gradients, with some flexibility in terms of the number of points used. The integral method involves numerical integration around the closed loop. As we will show later (section 2.3), the methods have different advantages in practice.

*2.2.1. WBV, lattice vectors and Burgers vectors*

In this section we discuss the links between WBV and Burgers vectors and show how there may be unique or non-unique relationships. In the approach we describe here, the "differential" values of WBV are usually expressed in units of $(\mu m)^{-1}$. In crystal coordinates **W** can be decomposed into lattice basis vectors **L** if needed

$$\boldsymbol{W} = K_1\boldsymbol{L}_1 + K_2\boldsymbol{L}_2 + K_3\boldsymbol{L}_3 \quad (5)$$

where the coefficients K are in units of $(\text{length})^{-2}$. These coefficients *resemble* dislocation densities but are in general different. This decomposition relates to the GND types and densities and is unique but further assumptions are needed to express it in terms of the Burgers vectors of actual slip systems. For example, in olivine, slips systems have Burgers vectors that are either [100] or [001]. If we find that **W** is parallel to [203] and we know the distortion is due to crystal plasticity then we can deduce that it shows a combination of slip systems with [100] and [001] Burgers vectors. The magnitude of **W** parallel to [100] would then, in accord with eqn. (4), be a weighted sum of the dislocation densities of all types of dislocation with [100] Burgers vectors. In anhydrite, also orthorhombic, slip systems can involve [001], [1-1-2] and [11-2] Burgers vectors (Hildyard et al. 2009). There is a unique way to express the three components of **W** in terms of those three vectors, if those vectors are linearly independent: in this example [203] = 7[001] + [1-1-2] + [11-2]. However, many crystals have more than three Burgers vectors for possible slip systems, especially in more symmetric crystals counting all symmetric variants. For example, in a trigonal phase such as calcite, there will be at least 3 Burgers vectors in the basal plane. Any two of these can be combined to give the basal plane component of **W**, so the decomposition is non-unique. **W** still carries valuable information on the relative contributions of dislocations with basal and non-basal Burgers vectors (Chauve et al. 2017). Our philosophy here is that the methods give the value of **W**, and if further assumptions are required (in terms of expected slip systems, relative energies etc.) these should be made on a case-by-case basis. The K coefficients can be related to GND densities using further information such as the specific Burgers vectors of GNDs.

Except for angular errors which are discussed later, it is crucial to note that the WBV cannot generate "phantom" directions: it must be the weighted average of Burgers vectors that are actually present in the microstructure. For example, regardless of mineral symmetry, if **W** is [203] then *at least one* of the GND types involved *must* have Burgers vector with an [001] component, though not necessarily parallel to [001]. Similarly, *at least one* of the GND types involved *must* have Burgers vector with an [100] component. **W** could be decomposed as 2[100] + 3[001], or 2[101] + 1[001], or 3[101] – 1[001] or even simply 1[203] if [203] is a known Burgers vector. ~~In a later section~~

We next illustrate how to visualise and interpret the WBV, using models for a smoothly tilted lattice and a smoothly twisted lattice (for illustration, distortions are much larger than those found in real crystals). We then address a tilt subgrain wall, describing some issues that are specific to sharp changes in orientation. The models have no variation of orientation in the z direction and the Nye tensors can be calculated fully (Appendix 2).

Figure **3.** Basic WBV concepts illustrated with model tilted and twisted crystals. a), b) 3D views of model tilted and twisted crystals, planes are colour coded in accord with IPF key (inset) for plane normal. Pale yellow of semi-transparent rectangles indicates the map plane though not the shape, with x and y marked for subsequent maps. c), d) Misorientation relative to top-left corner for tilt and twist models. In c) misorientation is around the [001] axis that points out of the page. In d) misorientation is around the [010] axis, running left-right, with linearly increasing gradient of twist angle to right. e), f) WBV magnitude (in $\mu m^{-1}$) colour coded for each model. In e) actual vector directions shown as white arrows; in f) WBV directions point directly into page so are not shown. The boxes are example integration loops with the net WBV indicated as K coefficients in $(\mu m)^{-2}$. g), h) WBV direction colour coded for each model. i) 3D view of semi-transparent WBV magnitude map for tilt model (as in (e)), with edge dislocations lines shown schematically: parallel to [010] and colour coded in accord with their [100] Burgers vectors. j) 3D view of semi-transparent WBV direction map for twist model (as in (h)), with two sets of screw dislocations lines shown schematically: blue parallel to [100], red parallel to [001]. For visual clarity the dislocations are shown as if in walls, but the distortion gradient is smooth. Note how the "weighting" towards dislocation lines perpendicular to the map causes variation in WBV direction (as in f) although the relative density of the two types of dislocation is uniform in 3D.

*2.2.2. Smoothly tilted crystal*

This model is similar to Fig 2, with a 3D view shown in Fig. 3a). The lattice is misoriented relative to the y-axis by an angle θ (zero along the y-axis and < 0 to the right), Fig. 3c). The misorientation axis is [001] that points out of the page. The centre of curvature is beyond the bottom left of the map (Fig. 3c)). If r is the distance to this centre, it is the radius of curvature of the lattice and in sample coordinates

$$\boldsymbol{W} = \frac{1}{r}(\cos\theta\,, \sin\theta\,, 0)$$

and in crystal coordinates,

$$\boldsymbol{W} = \frac{1}{r}(1,0,0) \qquad (6)$$

The magnitude of W is shown in Fig. 3e), increasing towards the centre of curvature in accord with eqn. (6). The WBV is a vector that can be represented in sample or crystal space: these require different methods for visualising direction. In sample space WBVs can be displayed as arrows on a map as in Fig. 3e). The direction in crystal coordinates is colour coded (as in any other sort of IPF map) in Fig. 3g), with the IPF colour scheme inset. Since **W** is everywhere parallel to [100] we see a single colour. The rectangle is an integral loop labelled with its net Burgers vector content in units of $(\mu m)^{-2}$; note only the first [100] component is non-zero.

Multiple decompositions of **W** are possible, but the simplest is a single population of edge dislocations with lines parallel to [001], Burgers vectors parallel to [100] and density

$$\frac{1}{ar}$$

where a is the length of [100]. Fig. 3i) shows a 3D view of that model. If this were not a model, all the map and WBV data could be in accord with other interpretations, for example dislocation lines not parallel to z. However, *any* interpretation must involve dislocations with Burgers vectors with a [100] component: the WBV calculation cannot generate "phantom" components (see above).

*2.2.3. Smoothly twisted crystal*

This model illustrates the importance of understanding the "weighting" or stereological bias in the WBV calculation. In Fig. 3b) the twist is defined by misorientation by angle θ around the [010] axis, with $\frac{d\theta}{dx}$ increasing to the right. Fig. 3d) shows the misorientation, defined as the *minimum* angle (with no absolute sign) required to rotate a lattice back to a reference orientation, relative to the top-left corner. Because this is olivine, symmetry dictates that the misorientation reaches a maximum at 90 degrees then decreases rightwards even though the lattice is more twisted to the right and the angle θ used for calculations increases monotonically. In sample coordinates (appendix 2.2) we have

$$\boldsymbol{W} = \frac{d\theta}{dx}(0,0,-1)$$

In crystal coordinates

$$\boldsymbol{W} = \frac{d\theta}{dx}(\sin\theta\,, 0, -\cos\theta)\,. \qquad (7)$$

The magnitude of W is simply $\frac{d\theta}{dx}$ and increases linearly to the right because θ is quadratic in x (Fig. 3f)). WBV arrows in sample coordinates are not shown for the twist example because they all point vertically out of the map. Despite the fact that individual dislocation lines and Burgers vectors are clearly not vertical, the WBV components parallel to the map cancel out because we are adding weighted contributions. In crystal coordinates the direction of **W** varies sinusoidally with θ (Fig. 3h)). The rectangle is an integral loop labelled with its net Burgers vector content in units of $(\mu m)^{-2}$; note both [100] and [001] components are non-zero, in agreement with the presence of blues and purples within the loop. The variation in

WBV direction across the map could be interpreted to mean that different types of dislocation predominate in different parts of the model. This is not the case: it is a stereological effect and needs careful explanation now because such effects must be borne in mind in any study.

Multiple decompositions of **W** are possible, but the simplest is as a sum of contributions from screw dislocations parallel to [100] with a density of

$$\frac{1}{a}\frac{d\theta}{dx}$$

and screw dislocations parallel to [001] with a density of

$$\frac{1}{c}\frac{d\theta}{dx}.$$

This decomposition is show in Fig. 3j). The screw dislocation lines are coloured using the IPF colour scheme for screw dislocation *line direction* (as in Fig. 3g)) but since these are screw dislocations the colours also indicate Burgers vector directions. Consider the model near the left hand end where θ is small. Blue dislocations, with [100] line vectors, are almost parallel to the map. This means the WBV calculation does not "sample" them and the IPF colour (Fig. 3h)) is dominated by red [001]. As the lattice is more twisted passing to the right, [100] lines are at higher and higher angles to the map. Hence the WBV IPF map is more dominated by blue. At a position near the right-hand side of the map, [001] lines are parallel to the maps so are not sampled at all; the IPF map is blue. As θ increases beyond 90 degrees we see an influence of [001] reappear. This is an example of the "weighting" towards dislocation lines at a high angle to the map.

The twist structure illuminates some fundamental aspects of WBV. The displays are entirely in accord with eqn. (7) and the WBV provides a weighted "subset" of the full dislocation population. If we were to examine another map at right angles to the one considered (but still containing the twist rotation axis) this second map would show a preponderance of [100] vectors at the left end, with more [001] passing to the right – it would look quite different.

*2.2.4. Model of subgrain tilt wall*

Many microstructures contain subgrain walls that, although populated by GNDs, have in essence zero width and hence zero volume. This means that dislocation density, defined as line length per unit volume, is infinite. Similarly, a sharp change in orientation means the lattice curvature is infinite. So, although eqn. (4) still applies, it is not particularly helpful. In contrast the integral method is helpful because it still yields finite values when the loop crosses a subgrain wall. For any particular subgrain wall the ~~Now, though, the quantities obtained are highly dependent on the size of the loop chosen for integration: the area does not affect the~~ net Burgers vector content **B**~~,~~ depends only the length of subgrain wall intersected by the loop, and not on the loop area.~~.~~ In this paper we use a vector **B**/A with units of (length)$^{-1}$ to characterise the GND content of any loop. For a subgrain wall, then, the magnitude of **B**/A is strongly influenced by loop area. Fig. 4 shows three loops, each intersecting the same length of subgrain wall and having the same value of **B**. ~~However, t~~The areas differ and so the ~~values~~ magnitudes of **B**/A ~~differ~~differ; however, the *direction* of **B**/A is not influenced by A and carries useful GND information. The advantage of the integral method for analysing subgrain walls persists when we consider spaced measurement points (section 2.3.2).

Fig. 4. Numerical aspects in of subgrain wall analysis - a sharp boundary indicated by green line, misorientation 5.6° around [001], crystal directions shown on either side with exaggerated misorientation for clarity. The 3 white boxes are used as loops to indicate the average dislocation density using the integral method (inset numbers for each box): they have relative lengths 1, 2 and 3.

386

387 So far we have assumed that all the analysed distortions are due to GNDs, but for sufficiently
388 high angle boundaries this will not be the case. We discuss this in detail next.

389 *2.2.5 "High angle" boundaries and boundary dislocation content*
390
391 When can boundaries be regarded as made of GNDs? Questions emerge for high angle grain
392 boundaries (HAGBs) where basic geometry proves that dislocations with specific Burgers
393 vectors must be close together and may not be recognisable as discrete entities. White (1976)
394 states "The limit is reached when dislocations are so closely spaced that they lose their
395 individual identity and when this happens the boundary is no longer a low angle sub-grain
396 boundary but a high angle, mobile, grain boundary. If a spacing of 2.5 nm (five lattice
397 spacings) is taken as the minimum distance before core interference … then a low angle
398 boundary becomes a grain boundary when the misorientation is about 10°". Trimby et al.
399 (1998) state "Without detailed TEM [Transmission Electron Microscopy] studies the nature
400 of a boundary can only be constrained from the nature of the misorientation across it": here
401 "constrained" does not mean "fully described". They continue "In many studies an arbitrary
402 misorientation value is assigned, above which boundaries are assumed to be grain boundaries
403 and below which they are assumed to be subgrain walls although, in some cases (e.g. quartz),
404 this value corresponds to the necessary misorientation for the overlap of dislocation cores.
405 Typical values are 10° for quartz (White 1976), 15° or more for halite (Guillopé & Poirier
406 1979) and 15° for olivine (Poirier & Nicolas 1975)". Two decades later there is still a lack of
407 clarity regarding such angles, but we discuss some relevant work next.
408
409 Shigematsu et al. (2006) coupled TEM to EBSD and showed that in quartz boundaries
410 dislocation substructures were lost somewhere between 9° and 17°, with one 13.5° boundary
411 still having dislocations (beyond the angular limit of 10° mentioned above). Mamtani et al.
412 (2020) image dislocations near HAGBs in magnetite using TEM as do Zhang et al. (2020) in
413 a Pd-10%Au alloy. So, HAGBs are not always disorganised. Kuhr and Farkas (2019) used
414 molecular dynamics models of an FCC polycrystal and found dislocations present in some
415 HAGBs. Twin boundaries may have dislocations e.g. p 79 of (Sutton & Balluffi 1995) but if
416 the twin plane is perfectly oriented there are none. An attempt to apply the WBV calculation
417 would yield an enormous and illusory dislocation density. Some HAGBs have lattices in
418 direct contact (Marquardt & Faul 2018), others may have amorphous films nm thick (Wirth
419 1996). In summary, HAGBs have diverse characteristics. We cannot address that diversity
420 here; nor can other methods of using EBSD data to deduce dislocation information. We
421 simply assert that our calculation is interpreted assuming that the lattice curvature is due to
422 the presence of GNDs. There is no single "cut-off" HAGB angle beyond which the GND
423 assumption is invalid. For this reason, in the algorithms we have created the user chooses the
424 HAGB angle above which calculations are excluded. The WBV method may in future
425 provide useful information about HAGB structure, but further research is required.
426
427 Our models up to this point are based on algebraic descriptions of distorted lattices (see
428 Appendix 2). We next address the finite number of measurement points that comprise an

actual EBSD map, and their consequences for gradient and WBV calculations (section 2.3). We then explore the errors in orientation and their consequences for those calculations (section 2.4).

*2.3. Numerical aspects of analysing spaced EBSD measurement points*

Orientation data to be analysed are not mathematical functions of position but discrete measurements at scattered measurement points (hereafter, simply "points" for brevity). The calculation methods therefore involve numerical approximations to the gradients and integrals of the underlying theory, and the differential and integral methods have different advantages in practice. The points in the studies we describe are on square grids, but there is no reason why the method should not be extended to hexagonal or other grids.

*2.3.1. Differential method*

The differential method uses gradients in orientation in the x and y map directions to calculate the WBV. A numerical estimation of gradients uses 2 or more orientation measurements and the distances between the points. We call the cluster of points used a "stencil" (Fig. 5a)). Here each measurement point is represented by a square with a side equal to the step size, so a stencil is illustrated as a cluster of squares. For flexibility our software allows for different stencil sizes; the differential method calculates a "best fit" lattice curvature using the orientations at each point in the stencil. Using larger stencils reduces errors in calculation (discussed later), but at the same time "smears out" microstructural details on the scale of the stencil. In published works the P = 9 stencil has usually been used; we discuss the effects of stencil size in the section on accuracy below.

Figure **5.** Stencils, orientation gradients and errors relevant for WBV. a) "Stencils" are arrangements of nearby measurement points (shown here as squares) used for numerical calculation of orientation gradients at the central point (coloured). Shown are example stencils of area 3, 5, 9 and 21. b) Illustration of effects of orientation errors. Blue graph shows a low but uniform orientation gradient (in 1D) with errors imposed. Red lines show the large effects of errors on estimating gradients over a short segment (analogous to using a small stencil). Note the estimate may even have the wrong sign. Orange line shows the improved precision using a longer segment (analogous to using a larger stencil as in a)). Inset illustrates consequent angular error in WBV direction (in 2D). The actual WBV is shown as middle arrow but with error ε (related to the gradient error) so WBV values might fall in the circle. Outer arrows illustrate the range of directions and hence the angular error δ that would arise due to these errors. c) as in b), with the same errors imposed, but for a larger orientation gradient. The errors in slope are the same as in b) but are *proportionately* less. The error ε in WBV is the same as in b) and the size of the error circle is the same for both. However, the angular error δ is smaller in c) because the WBV is longer.

In ~~a previous~~ section 2.2.4 we pointed out that if a subgrain wall is considered as having zero width, it will have infinite dislocation density. Because of this numerical differentiation creates numerical artefacts as it uses spaced measurement points. The algorithm cannot distinguish a sharp orientation change between two points from a smooth orientation gradient between those points. A consequence is that if a subgrain wall is present, the apparent WBV magnitude will be finite and depend on step size, so should be interpreted with care. In

practice we find that narrow "swathes" of high W are common on calculated W maps and are likely to be subgrain walls. In this case the magnitude W must be interpreted with care but the WBV direction still contains information on the Burgers vectors of the GNDs in the subgrain wall. The 3 boxes in Fig. 6 indicate the calculated W values for a sharp orientation boundary, using the differential method using stencils with areas 9, 13 and 21. Note how the dislocation density is smeared out more for larger stencils, and has apparently lower values.

Fig. 6. Numerical aspects in of subgrain wall analysis - a sharp orientation boundary indicated by green line – using the differential method. The 3 black boxes show regions in which W has been calculated using stencils of size 9 (top), 13 and 21. Compare Fig. 4 which uses the integral method on the same boundary.

*2.3.2. Integral method*

The integral method involves integrating the orientation tensor around a closed loop in the map plane, directly giving the net Burgers vector sum for all the dislocation lines threading through that loop. The details of numerical integration are given in Supplementary Information 1.2. Publications to date have restricted loop shapes to rectangles, though there is no fundamental difficulty in implementing other shapes and this has been done in a commercial version of the algorithm in the Oxford Instruments Aztec system. The result of integration is a vector **B** with dimensions of length. We divide this by the loop area A to get a vector in $(\text{length})^{-1}$ which is more easily compared to results of the differential method. Algebraically, the vector **B/**A must equal the average **W** value in the loop (eqn. (6)). Numerically, the "best fit" algorithm used in the differential method means the methods may give slightly different results; for subgrain walls the integral method remains advantageous (c.f. section 2.2.4).

In Wheeler et al. (2009) the integral method was presented as an exploratory tool in which the user drew rectangular loops and the WBV was reported as a lattice vector (e.g. Fig 3e), f)). More recently a method of systematically "tiling" the map with square loops, and applying the integral method to each loop was used in Fig. 8c of Timms et al. (2019). The tiles can be displayed colour coded by standard IPF colour schemes using a W threshold, in the same way as for calculations made with stencils (examples are given later). The tiles can be thought of as large pixels, though not all properties are precisely analogous to those of individual measurement points. In all circumstances, if the loop crosses a high angle boundary, then a WBV can in principle be calculated but as discussed above, has no meaning - so instead the algorithms we use do not return a result and the tile is left uncoloured.

*2.4. Numerical aspects of dealing with orientation measurement errors*

Orientation measurements used may be in error as a result of errors in the Hough transform, up to a degree at most (Prior et al. 2009); for one study on an Si single crystal, was 0.2° (Ram et al. 2015). Improved "real time" approaches to indexing Kikuchi patterns reduce the angular error in orientations to <0.05° (Nicolay et al. 2019). For higher angular resolution methods, e.g. correlating Kikuchi patterns, errors may be as low as ~0.0003 radians (Wallis et al. 2019a). The differential method uses gradients in crystal orientation to calculate WBV. On the grid of measurement points, a gradient is calculated from the misorientations between adjacent measurements. The misorientation angles are likely to be small and so the errors in misorientation axes will be large (Prior 1999) and these errors will propagate into the WBV

calculation. An algebraic analysis would involve error propagation through operations on various orientation tensors and is beyond the scope of this contribution; instead, we use simple arguments followed by some numerical experiments.

*2.4.1. General nature of error effects*

We argue in this section that angular errors in WBV are smaller for long WBVs. Longer WBVs are linked to higher lattice curvatures. Higher lattice curvatures mean the misorientation angles between adjacent pixels are larger, and the misorientation axes will have smaller errors, and the WBV direction will have smaller errors. We illustrate this assuming a typical orientation error of 0.01 radians.

Benchmark curvature (above which calculation will be less error prone) ~ 0.01/(step size)

and in terms of magnitude

$|WBV|$ ~ curvature

which means we should consider a benchmark below which WBV is error-prone as

$|WBV| \sim 0.01/(\text{step size}) = W_t$

This approach is similar to the derivation of eqn. 13 of Wilkinson and Randman (2010) and eqn 2 of Jiang et al. (2013), where a lower limit on detectable dislocation density is given in terms of step size:

(Minimum detectable GND density) ~

(Angular resolution) /((step size) * (Burgers vector length) )

For example 0.01 /( (1 micron) * (5 angstrom) ) = 2 x $10^{13}$ $m^{-2}$

The approach described below is related because in order of magnitude, $W = \rho b$. Hence our $W_t/b$ equates to the minimum detectable GND density discussed in other work. That work, and others (by the group) focusses on accuracy in determining dislocation *density*; here we also analyse WBV *direction* since it plays a key role in several studies (Table 1). In Wheeler et al. (2009) we argued that longer WBVs would be more accurate in terms of direction. For example, the map of Mg used in Fig. 2 and 3 of Wheeler et al. (2009), modified in Fig. 7, has a step size of 4 μm so $W_t = 0.0025$ $\mu m^{-1}$. Fig. 7 shows considerable scatter for $W > 0.002$ $\mu m^{-1}$ and much less for $W > 0.004$ $\mu m^{-1}$, in accordance with the argument that $W_t$ offers a guide to judging precision. Guided by this, our approach to displaying WBV data involves selecting data based on ranges of W. The minimum value $W_{min}$ in the range will be associated with the maximum angular error. Setting it high will reduce error. The maximum value $W_{max}$ is less important but is useful for dividing up datasets.

Figure **7.** IPFs of Mg WBV displayed using three different thresholds: threshold lengths and numbers of points as indicated, modified from Fig. 3 of Wheeler et al. (2009).

Figure 5b) and c) are non-rigorous illustrations of error effects. The graphs illustrate that larger stencils will give better precision. Errors ε in gradients are independent of the gradients themselves but for larger orientation gradients (as in Fig. 5c)), longer WBVs) the errors are

533 *proportionately* less important. The insets in b) and c) illustrate the consequent effects on
534 angular errors. The errors in WBV are now drawn as circles around the actual values since
535 errors may be in any direction. The error circles are the same size in b) and c). The green
536 arrows mark the vectors with maximum angular error δ, showing that longer WBVs in c) will
537 have smaller angular errors. In the next section we analyse error effects using numerical
538 models.

539 *2.4.2. Specific analyses of error effects*
540 It is useful to quantify error estimates for WBV, incorporating the effects of WBV length and
541 other parameters. We define an angle $\alpha_{95}$ so that there is a 95% chance that the true WBV
542 direction is that angle or less from the calculated direction, an approach used in analysing
543 palaeomagnetic data for example Butler (1992). In essence $\alpha_{95}$ defines a cone of directions
544 within which the true direction is likely to be. This is analogous to the $\pm$2 standard deviation
545 range within which 95% of the data lie when dealing with a one-dimensional normal
546 distribution. Our approach gives the angular error for the WBV in sample coordinates: it is in
547 principal the same for crystal coordinates except crystal symmetry may modify the
548 interpretation, as addressed in Appendix 3.1.

549 EBSD orientation errors will depend on mineralogy, acquisition conditions and indexing
550 methods and will propagate in the WBV calculations. For illustration we create model
551 orientation maps with angular errors in orientation up to 0.57° (0.01 rad) – so our angular
552 error estimates for WBVs are likely to be pessimistic. We used theoretical models shown in
553 Fig. 3 with added orientation noise, and calculated **W** for the noisy datasets. Larger stencils
554 and tiles take into account more orientation measurements and, in common with other
555 averaging methods, we hypothesised in Wheeler et al. (2009) that this would give higher
556 precision. We examine this idea in Appendix 3. First, we calculate the error on WBV, by
557 comparing actual **W** and theoretical $\mathbf{W}_c$ values. We find that the error in WBV magnitudes **E**
558 = **W** – $\mathbf{W}_c$ are not strongly dependent on length W, or on whether the model is tilt or twist,
559 but they do depend on stencil size. To quantify the errors, we calculate a standard deviation σ
560 for the vector **E** as described in Appendix 3. Larger stencils and tiles give smaller errors (Fig.
561 6). So, if one uses stencils (i.e the differential method), there is an approximate relationship
562 between W precision and the area S of a stencil (number of points, hence dimensionless)

563 $$\sigma_S = 0.0247S^{-1}/u \qquad (7)$$

564 where *u* is step size.

565 If one uses tiles (i.e. the integral method) and defines the dimensionless area T of a tile the
566 standard deviation $\sigma_T$ of vector E is:

567 $$\sigma_T = 0.0081T^{-3/4}/u\ . \qquad (8)$$

Figure **8.** a) Standard deviation σ of nondimensionalised WBV magnitude plotted against calculation region size for tilt and twist models, showing errors are independent of the detailed nature of distortion. The three left-hand points are for stencils, the others are for tiles. b) Same, plotted against areas of stencils and tiles for both tilt and twist models. c) Same as b) but plotted as log-log graphs to show linear relationships.

568

In Wheeler et al. (2009) we suggested that the integral method would have higher precision than the differential method because numerical integration is less sensitive to errors than numerical differentiation. Our assertion was correct because we were using small stencils (P = 9) and large integral loops. Fig. 8 b) and c) show that in fact the precision depends mainly on the area of the tile or stencil used. The integral method remains our favoured method for initial exploration since the calculation is much faster than for a stencil of comparable size.

The second stage of error analysis involves the angular errors. These *do* depend on the length W as described above and in Fig. 8. The inset in Fig 5c) suggests that $\delta \approx \varepsilon/W$ when errors are small. This is in accord with Fig. S1. One might then expect some proportionality between measures of vector error $\sigma$ and angular error $\alpha_{95}$ in a more rigorous approach, and this is confirmed in Appendix 3. For small errors we have

$$\alpha_{95} \cong 1.413\frac{\sigma}{W}$$

For example, in Table 1, for the second Mg example we have a step size of 4 μm and calculated the WBV using a stencil area 9 so $\sigma_s = 0.000686$ μm$^{-1}$. For a WBV length 0.004 μm$^{-1}$ we have

$$\alpha_{95} \cong 1.413\frac{0.000686}{0.004} = 0.24\,rad = 13.8°$$

(the table calculation is more precise). If we compare the calculated $\alpha_{95}$ with Fig. 7c), it is plausible that the dislocations are all basal and we see a scatter up to 14° away from the basal plane, broadly in accord with the calculation. The above assessment of precision should be used with caution, since it assumes a particular range of orientation errors in the measured data, and those errors are dependent on acquisition conditions and the mineral being measured. A larger stencil or tile will give a more precise measure of WBV magnitude and direction, but larger regions are also more likely to contain more than one type of dislocation. There is a trade-off between finding a relatively precise WBV direction in a large region that may contain more than one type of GND, versus finding a less precise direction in a smaller region which may relate to a single type of GND.

Our error analysis is numerical rather than algebraic but simple calculations give confidence that, if other parameters are maintained, the WBV angular error will scale linearly with orientation angular error. Thus, if angular errors are distributed uniformly between 0 and 0.001 rad, we expect angular errors in WBV to be 10 times less than those we present here. Such low indexing errors are now routinely possible, albeit with a trade-off on indexing speed (Nicolay et al. 2019). Improved indexing would allow for use of a smaller stencil or tile ensure a particular level of WBV precision. We note that algorithms that assign interpolated orientations to misindexed or non-indexed pixels may have adverse effects on subsequent WBV calculations. For example, if the orientation value of an adjacent pixel is used, this guarantees that there is a zero orientation gradient between those two pixels, which may have a big (and spurious) influence on the WBV calculation. Ideally, analysis is done only on confidently indexed points. We also urge caution using dictionary indexed EBSD maps (De Graef 2020) for WBV calculations, because the orientations stored in the dictionary of Kikuchi patterns are discrete and orientation gradients therefore will be stepped. This may give a spurious influence on WBV calculations.

## 3. WBV applications in Earth Sciences: examples

The published works in Table 1 show a variety of approaches for interpreting WBV. The basic algorithms we use do *not* decompose the WBV down into individual Burgers vectors because to do this requires additional assumptions, dependent on the particular mineral and its microstructural evolution. For example, a WBV parallel to [100] may result from a single population of GNDs with Burgers vectors parallel to [100], or a mix of dislocations with [110] and [1-10]. In some phases, prior knowledge of likely Burgers vectors will mean there is only one choice for decomposition – e.g. if such a WBV is found in olivine. In the following, we present first two new examples of WBV usage and then comment on published examples.

Figure **9.** Example of WBV applied to olivine. a) IPF map of Y direction of deformed single crystal of olivine. Scale bar is 1000 μm. b) IPF key. c) IPF coloured as in a), showing a few degrees of distortion within a single initially undeformed crystal. d) WBV magnitude map calculated on 10 x 10 tiles. e) IPF map of WBV direction (calculated as in (d)) superimposed on a band contrast greyscale map; minimum length 0.001 $\mu m^{-1}$. f) IPF of WBV as in (e). g) WBV magnitude map calculated on 3 x 3 stencils in part of overview map shown as white box in (d). Scale bar is 1000 μm. Inset shows orientation variation (degrees) from left hand end of transect marked by white line. h) IPF map of WBV direction (calculated as in (g)) superimposed on a band contrast greyscale map; minimum length 0.00005 $\mu m^{-1}$, showing subgrain walls with [100] Burgers vectors running NE and those with [001] running NW. White squares indicate results of the integral method, with numbers in $\mu m^{-2}$ expressed as coefficients of crystal basis vectors (K values). i) IPF of WBV as in (h).

### *3.1. Olivine: subgrain wall analysis free from trace, or tilt or twist assumptions*

Fig. 9 shows an experimentally deformed single crystal of olivine (PI-1766) as in Fig. 8 of Tielke et al. (2017). The experiment was set up so that the Y (shortening) direction was initially parallel to $[101]_c$, at 45∘ to [100] and [001], with an expectation that slip systems with [100] and [001] Burgers vectors would be activated. The orientation map (a) shows the crystal direction that is parallel to the Y sample direction, in accord with the IPF key (b). We refer to such maps as "IPF Y maps" below. The colour variations reveal rather straight subgrain walls running in two directions. Orientations vary over a few degrees (c). Fig 9(d) shows 10 x 10 tiles colour coded by WBV magnitude and (e) by direction, superimposed on the band contrast greyscale map. The size of the tiles reduces $\alpha_{95}$ but the threshold length for display is set low, at 0.00005/μm, so $\alpha_{95}$ is 26°.With this in mind, the IPF Fig 9f) is, within error, in accord with a mix of dislocations with [100] and [001] Burgers vectors, and the dominant blue colour on the map indicates mainly [100]. Figs (g) and (h) show a subarea with WBV now calculated using a 3 × 3 stencil, giving less precision but more spatial resolution and revealing individual subgrain walls. Blue subgrain walls running NE are consistent with being [100] tilt boundaries and red subgrain walls running SE are consistent with being [001] tilt boundaries. A higher threshold length for display (0.001/μm) means $\alpha_{95}$ is 14° and the IPF in Fig. (i) is in accord with that, insofar as most points are within 14° of the plane containing [100] and [001]. There are still mixtures of [100] and [001]. Some will result from where the stencil overlapped subgrain wall junctions, but as Fig. (h) shows, these

mixtures also appear along irregular segments of the NW-SE subgrain walls and are likely to represent two types of GND in an individual wall. The three square "loops" show results of the integral method and provide additional illustration of how the WBV is averaged over the sample area. Each triplet of numbers is a list of K values, i.e. the coefficients defining the WBV when it is expressed in crystal basis vectors (eqn (5)). The numbers have the dimensions of dislocation density but must be interpreted with care, as discussed above and shown in Fig. 4, since the dislocations are in discrete walls.

In this example the directional information is more useful than the density information: integral and differential methods both give information about where GNDs with [100] and [001] occur. Note that examining the subgrain wall traces together with misorientation axes deduced from the distortion (Fig. 9c) could yield similar results. However, that approach would involve manual and subjective selection of boundary segments and of subregions from which to use misorientation data; it would be based on assumptions about pure tilt or twist boundary character and errors would be difficult to assess. Use of WBV does not preclude further analysis (e.g. Wieser et al. (2020)) but provides a firm foundation.

*3.2. Plagioclase: distributed deformation analysis free from slip system assumptions*

Fig. 10 shows plagioclase from a deformed gabbro from close to the slow spreading mid ocean ridge in the SW Indian Ocean (sample ODP 176-735B-95R-2 from approx. 546 m below the ocean floor). The plagioclase is highly strained, with two prominent ribbons bent around an augite porphyroclast (grey scale on right). Trails of smaller grains are interpreted as new grains due to recrystallization. Hornblende marginal to pyroxene suggests deformation is amphibolite facies, as recorded deeper in the leg (Gardner et al. 2020), but it may have been higher temperature. Our aim here is to not to offer a full interpretation of how the microstructure evolved, but to show how the WBV tools assist in that task.

Figure **10.** Example of WBV applied to plagioclase. Figure layout is similar to Fig. 9 but contouring is used to reveal dominant directions. a) IPF map of plagioclase Y direction of a deformed gabbro. Inset shows orientation variation (degrees) from top end of transect marked by white line. The right-hand porphyroclast is augite rimmed by hornblende. b) Key for IPF map colour scheme. c) IPF map of plagioclase as in a), contoured with intervals at 0.1 x uniform. d) Magnitude of WBV calculated on 20 x 20 tiles in area a) superimposed on a band contrast greyscale map. e) IPF map of WBV calculated as in d) colour coded by WBV direction using b), minimum length 0.0005 $\mu m^{-1}$. f) IPF of WBV as in d) and e), contoured in multiples of uniform. g) Magnitude of WBV calculated on 3 × 3 stencils in white box subarea of map d) superimposed on a band contrast greyscale map. h) IPF map of WBV calculated as in g) colour coded by WBV direction as in b), minimum length 0.01 $\mu m^{-1}$. i) IPF of WBV as in g) and h).

The IPF Y map (Fig. 10a), colour coded as in 10b)) indicates rather smooth variations in orientation for the large grain, in contrast to the olivine example Fig. 9a). Large tiles used in Fig 10d) confirm this, showing a rather uniform level of distortion on the scale of the tiles through the two ribbons. The WBV IPF map (Fig. 10e)) shows <100> dominates at the top of the left hand ribbon, whilst <001> dominates at the bottom, and the IPF (Fig. 10f)) combines these. In and around new grains no data is displayed (Fig. 10d and e) because the 20 × 20 pixel tiles are large enough to cover several small grains and include high (> 5°) angle

boundaries. Thus, in these areas WBV analysis is not appropriate. It is worth considering whether the apparent variation in WBV direction is a stereological effect, like that shown in Fig. 3h), j). Could the ribbon have a relatively uniform population of GNDs, but with a stereological bias governed by varying orientation? The misorientation from bottom to top of (for example) the left-hand ribbon is about 35° in contrast to Fig. 3h), j) which involved 90° of twist. We conclude it is likely that there are real variations in the GND population in this grain, which is not surprising given the stretch and non-uniform bending it has enjoyed. Fig 10g)-i) shows WBV calculated using the differential method on a subarea marked with a white box in Figs. 10d and e. In Fig 10g), boundaries above 5° are shown in black and the highest distortions i.e. WBV magnitude are shown not in the large ribbons but in small grains interpreted as products of dynamic recrystallization. Fig. 10h) and i) show WBV direction, with a pronounced maximum close to <001> as illustrated by the preponderance of red colours in new grains in (h) and a contoured maximum near <001> in (i). The relict ribbon in centre right of Fig. 10h) shows two left-right tapered zones coloured green, indicating WBV rather close to <-100> and in accord with the tiling in Fig. 10e).

In summary this example shows how the integral (here, tiling) and differential methods may be used to interrogate different parts of the microstructure. The interiors of the plagioclase ribbons have relatively low dislocation densities, with GNDs with Burgers vectors combining <100> and <001>, likely in different proportions in different parts. Here, the integral method is a very effective tool. For the small grains, interpreted as recrystallized, the differential method is helpful; they have higher dislocation densities and various Burgers vectors but with an emphasis on <001>. In tectonites small grains are often interpreted as new, forming by static or dynamic recrystallisation from strongly plastically deformed large old grains, and are relatively strain free. Intriguingly, here the small grains are more distorted than the old ribbons though normally one would expect them to be relatively strain free. Further WBV investigation will assist in understanding the evolution of that microstructure. Methods including the traces of subgrain walls could not be used here, since distortion is distributed; methods assuming slip systems and dislocation line energies could be applied but the required inputs may be difficult to constrain in a mineral like plagioclase. As in the olivine example, we suggest the WBV approach provides a firm foundation on which other analyses can be built if required.

### *3.3. Ice: investigation of non-basal slip*

Figure **11.** Example of WBV applied to a subgrain in ice, modified from Fig. 2 of Chauve et al. (2017). WBV is colour coded not by the full IPF but just by the sin of the angle of the WBV from the basal plane, i.e. (component of W parallel to c)/W. This runs between 0 and 1 as shown by the colour scale. Red arrows show the WBV projected onto the map plane, using its actual length not just its direction. Black line is a subgrain wall of 5° or more misorientation.

There is ongoing research into the role of non-basal slip in ice, since if that is active it will alter the rheology of ice sheets (Chauve et al. 2017, Piazolo et al. 2015, Weikusat et al. 2011). Chauve et al. (2017) undertook deformation experiments on ice and Fig. 11a), modified from Fig. 2 of that paper, shows a subgrain from an experiment run at -7 °C and 0.5 MPa stress. The WBV is colour coded not by the full IPF but just by the sin of the angle of the WBV

712 from the basal plane, i.e. (component of W parallel to c)/W. For this dataset we estimate $\alpha_{95}$
713 as 32° (Table 1). The yellow vertical subgrain wall indicates angles near 90° from the basal
714 plane so, even though the errors are large, there is negligible probability that these WBVs lie
715 in the basal plane. Moreover, the colours along this wall are quite consistent, adding credence
716 to the diagnosis that the WBV is subparallel to c. It does not immediately imply that
717 individual Burgers vectors are parallel to c: for example, there could be a mixed population of
718 c + a and c - a, bearing in mind the WBV is a vector average. Further data and/or assumptions
719 are required to determine this. However, as noted above the WBV cannot contain "phantom"
720 directions: it must be the weighted average of Burgers vectors that are actually present in the
721 microstructure, and here must include non-basal vectors of some sort. The Figure also
722 provides an example of WBVs drawn in red as vectors in sample coordinates. As discussed
723 above and derived in Appendix 1, there is only one such choice at each point, regardless of
724 crystal symmetry. Despite $\alpha_{95}$ being predicted as 32°, the WBV directions along each wall
725 segment are quite consistent, suggesting the angular errors are in fact lower, though further
726 work is required to confirm this.

727 *3.4. Titanite: discovery of new slip system*
728 Fig. 12 shows the use of tiling in a study of deformed titanite, modified from Timms et al.
729 (2019). The titanite grain is from a shocked granitoid from the Chicxulub impact structure,
730 Mexico, and the study searched for slip systems activated under extreme stresses, which
731 would not necessarily correspond to slip systems documented from other settings. The study
732 included a boundary trace/misorientation approach, but that assumed pure tilt boundaries, so
733 the WBV method was used for independent verification. The differential method gave a wide
734 scatter of WBV directions so to reduce errors 20 × 20 pixel tiles were used. The tiles are
735 colour coded in terms of IPF direction; missing colours indicate either that the tile includes a
736 high angle boundary, or the WBV magnitude is below the threshold for display (Table 1).
737 There are many shock-induced twins, and the abundance of those high angle boundaries
738 mean that tile coverage is sparse. However, the WBV directions show a strong maximum
739 near <341>. This is a Burgers vector not previously described in titanite but likely indicating
740 a dislocation slip system operating concurrently with twinning under shock.

Figure **10.** Example of WBV applied to titanite. The greyscale map is of band contrast in a shocked titanite grain and its surroundings, redrawn from Fig. 8 of Timms et al. (2019). Inset shows orientation variation (degrees) from lower left end of transect marked by thick black line. Tiling was used to analyse the microstructure – tiles are coloured for WBV direction in accordance with the IPF key on bottom left. The WBV IPF (top right) shows distinct preferred directions. Calculation and display parameters are given in Table 1.

741

742 *3.5. WBV precision in specific studies*
743 In Table 1 we compile the parameters required for estimating $\alpha_{95}$ from previous studies
744 making a big assumption, that the orientation measurement errors in those studies are all
745 distributed uniformly between 0 and 0.01 radians. Despite this, the error estimates are in
746 general agreement with the appearance of the relevant IPFs. For example, for Mg metal Fig. 7
747 shows IPFs with $\alpha_{95}$ of 28° and 14°, and those angles are in accord with the scatters of points
748 if all WBVs are in fact in the basal plane. One large $\alpha_{95}$ = 110° is for quartz and relates to
749 Fig. 15 of Wheeler et al. (2009), but the left hand IPF there was drawn to specifically

illustrate the effect of choosing a threshold W that is too low. The cone of error would cover the entire IPF and that is in accord with the random scatter of points seen. In contrast, another study is predicted to have a large $\alpha_{95}$ of 110° yet the IPFs show strong maxima. Fig. 4 of Kendrick et al. (2017) shows IPFs of WBV for deformed plagioclase microlites in an andesite with strong maxima around [001], particularly in the experimentally deformed sample. We suggest this is because there is a single family of GNDs with a single [001] Burgers vector. Then, even though individual WBVs have large errors, the maximum is strong because the errors cancel out to some extent. This is analogous to a standard result in statistics of a single variable: the standard variation of the mean is equal to the standard deviation of an individual measurement divided by the square root of the sample size. A similar idea might be developed for directional statistics in future work.

## 4. Comparison of WBV with other methods used for analysing GND directional data

All 6 orientation gradients (3 in x and 3 in y) can be calculated from EBSD maps and provide 6 constraints on the Nye curvature tensor as in (Pantleon 2008), Wilkinson and Randman (2010), Wallis et al. (2016). If there are 6 types of dislocation, then eqn (3) has a unique solution for 6 GND densities, given the 6 constraints on the Nye tensor. In many materials, particularly cubic phases, symmetry indicates there are more than 6 types of slip system and there is no unique solution for eqn (3). So, an additional assumption is made, that the total line energy of all the dislocations involved is the minimum out of all the possible solutions.

This approach uses more information than the WBV method (6 components of the Nye tensor versus 3) but is based on assumptions that we recommend deserve appraisal on a mineral-by-mineral basis.

i) Assumptions about allowable slip systems might be misleading as we do not have a complete knowledge of all in all minerals.

ii) Assumptions about the line energies of each type of dislocation, to enable overall energy minimisation if there are more than 6 slip systems, will be based on limited information for minerals.

iii) Assuming that the types of dislocation related to slip also characterise growth defects deserves scrutiny. For growth the concept of slip systems is not relevant: there might be alternative lists of allowable GND types, but again in minerals such information is scanty.

iv) Assuming that dislocations have locally reorganised to minimise their net energy may not be true (e.g. in cold working, or when defects are due to growth).

In contrast WBV calculation makes no assumptions about GND types at any stage of the calculations. Instead, individual studies tailor the interpretation, possibly involving further calculation, based on the problems being addressed. This is well illustrated in the published ice non-basal slip example outlined above. Here, the hypothesis to be tested was to identify if non-basal dislocations are present in ice, tested by calculating and displaying the angle of the WBV to the basal plane (Chauve et al. 2017). The calculation is free from detailed assumptions about dislocation types and energies, which are not well known. A further example is provided in Wieser et al. (2020) who used the trace of subgrain walls together with WBV analysis to provide additional constraints on potential activated slip systems. In this case, additional assumptions were introduced, e.g. that all subgrain walls were either pure tilt or pure twist. Those assumptions are not intrinsic to the WBV calculation. In essence the

WBV may provide sufficient information on its own and provides a platform for further in-depth analysis which may use additional assumptions.

In a number of works using the "energy minimisation" method, the EBSD data are high resolution electron backscatter diffraction (HREBSD) which gives higher angular accuracy to orientation measurements: for details see Wilkinson and Randman (2010), Wallis et al. (2016) and Wallis et al. (2019a). This means that errors in misorientation gradients and hence WBV or other calculations will be lower than using conventional data (Gardner et al. 2024). However, there is no intrinsic difference in applying WBV or energy minimisation calculations to HREBSD versus conventional data or to data obtained with new techniques e.g. (Winkelmann et al. 2020). WBV ~~could~~ can be calculated from HREBSD data, as in Wallis et al. (2016) and Gardner et al. (2024). Equally, best fit/energy minimisation can be used on Hough based orientation data as in Pantleon (2008).

## 5. Summary and discussion

We have described the theoretical basis for the WBV method and shown examples where it has assisted in deducing Burgers vectors for slip systems in various minerals. Since the method is purely geometric it can also be used to analyse distortions due to growth as in Gardner et al. (2021). Key aspects of the WBV method are as follows.

- It makes no assumptions about the dislocation populations being investigated.
- It uses just the three numbers defining orientation at each measurement point, so is fast.
- It assumes there are no significant grain scale elastic strains.

The software we use in this contribution ("Crystalscape") involves user-defined parameters for calculation as follows; these need to be recorded to allow calculations to be reproduced.

- The cutoff angle above which boundaries are assumed to no longer have dislocation substructure.
- The size of the stencil or tile used for systematic calculations.

WBV results can be displayed in several ways and the key user-defined parameters for display are the minimum and maximum WBV lengths. The minimum length can then, together with the other parameters, be used to estimate the angular accuracy $\alpha_{95}$ (the shortest vectors being the least accurate in terms of direction). That estimation contains several simplifications and, in any case, depends on an assumed angular error in the EBSD data; but it serves as an indication of accuracy which proves useful.

For interpretation, the following properties must be borne in mind.

- The WBV does *not* measure the complete GND population or density. It is a sample of that population, weighted towards dislocation lines that intersect the EBSD map at high angles. Maps cut in different planes will show different but related WBV information.
- The WBV is a weighted sum of Burgers vectors of GNDs. In general, there are multiple ways of decomposing the WBV, but it still provides a platform for testing hypotheses. It will never generate "phantom" components. For example, if a trigonal or hexagonal mineral shows WBVs with significant c axis components, there must be GNDs with Burgers vectors involving c (though not necessarily parallel to c).

- Errors in WBV are smaller when larger stencils or tiles are used. Angular errors are smaller for longer WBVs.
- Larger stencils or tiles tend to "smear out" the WBV pattern. Increased angular precision is thus linked to reduced spatial resolution.

Future directions using this method could include further development of ways to characterise non-basal slip in hexagonal and trigonal materials e.g. Chauve et al. (2017). The combination of WBV analysis with subgrain boundary trace analysis (Wieser et al. 2020) has potential to be developed for olivine and other minerals. More advanced statistical tests related to directional data could be developed. We have not discussed 3D orientation data here but in principle this allows calculation of orientation gradients in all three dimensions and hence the complete Nye tensor which would be valuable for constraining GNDs. However, even the 9 components of the Nye tensor are not sufficient to constrain all GND types in very symmetric minerals. Statistical tests could be developed for 3D analysis as we have done in 2D. Hybrid approaches using two or more maps at right angles also deserve investigation.

We note that the methods discussed here are applicable to any crystalline material including metals, ceramics and ice.

The Matlab software used for analysis here ("Crystalscape") is available from the lead author for academic use only. In 2021 Oxford Instruments Nanoanalysis adapted a version of the WBV method for use in Aztec Crystal, their EBSD analysis suite. This is described here: https://www.ebsd.com/ois-ebsd-system/dislocation-density-analysis and in a webinar here https://register.gotowebinar.com/register/5472775566652982031. ~~To safeguard the commercial development, Crystalscape for academic use only.~~

**Credit author statement**

**John Wheeler:** Conceptualization, Software, Writing - Original Draft, Visualization; **Sandra Piazolo:** Conceptualization, Writing – Review and Editing; **David Prior:** Conceptualization, Writing – Review and Editing; **Patrick Trimby:** Conceptualization, Resources, Writing – Review and Editing; **Jake Tielke:** Resources, Writing – Review and Editing.

**Acknowledgements**

We thank all the user of the WBV method who have contributed through discussion to developing the method. We thank Elena Miranda and David Wallis for constructive reviews and Virginia Toy for substantial editorial work.

**Table 1. Details of published WBV studies, and the new studies here**

Table 1. Published papers using WBV on minerals, with precision estimates added in this contribution. We include one example of use on Mg metal as it helps illustrate the basic ideas. In the right hand columns we have compiled information from the published works ~~so as~~ to estimate $\alpha_{95}$ based on the assumption that orientation measurement errors are distributed uniformly between 0 and 0.01 radians, a realistic if somewhat pessimistic range for data obtained by Hough transform.~~-~~

| Crystal system | Laue group | Phase | weighted Burgers vector study motivation | Reference | Figure in referenced paper | Integral method used? | Stencil or tile | Sampled area (pixels) | Step size (μm) | W minimum length ((μm)$^{-1}$) | $\alpha_{95}$ (deg) |
|---|---|---|---|---|---|---|---|---|---|---|---|
| Cubic holosymmetric | m3m | Periclase | example | (Wheeler et al. 2009) | Fig 11 | | s | 9 | 10 | 0.0015 | 14.9 |
| Cubic | m3 | | ***no studies yet published on minerals*** | - | | | | | | | - |
| Hexagonal holosymmetric | 6/mmm | Mg | example | (Wheeler et al. 2009) | Fig 3, 5 | | s | 9 | 4 | 0.002 | 28.1 |
| | | Mg | example | (Wheeler et al. 2009) | | | s | 9 | 4 | 0.004 | 13.9 |
| | | Ti | magnitude display from TKD data | (Trimby et al. 2014) | Fig 5 | | | | 0.01 | | n/a |
| | | Ice | search for non-basal dislocations | (Piazolo et al. 2015) | | | s | 9 | 15 | 0.0004 | 37.7 |
| | | Ice | search for non-basal dislocations | (Chauve et al. 2017) | Fig. 2 | | s | 9 | 5 | 0.0014 | 32.2 |
| | | Ice | intragranular boundary development | (Fan et al. 2022) | Fig. 5 | | s | 9 | 5 | 0.006 | 7.4 |
| Hexagonal | 6/m | | ***no studies yet published on minerals*** | - | | | | | | | - |
| Trigonal holosymmetric | -3m | Quartz | example | (Wheeler et al. 2009) | Fig 15 | | s | 9 | 2 | 0.001 | 110.0 |
| | | Quartz | example | (Wheeler et al. 2009) | Fig 15 | | s | 9 | 2 | 0.003 | 37.7 |
| | | Quartz | compare GND density with density from etch pits | (Billia et al. 2013) | n/a | y | | | | | n/a |
| | | Calcite | deduce slip systems hence deformation T | (Mcnamara et al. 2020) | Fig 4, 5 | | | | | | |
| Trigonal | -3 | | ***no studies yet published on minerals*** | - | | | | | | | |
| Tetragonal holosymmetric | 4/mmm | Zircon | Link magnitude to Pb loss | (MacDonald et al. 2013) | Fig. 9 | y | | | 1, 2, 0.8 | | n/a |
| | | Zircon | Planar deformation bands | (Kovaleva et al. 2015) | Fig. 6 | y | | | | | n/a |
| | | Zircon | help to characterise slip systems | (Kovaleva et al. 2018) | Fig. 6 | y | | | | | n/a |
| Tetragonal | 4/m | | ***no studies yet published on minerals*** | - | | | | | | | - |
| Orthorhombic | mmm | Olivine | confirm slip systems dominated by [100] | (Tielke et al. 2019) | Fig. 5 b | y | s | 9 | 3 | 0.005 | 14.9 |
| | | Olivine | determine slip systems | (Wieser et al. 2020) | Fig. 4, 7 | | | | | | |
| | | Olivine | tiling example | ***this contribution*** | Fig. *7* | y | t | 100 | 16 | 0.00005 | 26.2 |
| | | Olivine | stencil example | ***this contribution*** | Fig. *7* | | s | 9 | 16 | 0.001 | 13.9 |
| Monoclinic | 2/m | Titanite | Diagnose slip systems: map showing WBV direction (6 μm tiles) | (Timms et al. 2019) | Fig. 8c | | t | 400 | 0.3 | 0.001 | 24.6 |
| | | Titanite | Contoured IPF showing WBV direction (2.4 μm tiles) | (Timms et al. 2019) | Fig. 8e | | t | 64 | 0.3 | 0.003 | 32.6 |
| Triclinic | -1 | Plagioclase | Diagnose slip system in naturally and experimentally deformed microlites; latter show [001] clearly; both show it in loops | (Kendrick et al. 2017) | Fig. 4 | | s | 9 | 0.2 | 0.01 | 110.0 |
| | | Plagioclase | Understand plagioclase replacement by albite | (Gardner et al. 2021) | Fig. 6 | | s | | | | |
| | | Plagioclase | tiling example | ***this contribution*** | Fig. *8* | y | t | 400 | 1 | 0.0005 | 14.7 |
| | | Plagioclase | stencil example | ***this contribution*** | Fig. *8* | | s | 21 | 1 | 0.01 | 9.5 |

## References


Ashby, M. F. 1970. Deformation of plastically non-homogeneous materials. *Philosophical Magazine* **21**(170), 399-424.

Billia, M. A., Timms, N. E., Toy, V. G., Hart, R. D. & Prior, D. J. 2013. Grain boundary dissolution porosity in quartzofeldspathic ultramylonites: Implications for permeability enhancement and weakening of mid-crustal shear zones. *Journal Of Structural Geology* **53**, 2-14.

Butler, R. F. 1992. *Paleomagnetism: Magnetic Domains to Geologic Terranes*. Blackwell Scientific Publications.

Chauve, T., Montagnat, M., Piazolo, S., Journaux, B., Wheeler, J., Barou, F., Mainprice, D. & Tommasi, A. 2017. Non-basal dislocations should be accounted for in simulating ice mass flow. *Earth And Planetary Science Letters* **473**, 247-255.

Das, S., Hofmann, F. & Tarleton, E. 2018. Consistent determination of geometrically necessary dislocation density from simulations and experiments. *International Journal Of Plasticity* **109**, 18-42.

De Graef, M. 2020. A dictionary indexing approach for EBSD. *IOP Conference Series: Materials Science and Engineering* **891**, 012009.

Drury, M. R. & Urai, J. L. 1990. Deformation related recrystallization processes. *Tectonophysics* **172**, 235-253.

Fan, S., Wheeler, J., Prior, D. J., Negrini, M., Cross, A. J., Hager, T. F., Goldsby, D. L. & Wallis, D. 2022. Using misorientation and weighted Burgers vector statistics to understand intragranular boundary development and grain boundary formation at high temperatures. *Journal of Geophysical Research - Solid Earth* **127**(8), 26 pages.

Gardner, J., Wallis, D., Hansen, L. N. & Wheeler, J. 2024. Weighted Burgers Vector analysis of orientation fields from high-angular resolution electron backscatter diffraction. *Ultramicroscopy* **257**, 113893.

Gardner, J., Wheeler, J. & Mariani, E. 2021. Interactions between deformation and dissolution-precipitation reactions in feldspar at greenschist facies. *Lithos* **396-397**.

Gardner, R. L., Piazolo, S., Daczko, N. R. & Trimby, P. 2020. Microstructures reveal multistage melt present strain localisation in mid-ocean gabbros. *Lithos* **366**.

Guillopé, M. & Poirier, J. P. 1979. Dynamic recrystallization during creep of single-crystal halite: an experimental study. *Journal of Geophysical Research* **84**, 5557-5567.

Hildyard, R. C., Prior, D. J., Faulkner, D. R. & Mariani, E. 2009. Microstructural analysis of anhydrite rocks from the Triassic Evaporites, Umbria-Marche Apennines, Central Italy: An insight into deformation mechanisms and possible slip systems. *Journal Of Structural Geology* **31**(1), 92-103.

Jiang, J., Britton, T. B. & Wilkinson, A. J. 2013. Measurement of geometrically necessary dislocation density with high resolution electron backscatter diffraction: Effects of detector binning and step size. *Ultramicroscopy* **125**, 1-9.

Kalácska, S., Dankházi, Z., Zilahi, G., Maeder, X., Michler, J., Ispánovity, P. D. & Groma, I. 2020. Investigation of geometrically necessary dislocation structures in compressed Cu micropillars by 3-dimensional HR-EBSD. *Materials Science and Engineering: A* **770**, 138499.

Kendrick, J. E., Lavallee, Y., Mariani, E., Dingwell, D. B., Wheeler, J. & Varley, N. R. 2017. Crystal plasticity as a strain marker of the viscous-brittle transition in magmas. *Nature Communications* **8**(1), Art. No. 1926.

Konijnenberg, P. J., Zaefferer, S. & Raabe, D. 2015. Assessment of geometrically necessary dislocation levels derived by 3D EBSD. *Acta Materialia* **99**, 402-414.

Kovaleva, E., Klotzli, U., Habler, G. & Wheeler, J. 2015. Planar microstructures in zircon from paleo-seismic zones. *American Mineralogist*.

Kovaleva, E., Klotzli, U., Wheeler, J. & Habler, G. 2018. Mechanisms of strain accommodation in plastically-deformed zircon under simple shear deformation conditions during amphibolite-facies metamorphism. *Journal Of Structural Geology* **107**, 12-24.

Kuhr, B. & Farkas, D. 2019. Dislocation content in random high angle grain boundaries. *Modelling and Simulation in Materials Science and Engineering* **27**(4), 045005.

Lloyd, G. E. 2002. Microstructural evolution in a mylonitic quartz simple shear zone: the significant roles of dauphine twinning and misorientation. In: *Joint International Meeting of the Tectonic-Studies-Group of the Geological-Society London/Structural Geology and Tectonics Division of the Geological-Society-of-America/Geological-Society-of-Australia*. *Geological Society Special Publication* **224**, London, ENGLAND, 39-61.

MacDonald, J. M., Wheeler, J., Harley, S. L., Mariani, E., Goodenough, K. M., Crowley, Q. G. & Tatham, D. 2013. Lattice distortion in a zircon population and its effects on trace element mobility and U–Th–Pb isotope systematics: examples from the Lewisian Gneiss Complex, northwest Scotland. *Contributions To Mineralogy And Petrology* **166**, 21-41.

Mamtani, M. A., Reznik, B. & Kontny, A. 2020. Intracrystalline deformation and nanotectonic processes in magnetite from a naturally deformed rock. *Journal of Structural Geology* **135**, 104045.

Marquardt, K. & Faul, U. H. 2018. The structure and composition of olivine grain boundaries: 40 years of studies, status and current developments. *Physics and Chemistry of Minerals* **45**(2), 139-172.

Mcnamara, D. D., Lister, A., Prior, D. J., Scully, A., Gardner, J. & Wheeler, J. 2020. Microanalysis of Calcite Scaling in a Fractured Geothermal System.

Nicolay, A., Franchet, J. M., Cormier, J., Mansour, H., De Graef, M., Seret, A. & Bozzolo, N. 2019. Discrimination of dynamically and post-dynamically recrystallized grains based on EBSD data: application to Inconel 718. *JOURNAL OF MICROSCOPY* **273**(2), 135-147.

Nye, J. F. 1953. Some geometrical relations in dislocated crystals. *Acta Metallurgica* **1**, 153-162.

Pantleon, W. 2008. Resolving the geometrically necessary dislocation content by conventional electron backscattering diffraction. *Scripta Materialia* **58**(11), 994-997.

Piazolo, S., Montagnat, M., Grennerat, F., Moulinec, H. & Wheeler, J. 2015. Effect of local stress heterogeneities on dislocation fields: Examples from transient creep in polycrystalline ice. *Acta Materialia* **90**, 303-309.

Poirier, J. P. & Nicolas, A. 1975. Deformation-induced recrystallization due to progressive misorientation of subgrains, with special reference to mantle peridotites. *Journal of Geology* **83**, 707-720.

Prior, D. J. 1999. Problems in determining the orientations of crystal misorientation axes, for small angular misorientations, using electron backscatter diffraction in the SEM. *Journal of Microscopy* **195**, 217-225.

Prior, D. J., Mariani, E. & Wheeler, J. 2009. EBSD in the Earth Sciences: applications, common practice and challenges. In: *Electron Backscatter Diffraction in Materials Science* (edited by Schwartz, A. J., Kumar, M., Adams, B. L. & Field, D. P.). Springer, 345-357.

Ram, F., Zaefferer, S., Japel, T. & Raabe, D. 2015. Error analysis of the crystal orientations and disorientations obtained by the classical electron backscatter diffraction technique. *Journal of Applied Crystallography* **48**(3), 797-813.

Shigematsu, N., Prior, D. J. & Wheeler, J. 2006. First combined electron backscatter diffraction and transmission electron microscopy study of grain boundary structure of deformed quartzite *Journal of Microscopy* **224**, 306-321.

Spruzeniece, L., Piazolo, S. & Maynard-Casely, H. E. 2017. Deformation-resembling microstructure created by fluid-mediated dissolution-precipitation reactions. *Nature Communications* **8**.

Sutton, A. P. & Balluffi, R. W. 1995. *Interfaces in crystalline materials*. Clarendon Press, Oxford.

Tielke, J. A., Mecklenburgh, J., Mariani, E. & Wheeler, J. 2019. The influence of water on the strength of olivine dislocation slip systems. *Journal Of Geophysical Research: Solid Earth* **124**, 6542-6559.

Tielke, J. A., Zimmerman, M. E. & Kohlstedt, D. L. 2017. Hydrolytic weakening in olivine single crystals. *Journal of Geophysical Research-Solid Earth* **122**(5), 3465-3479.

Timms, N. E., Pearce, M. A., Erickson, T. M., Cavosie, A. J., Rae, A., Wheeler, J., Wittman, A., Ferriere, F., Poelchau, M. H., Tomioka, N., Collins, G. S., Gulick, S. P. S., Rasmussen, C., Morgan, J. V. & Scientists, I.-I. E. 2019. New shock microstructures in titanite (CaTiSiO5) from the peak ring of the Chicxulub impact structure, Mexico. *Contributions To Mineralogy And Petrology*.

Timms, N. E., Reddy, S. M., Healy, D., Nemchin, A. A., Grange, M. L., Pidgeon, R. T. & Hart, R. 2012. Resolution of impact-related microstructures in lunar zircon: A shock-deformation mechanism map. *Meteoritics & Planetary Science* **47**(1), 120-141.

Trimby, P. W., Cao, Y., Chen, Z., Han, S., Hemker, K. J., Lian, J., Liao, X., Rottmann, P., Samudrala, S., Sun, J., Wang, J. T., Wheeler, J. & Cairney, J. M. 2014. Characterizing deformed ultrafine-grained and nanocrystalline materials using transmission Kikuchi diffraction in a scanning electron microscope. *Acta Materialia* **62**, 69-80.

Trimby, P. W., Prior, D. J. & Wheeler, J. 1998. Grain boundary hierarchy development in a quartz mylonite. *Journal of Structural Geology* **20**, 917-935.

Wallis, D., Hansen, L. N., Ben Britton, T. & Wilkinson, A. J. 2016. Geometrically necessary dislocation densities in olivine obtained using high-angular resolution electron backscatter diffraction. *Ultramicroscopy* **168**, 34-45.

Wallis, D., Hansen, L. N., Britton, T. B. & Wilkinson, A. J. 2019a. High-Angular Resolution Electron Backscatter Diffraction as a New Tool for Mapping Lattice Distortion in Geological Minerals. *Journal of Geophysical Research: Solid Earth* **124**, 6337–6358.

Wallis, D., Parsons, A. J. & Hansen, L. N. 2019b. Quantifying geometrically necessary dislocations in quartz using HR-EBSD: Application to chessboard subgrain boundaries. *Journal of Structural Geology* **125**, 235-247.

Weikusat, I., Miyamoto, A., Faria, S. H., Kipfstuhl, S., Azuma, N. & Hondoh, T. 2011. Subgrain boundaries in Antarctic ice quantified by X-ray Laue diffraction. *Journal of Glaciology* **57**(201), 111-120.

Wheeler, J., Mariani, E., Piazolo, S., Prior, D. J., Trimby, P. & Drury, M. R. 2009. The weighted Burgers vector: a new quantity for constraining dislocation densities and types using Electron Backscatter Diffraction on 2D sections through crystalline materials. *Journal of Microscopy* **233**(3), 482-494.

White, S. 1976. The effects of strain on the microstructures, fabrics, and deformation mechanisms in quartzites. *Philosophical Transactions of the Royal Society of London A* **283**, 69-86.

Wieser, P., Edmonds, M., Maclennan, J. & Wheeler, J. 2020. The Record of Magma Storage under Kīlauea Volcano preserved in Distorted Olivine Crystals. *Nature Communications*.

Wilkinson, A. J. & Randman, D. 2010. Determination of elastic strain fields and geometrically necessary dislocation distributions near nanoindents using electron back scatter diffraction. *Philosophical Magazine* **90**(9), 1159-1177.

Winkelmann, A., Nolze, G., Cios, G., Tokarski, T. & Bała, P. 2020. Refined Calibration Model for Improving the Orientation Precision of Electron Backscatter Diffraction Maps. *Materials* **13**(12), 2816.

Wirth, R. 1996. Thin amorphous films (1–2 nm) at olivine grain boundaries in mantle xenoliths from San Carlos, Arizona. *Contributions to Mineralogy and Petrology* **124**(1), 44-54.

Zhang, Z., Ódor, É., Farkas, D., Jóni, B., Ribárik, G., Tichy, G., Nandam, S.-H., Ivanisenko, J., Preuss, M. & Ungár, T. 2020. Dislocations in Grain Boundary Regions: The Origin of Heterogeneous Microstrains in Nanocrystalline Materials. *Metallurgical and Materials Transactions A* **51**(1), 513-530.

Figure 1



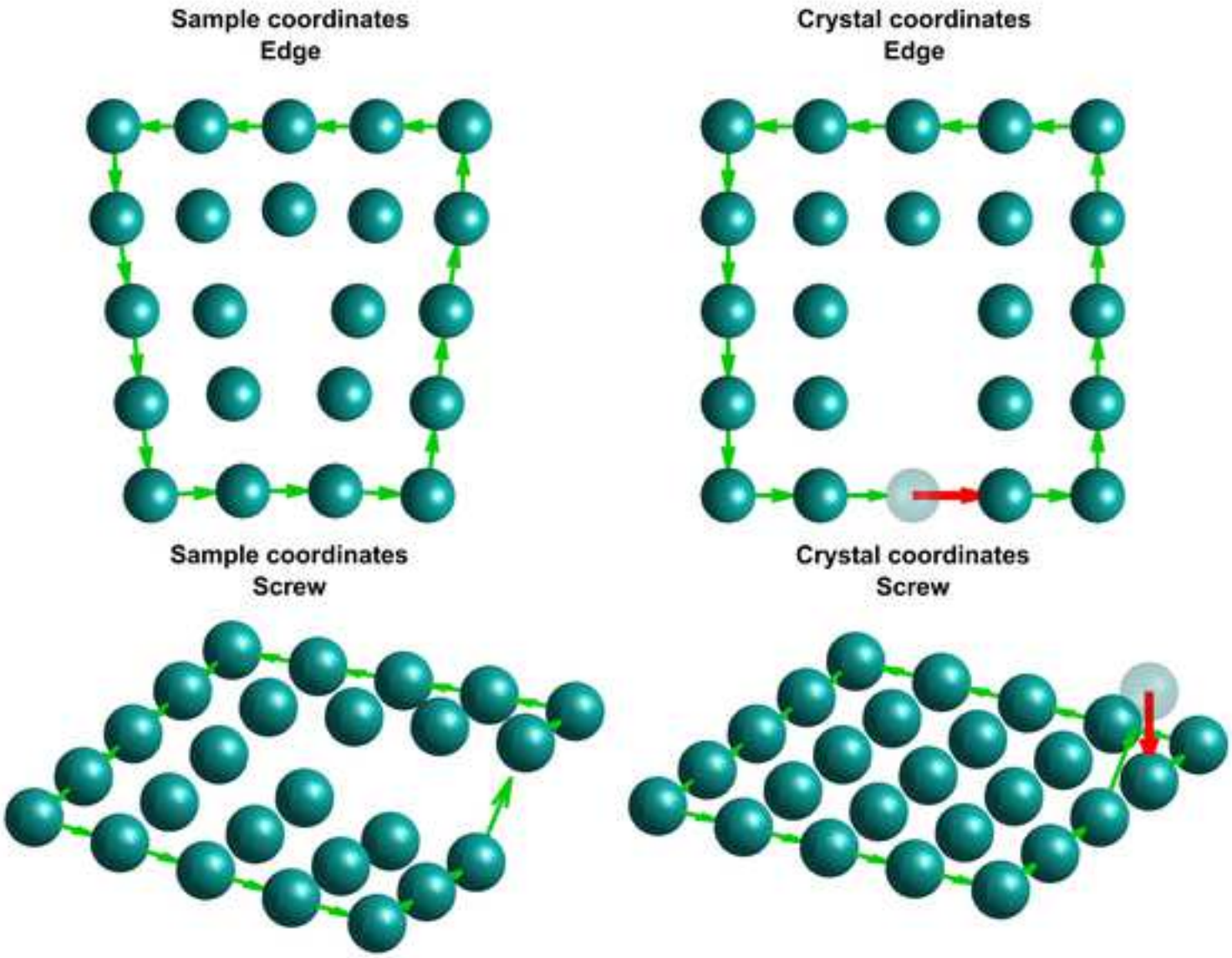

Figure 2

Click here to access/download;Figure;Fig. 2 dislocations curvature SUB.pdf

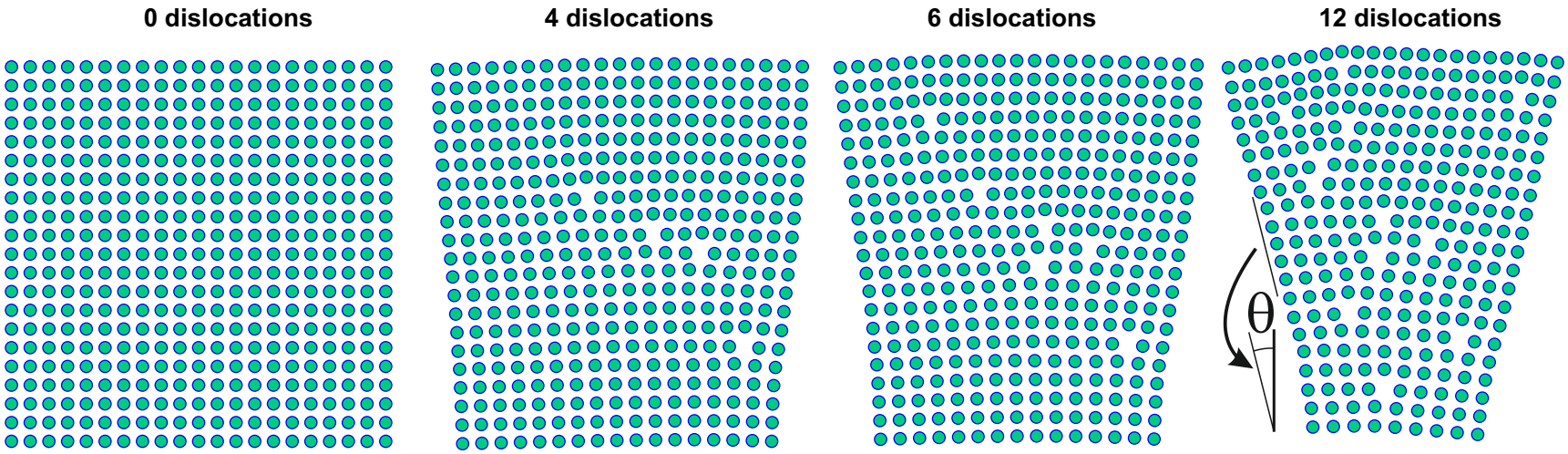

Figure 3

Click here to access/download;Figure;Fig. 3 SUB.pdf

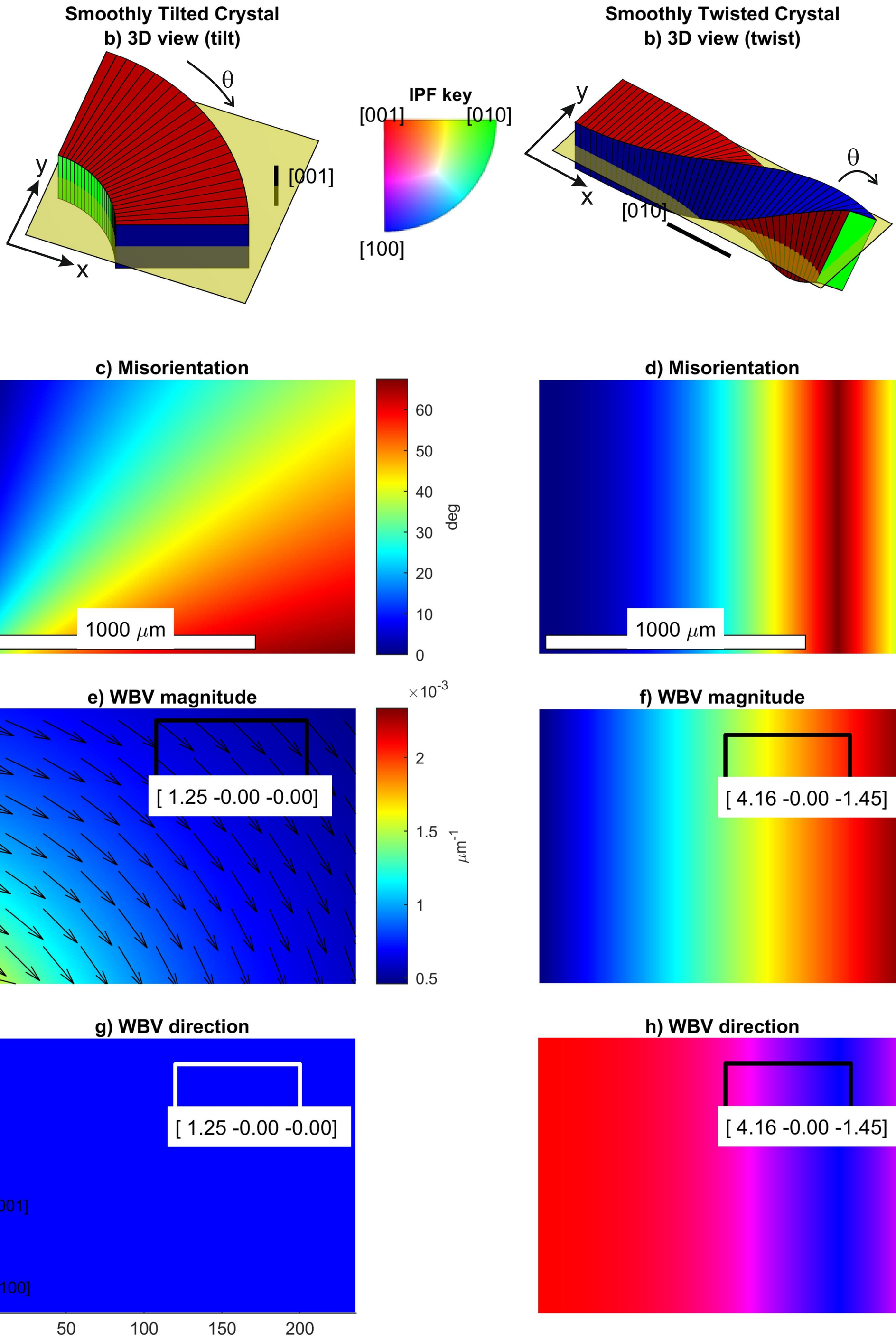

Figure 4

Click here to access/download;Figure;Fig. 4 sgw boxes SUB.pdf

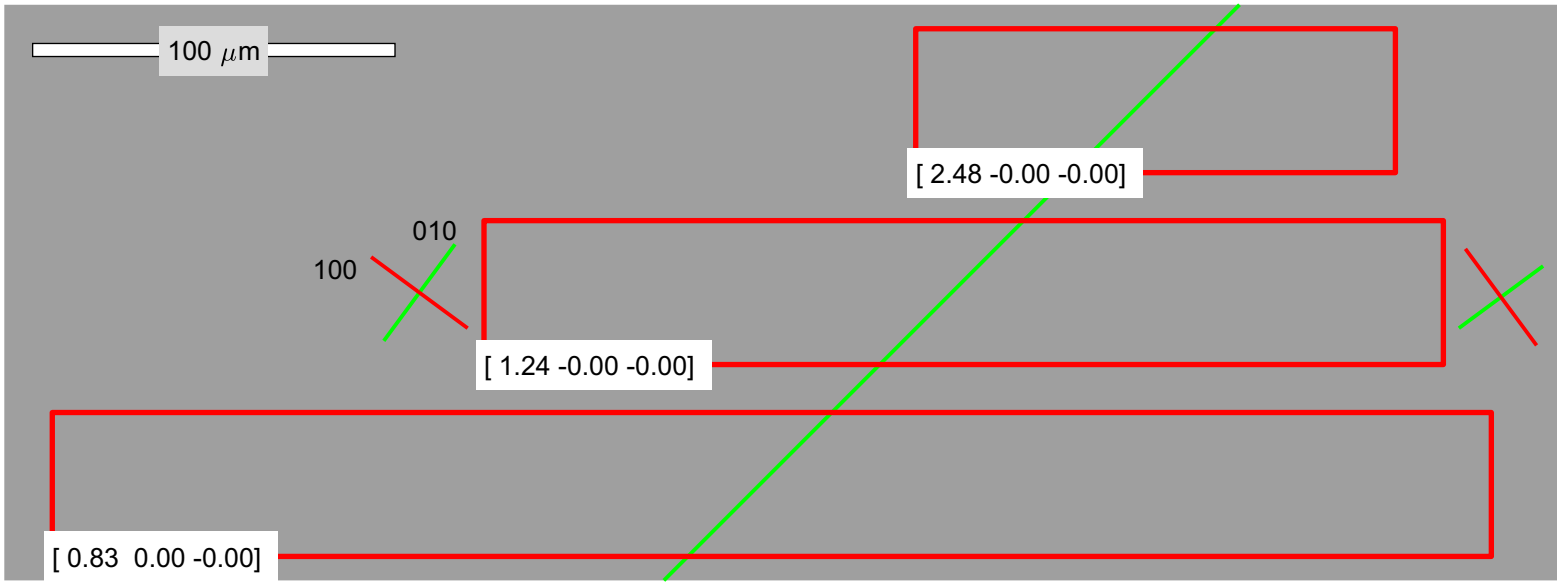

Figure 5

Click here to access/download;Figure;Fig. 5. stencils etc. SUB.pptx

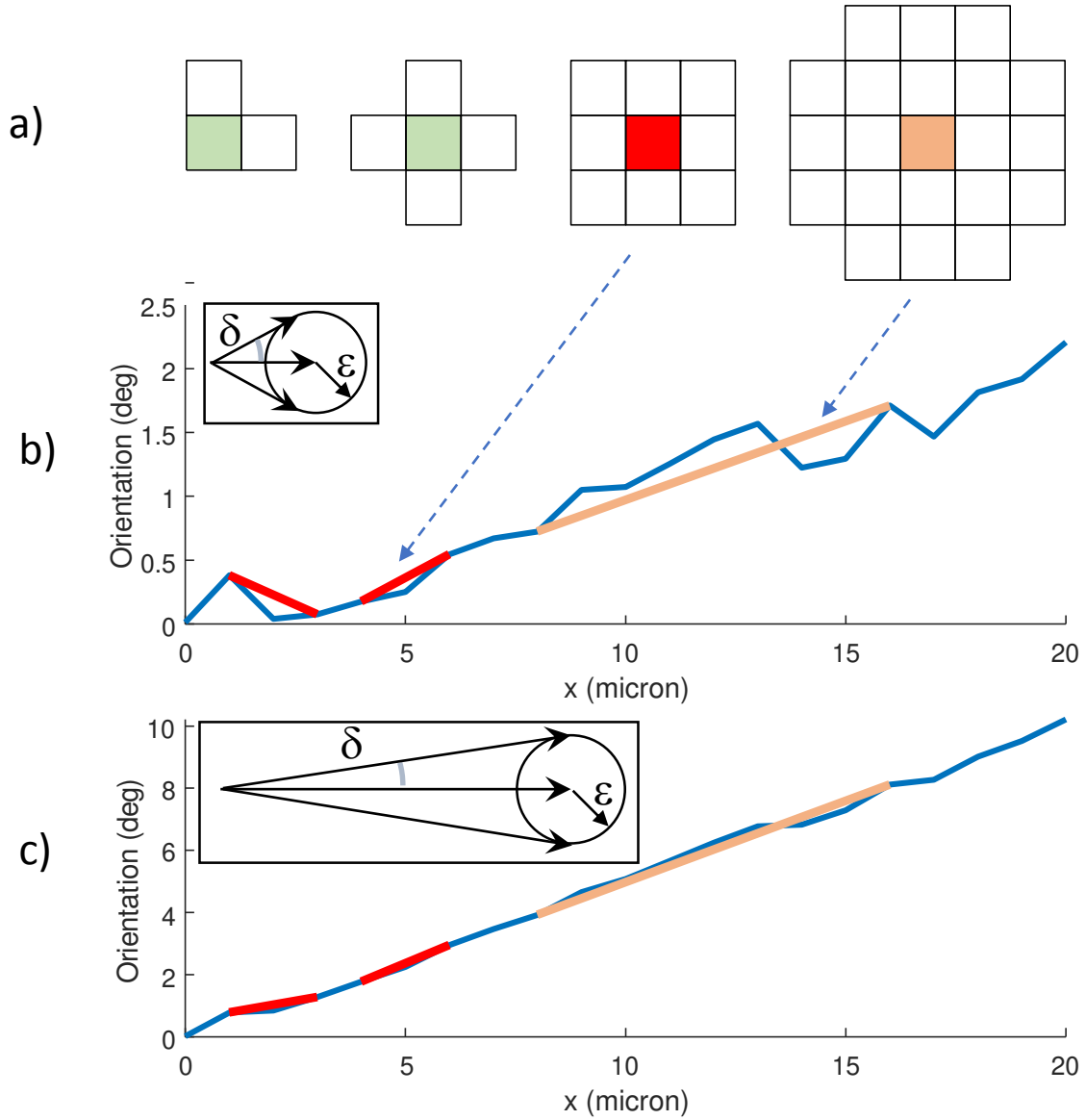

Figure 6

Click here to access/download;Figure;Fig. 6. sten SUB.pdf

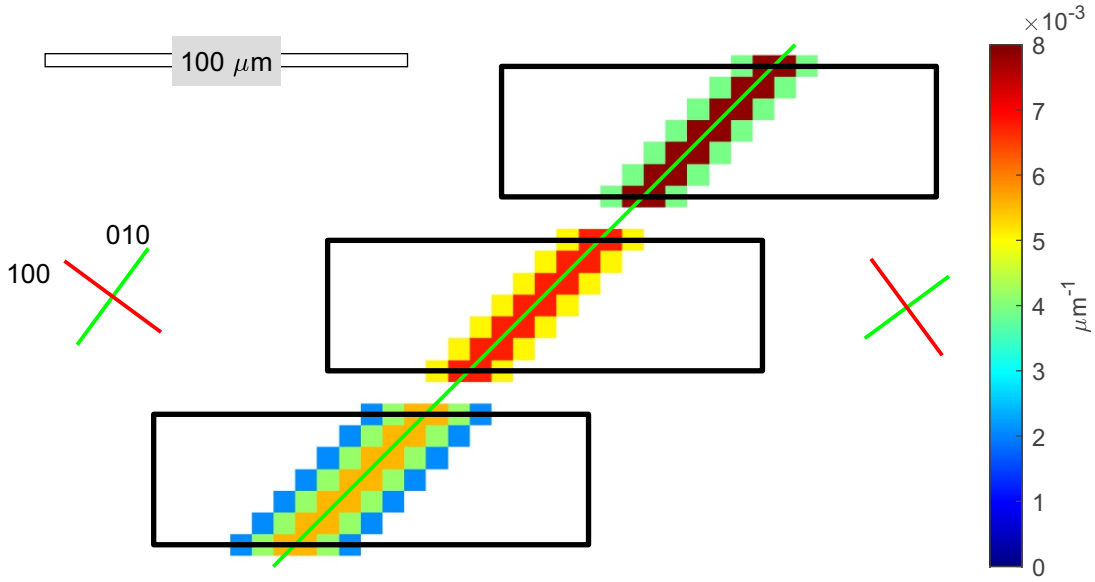

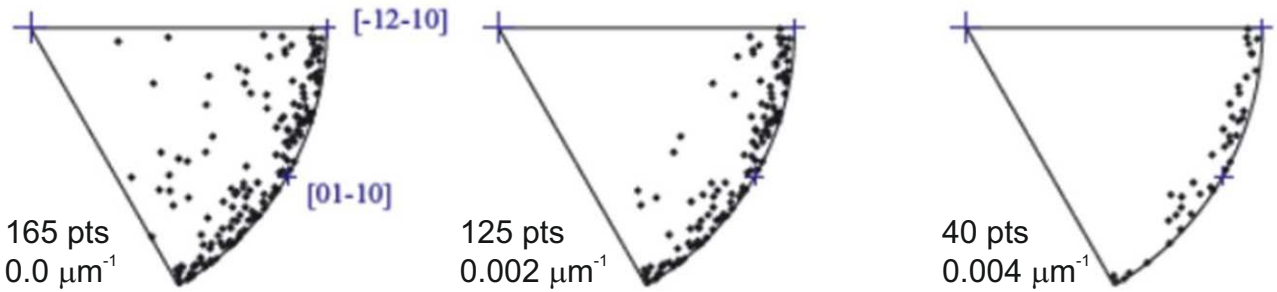

Figure 8

Click here to access/download;Figure;Fi

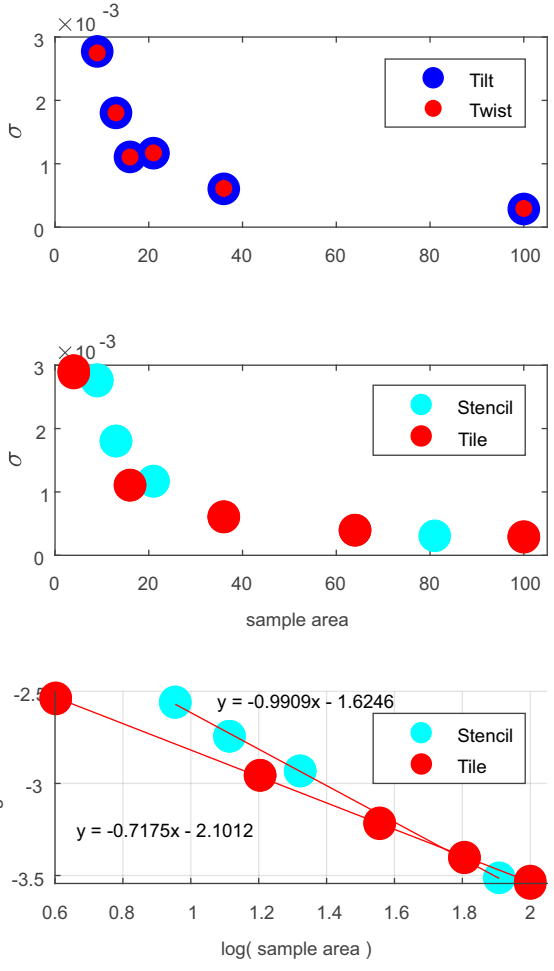

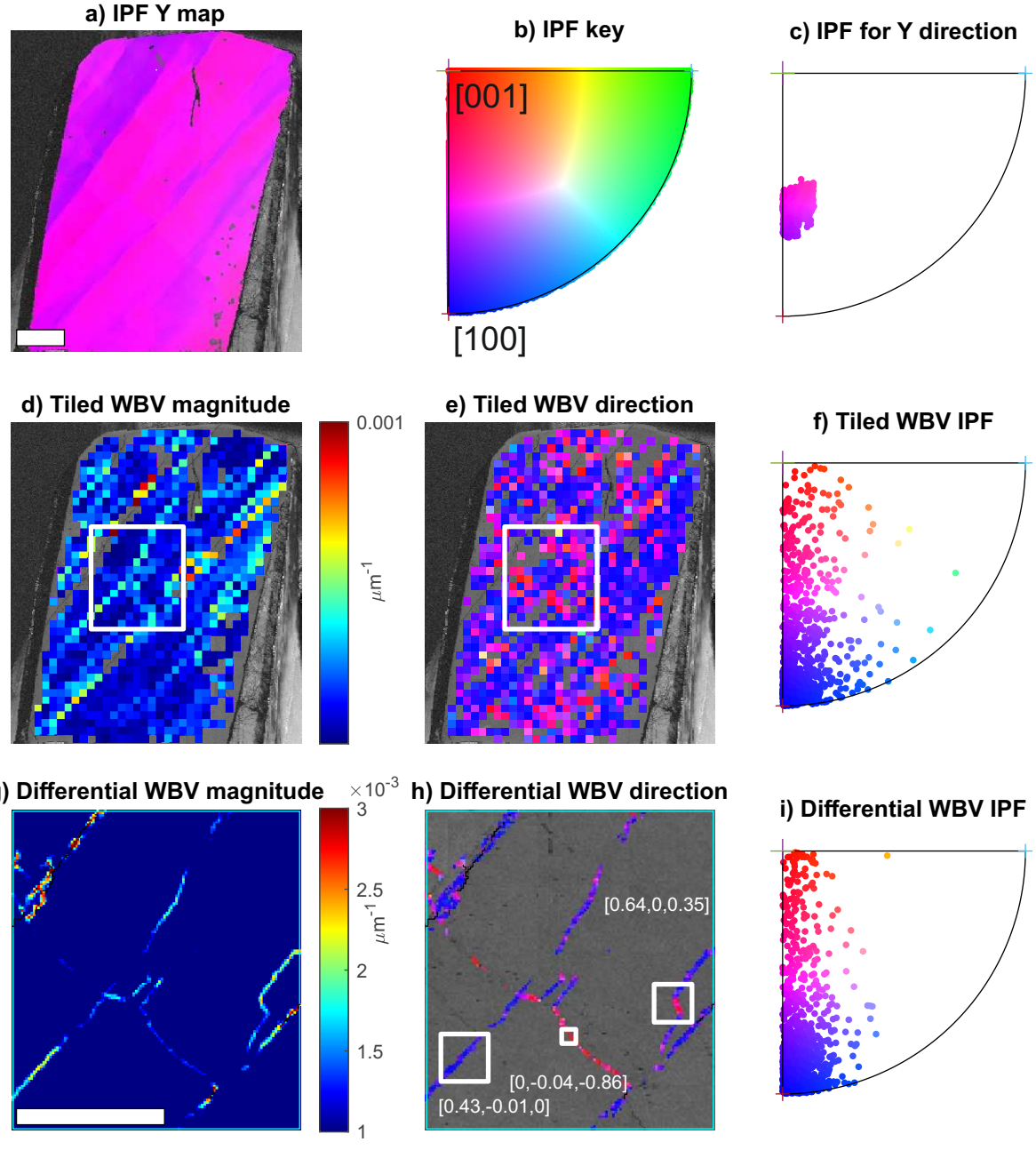

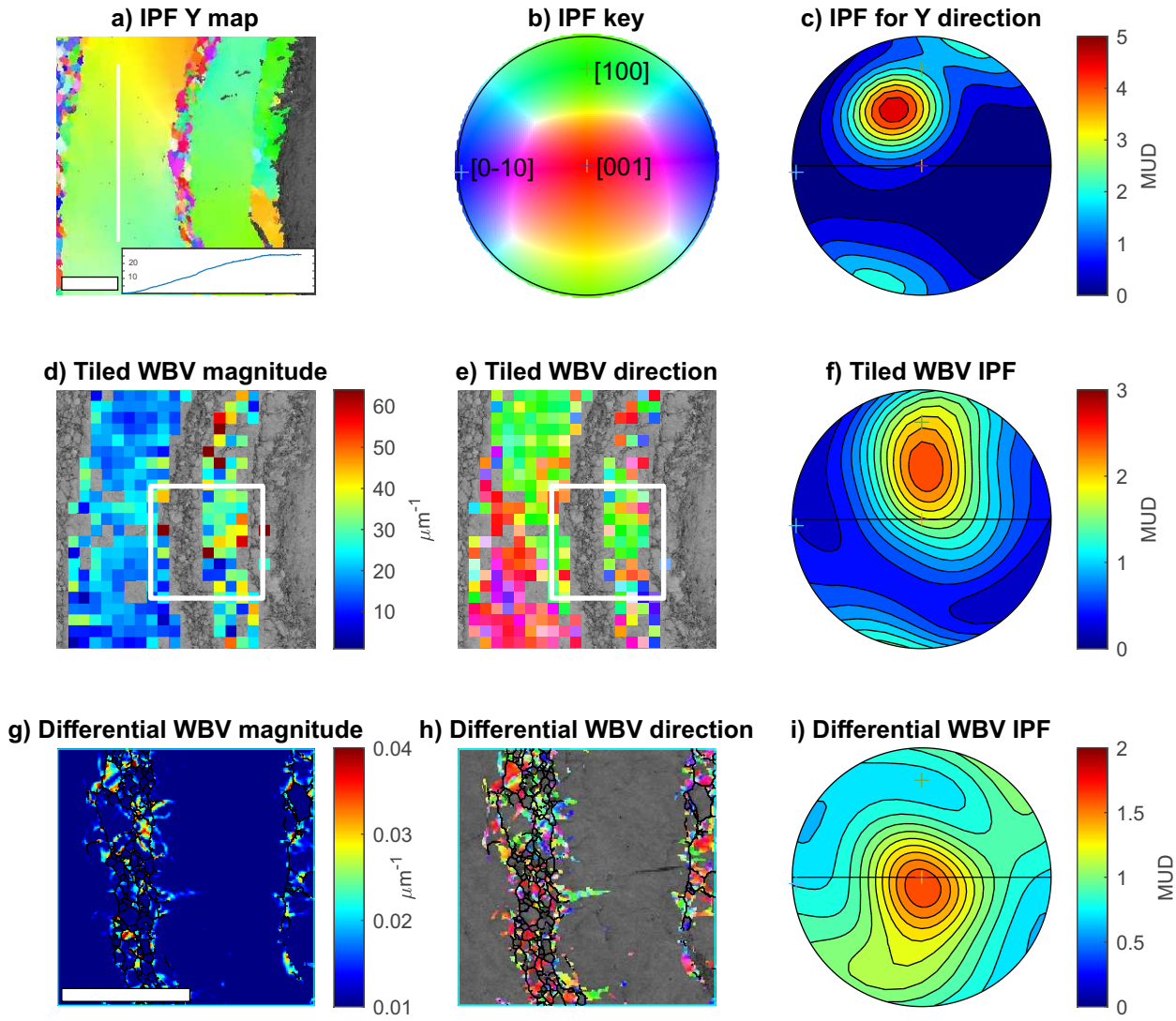

Figure 11

Click here to access/download;Figure;Fig. 11 iii 2020

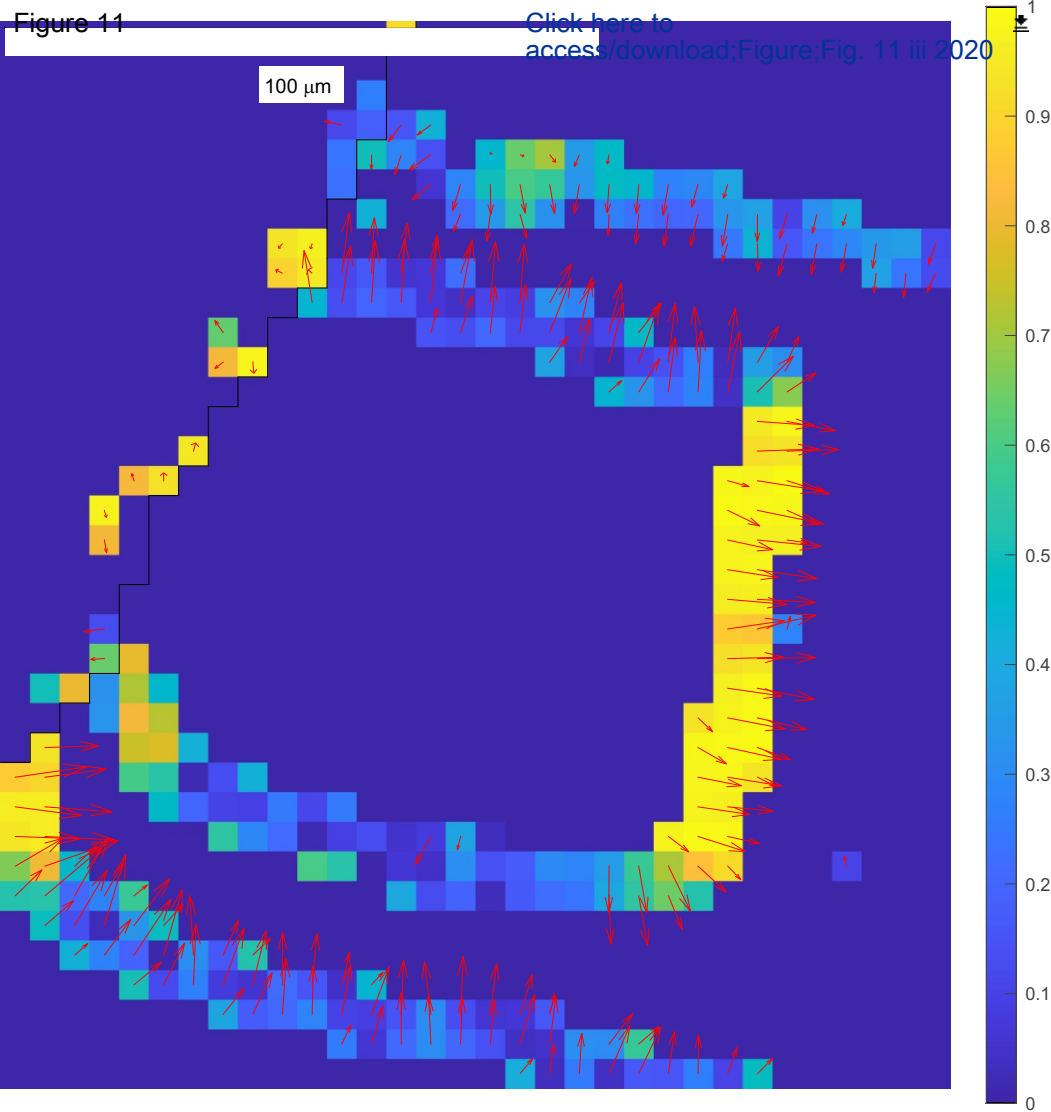

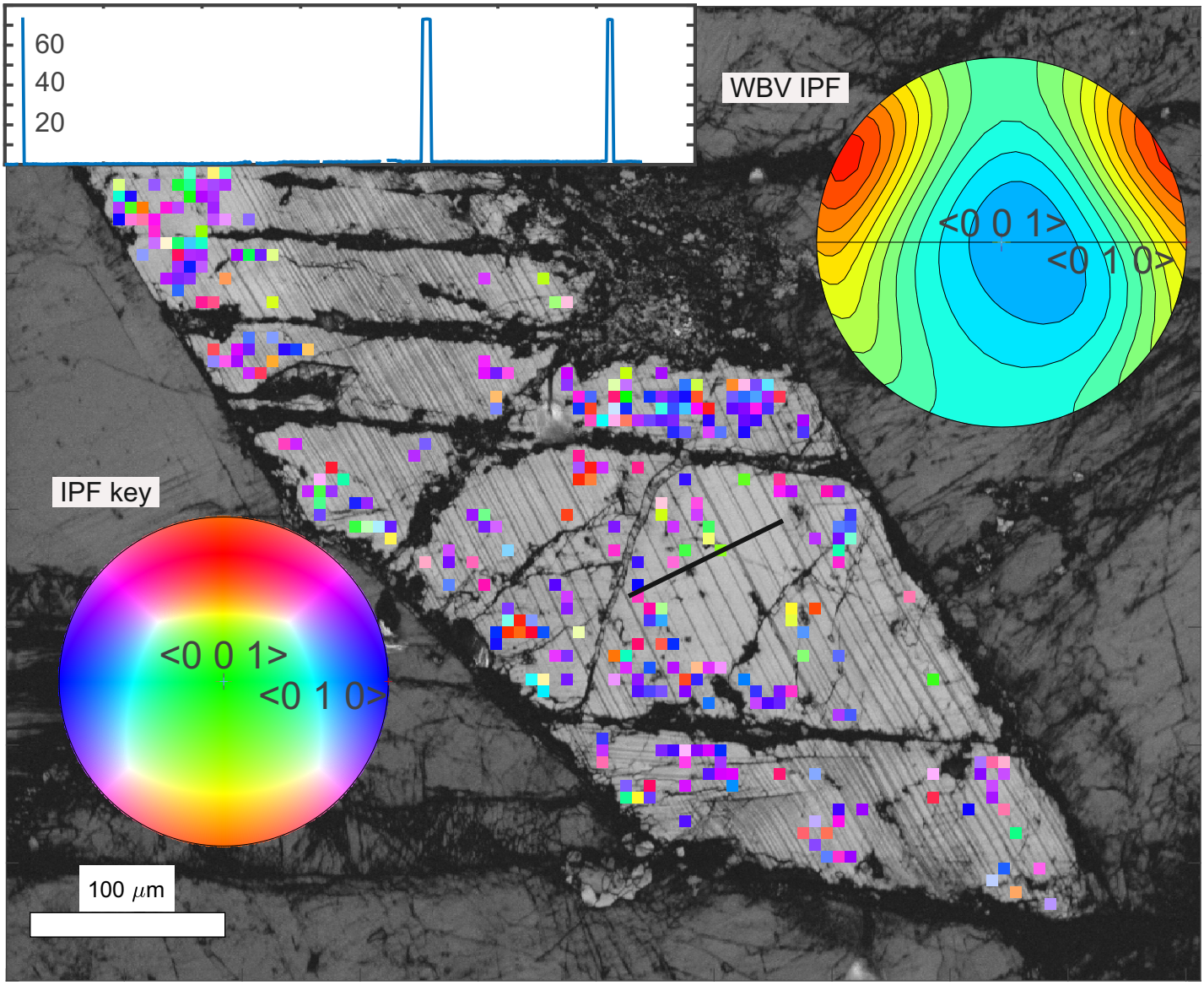

Figure S1

Click here to access/download;Figure;Fig. S1.jpg

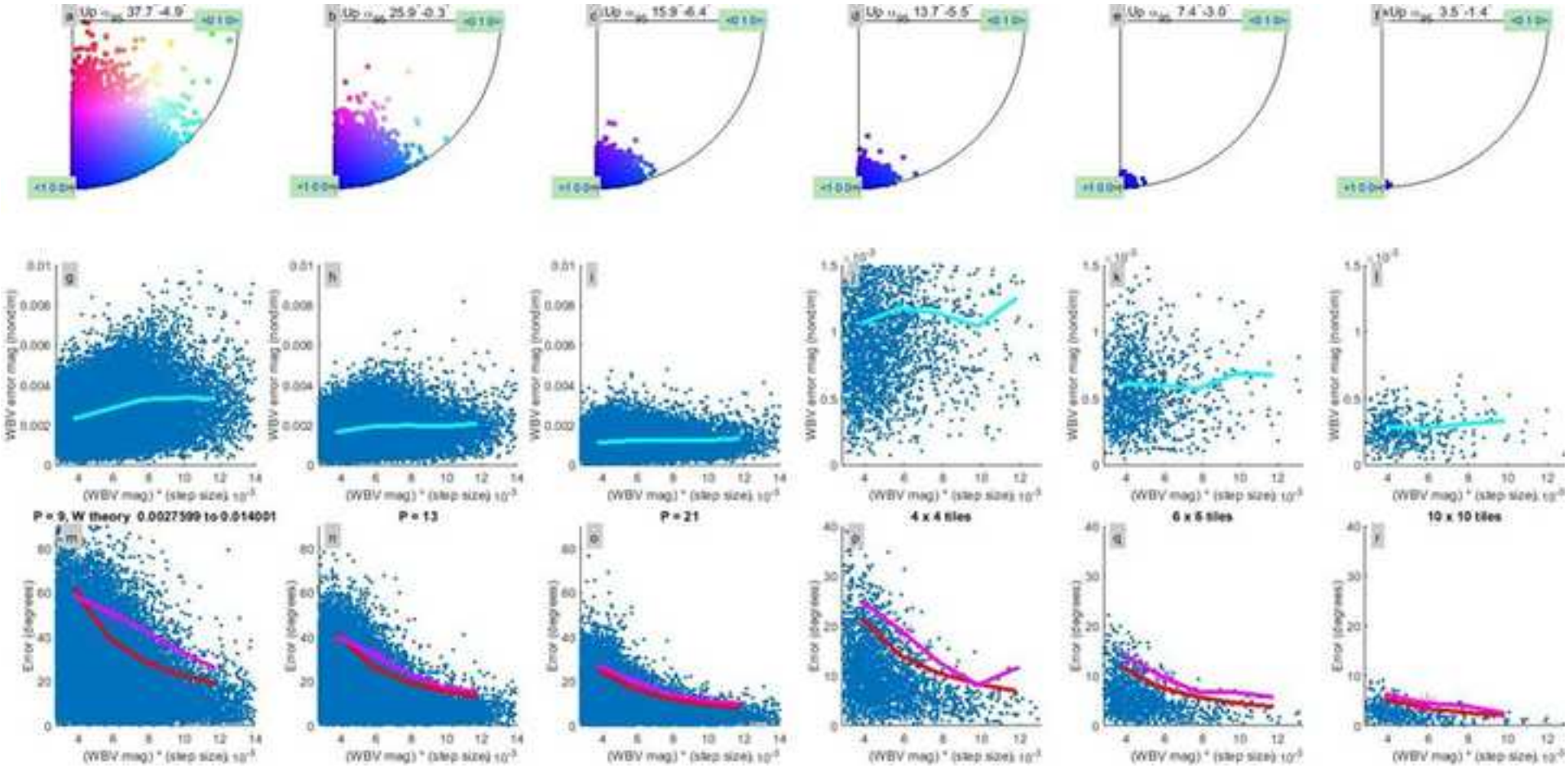

Figure S2

Click here to access/download;Figure;Fig. S2.jpg